Detailed Characterization of Nearby M Dwarfs with High-Resolution Near-Infrared Spectroscopy

by

Hiroyuki Tako Ishikawa

Dissertation

submitted to the Department of Astronomical Science

in partial fulfillment of the requirements for the degree of

Doctor of Philosophy

The Graduate University for Advanced Studies, SOKENDAI

January 2021

Abstract

M dwarf stars are the most numerous constituents of the Galaxy and recently observed intensively as prominent targets of planet search projects. Their chemical composition is crucial to understand the formation process and internal structure of orbiting exoplanets. However, measurements of elemental abundances of M dwarfs have been limited due to difficulties in the analysis of their optical spectra.

In this thesis, we report the abundance ratios of individual elements of M dwarfs in the solar neighborhood, including the mid- to late-M subtypes with effective temperature ($T_{\rm eff}$) < ~3200 K that has not been well studied by previous studies. This enables the first understanding of the elemental abundance distribution of nearby M dwarfs as promising planet-host candidates.

We firstly conducted a detailed chemical abundance analysis of five M dwarfs ($T_{\rm eff}$ ~ 3200–3800 K), which form binary systems with G/K-type stars, by performing a line-by-line analysis based on high-resolution (R ~ 80,000) near-infrared (960–1710 nm) spectra obtained with CARMENES (Calar Alto high-Resolution search for M dwarfs with Exo-earths with Near-infrared and optical Échelle Spectrographs). We determined the chemical abundances of eight elements (Na, Mg, K, Ca, Ti, Cr, Mn, and Fe), which are in agreement with those of the primary stars within measurement errors (~0.2 dex). This means the analysis method is reliable under this precision, given the reasonable assumption that the chemical abundances of stars in a binary system are identical.

Through the analysis process, we investigated the unique behavior of atomic lines in a cool atmosphere. Most atomic lines are sensitive to changes in abundances not only of the corresponding element responsible for the lines but also of other elements, especially dominant electron donors such as Na and Ca, through the change in continuous opacity. The Ti I lines show a negative correlation with the overall

metallicity at $T_{\rm eff} < 3400$ K due to the consumption of neutral titanium by the formation of TiO molecules. These findings indicate that, to correctly estimate the abundance of any element or the overall metallicity, it is needed to determine the abundances of other individual elements consistently.

We subsequently applied the verified abundance-analysis technique to 13 objects ($2900 < T_{\rm eff} < 3500$ K) among the targets of the IRD-SSP (InfraRed Doppler planet search project in the framework of the Subaru Strategic Program), which consists of nearby M dwarfs. We used the high-quality spectra obtained in the IRD-SSP to determine the abundances of eight elements (Na, Mg, Ca, Ti, Cr, Mn, Fe, and Sr) for all 13 M dwarfs. The abundances of three additional elements (Si, K, and V) were also determined for the hottest one.

The resulting metallicities of these M dwarfs, represented by [Fe/H] values, agree with previous metallicity estimates by medium-resolution K-band spectra within the error margin. The values range from approximately -0.6 to $+0.4$ centered at around 0.0. The abundance ratios of individual elements with respect to Fe, determined for the first time in the present work, are generally aligned with the solar values within the measurement errors in all M dwarfs. An exception is GJ 699 (Barnard's star) that shows a small departure from the solar abundance ratios.

The abundance ratios of individual elements are comparable to those of FGK stars in the solar neighborhood, most of which belong to the thin disk population. The wide distribution of metallicity, however, suggests a few of them could be thick disk stars. The Galactocentric space velocities UVW, which are calculated from the radial velocities we measured from the IRD spectra and the astrometric measurements of the Gaia mission, also suggest that a couple of M dwarfs studied in Chapters 2 and 3 show similar features to FGK stars classified into the thick disk.

The wide distribution of metallicity could have an impact on planet formation around M dwarfs. Whereas scaled solar abundances were found for the 13 objects studied in the present work, different abundance ratios could be found in a larger sample, given that the existence of thick disk stars is suggested. Abundance measurements of individual elements are required to determine accurate metallicity and to characterize planets found by the IRD-SSP and other planet searches.

This study provides the first reliable elemental abundances from the line-by-line analysis for a homogeneous sample of nearby M dwarfs, especially including more

than 10 objects with $T_{\rm eff}$ less than 3200 K that have not been previously investigated. We also show the possibility of locating M dwarfs on the Galactic chemical evolution based on the elemental abundance ratios. The future extension of the analysis to all the targets of the IRD-SSP and other planet search projects around M dwarfs will lead to a further understanding of the abundance distribution of M dwarfs. This will be useful to explore the relation between the chemical composition of M dwarfs and properties of the orbiting planets and constrain planet formation theories around the most ubiquitous stars in the Galaxy.

Acknowledgments

I would like to express my sincere gratitude to Wako Aoki for supervising me and always giving me helpful and constructive instructions. He gave me the precious research life in NAOJ and the direction of how to behave as a researcher in countless ways, such as how to analyze data, discuss the results, look for problems, and express the outcomes in reports and presentations. My data analysis, presentation, and the preparation of papers, observation proposals, and other documents have been all possible because of his generous support.

I also deeply appreciate the warm supports and instructions of my associate supervisors, Saeko Hayashi and Takayuki Kotani, and my former supervisor, Tomonori Usuda. Thanks to them, I was welcomed into NAOJ and have spent invaluable five years here. Their advice on my research plan and reports always helped and encouraged me.

I greatly thank my collaborators, Masayuki Kuzuhara, Masashi Omiya, Teruyuki Hirano, Ansgar Reiners, and Mathias Zechmeister. Their insightful and constructive comments and suggestions have helped me grow in both my research and my writing. I am also grateful to Yasunori Hori, Jun Hashimoto, Nobuhiko Kusakabe, Aoi Takahashi, all the IRD team members, and many other wonderful colleagues in NAOJ and ABC. The discussions with them were always inspiring and exciting.

My deep gratitude also goes to the thesis committee members, Hideyuki Izumiura, Hirohisa Hara, Misato Fukagawa, Shu-ichiro Inutsuka, and Hajime Kawahara for their careful reading and thoughtful and constructive comments, which were invaluable in refining this thesis in the final stages.

Many thanks to all the staff members in NAOJ and SOKENDAI for their patient support with administrative procedures and daily support. My research life at Mitaka

has been very fruitful thanks to the excellent facilities and financial support of NAOJ and SOKENDAI.

I am grateful to the many people in my life who have guided and fostered my zeal towards the starry skies and the universe beyond, and the field of astrobiology and astronomy. I am here because of a series of fortunate meetings: the friends I talked with in my boyhood while looking up at the starry sky, the people at the science museum and public observatory in Hyogo Prefecture, the friends of Sommelier of Star in Kyoto, the respectable researchers and friends I met as an undergraduate at Kyoto University, such as Kosuke Namekata, Yuma Sugahara, Keisuke Takatori, and Hiroki Nagaoka, and the staff at the Mauna Kea Observatories who especially support the Subaru Telescope, and many more. I cannot list them all here, but I would be happy to continue to share the joy that the starry sky gives us.

I appreciate my all dear friends inside and outside of astronomy for supporting and inspiring me a lot. Especially, I want to give my appreciation for keeping me motivated to my peers (and senpai/kohai) at NAOJ: Ko Hosokawa, Jinshi Sai, Masayuki Yamaguchi, Tadafumi Matsuno, Satoshi Kikuta, Takafumi Tsukui, Noriharu Watanabe, Yusuke Tanaka, Satoshi Tanioka, Yoshiki Hatta, and too many others to name.

Finally and sincerely, from the bottom of my heart, I thank my wife Madoka, brother Yutaka, best-friend Shintaro, my parents, and the rest of my family for always being on my side.

Contents

1 Introduction

1.1 M dwarfs as planet-search targets

M dwarf stars are favorable targets for the discovery and detailed characterization of rocky planets, especially in the habitable zone, owing to their small mass, small size, and low luminosity compared to hotter Sun-like stars (e.g., Shields et al. 2016). Their low mass boosts the radial velocity signal of small planets. For a system with a planet with a given size and orbit, the transit signal on a smaller star also gets larger because the amplitude of the transit is proportional to the square of the ratio of radius between a planet and its host star. The lower luminosity of M dwarfs makes the habitable zones closer to the central stars. As a result, planets in the habitable zones provide larger radial velocity, higher geometric probability of transit events, and shorter periods of those signals.

One primary obstacle to the investigation of planets around M dwarfs is their faintness in the visible band. Through recent advancements in infrared detector technology, various infrared instruments have been developed that increase the

feasibility of the study of M dwarfs because their peak fluxes are at infrared wavelengths. Many current and future planet-search projects have set M dwarfs as the primary targets. For example, ground-based transit surveys such as MEarth (Irwin et al. 2015), APACHE (Sozzetti et al. 2013), and SPECULOOS (Delrez et al. 2018) mainly target M dwarfs. Ground-based radial velocity surveys such as IRD (Kotani et al. 2014), CARMENES (Quirrenbach et al. 2014), HPF (Mahadevan et al. 2012), and SPIRou (Artigau et al. 2014) also focus on M dwarfs. Space-based surveys such as K2 (Howell et al. 2014) have discovered a significant number of planets orbiting M dwarfs to date, and NASA's Transiting Exoplanet Survey Satellite (TESS; Ricker et al. 2015) is expected to detect approximately 500 planets around M dwarfs (Barclay et al. 2018).

1.2 Chemical composition of M dwarfs

To investigate the characteristics or habitability of planets found around M dwarfs, it is crucial to determine the detailed chemical compositions of the host M dwarfs. The stellar chemical composition provides the initial condition of planet formation. Especially, the ratios of refractory elements in planets are expected to be consistent with those of the host stars (Thiabaud et al. 2014).

Although the mean density of a rocky planet is estimated from its mass and radius, the features of internal structures such as core size and mantle mineralogy, which control the surface habitability, cannot be determined without the constraints from the chemical composition (e.g., Dorn et al. 2017, Unterborn & Panero 2017). Bitsch & Battistini (2020) calculated the chemical composition of planetary building blocks, taking into account the abundance variation of some key elements, not only iron, of the host stars. Their results show that different elemental abundances can significantly change the amount of rock-forming materials. In particular, the water-ice content of the building blocks formed outside the water-ice line (T > 150 K) varies by about an order of magnitude.

A common measure of stellar chemical composition is the overall metallicity. It is expressed as [M/H], which is the logarithm of the number ratio of all metals to hydrogen in the object of interest, normalized by the corresponding ratio in the Sun. The iron abundance ratio [Fe/H], which is calculated in the same manner but with the number of Fe instead of all metals, is often used as a proxy for the overall metallicity.

The relation between the stellar metallicity and the planet occurrence rate (the so-called planet–metallicity correlation) has been discussed since Santos et al. (2004) and Fischer & Valenti (2005) established the case of Jupiter-mass planets around FGK stars. Brugamyer et al. (2011) and Adibekyan et al. (2012b) reported that the abundances of refractory elements such as Si, Mg, and Ti have a stronger correlation than the overall metallicity with the occurrence rate of giant planets. These relations support the core-accretion scenario as the standard planet formation mechanism. Such relations for M dwarfs have also been investigated, but they remain under discussion (e.g., Hobson et al. 2018, Neves et al. 2013). Further studies of M dwarfs with detailed abundances of refractory elements are needed to develop a better understanding of such trends.

The characterization of planetary atmospheres has advanced in the past few years. Various species such as H_2O, TiO, Na I, and K I have been detected. We refer the reader to Madhusudhan (2019) for a tabulated list of detection methods, investigated planets, and detected species. In order to advance detailed discussions of planetary atmospheres, it is important to take the elemental abundances of the host stars into account.

For giant planets, one of the interesting topics related to the planetary and stellar chemistry is the mass-metallicity trends of planets. It is known that the metallicity of giant planets in our solar system, estimated precisely from CH_4 measurements (CH_4/H), tends to increase with decreasing planetary mass. It is naturally explained by planet formation scenarios based on the planetesimal accretion (e.g., Fortney et al., 2013). Similar trends were suggested also in exoplanetary atmospheres (e.g., Welbanks et al., 2019), although it is not that significant and some differences between the probed species. Welbanks et al. (2019) used the abundances of individual elements of the host FGK stars based on high-resolution spectroscopy for eight among the 19 objects, while those of the other objects are approximated by scaling the solar elemental-abundance pattern by their overall metallicity [Fe/H] or [M/H]. The atmospheric characterization of super-Earths and terrestrial-sized exoplanets will be accelerated by JWST (Gardner et al., 2006), mainly for planets orbiting low-mass stars. Therefore, elemental abundances of M dwarfs are needed to explore these trends in a wider temperature range including M dwarfs.

1.3 M dwarf in the Galaxy

M dwarfs are also important in the Galactic context because they are the most numerous constituents of the Galaxy being accounting for more than 70 % of the nearby stars (Henry et al., 1994). In addition, their lifetimes are longer than the current age of the universe, which means they are the ideal tracer of the Galactic history. Many studies have collected the data of photometry, kinematics, and spectra of M dwarfs for the study of Galactic archaeology (e.g., Bochanski et al., 2010; West et al., 2011; Hejazi et al., 2020; Woolf & Wallerstein, 2020).

The abundance ratio of individual elements is one of the essential tools to explore the chemical evolution of the Galaxy. Several studies have identified the chemically separated populations by probing the elemental abundance trends (especially [α/Fe] ratio) for stars of individual populations (e.g., Reddy et al., 2006; Bensby et al., 2014; Holtzman et al., 2015). However, most of this previous knowledge of the detailed chemical composition has been limited to the more massive members than M dwarfs. Similar abundance trends of M dwarfs have been reported using [α/Fe] (Hejazi et al., 2020) or [Ti/Fe] (Woolf & Wallerstein, 2020) lately.

Recently, it has also been discussed that the occurrence rates of planets depend on the Galactic population. Bashi et al. (2020) found a mysterious fact that concerning the iron-poor regimes ([Fe/H] < 0), the occurrence rates of low-mass close-in planets are significantly larger at high-α FGK stars in the thick disk than low-α FGK stars in the thin disk. Also around the M dwarfs in the thick disk, planet detections have been increased recently (e.g., Gan et al., 2020).

The abundance measurements of individual elements of nearby M dwarfs, which are targets of planet searches, will enable the extension of these previous insights to the dominant type of stars in the Galaxy.

1.4 Previous determinations of M dwarf chemistry

The chemical analysis of M dwarfs is hampered by their optical faintness and the complicated molecular absorption bands. The difficulty of modeling the forest of molecular lines limits the determination of the continuum level and identification of isolated absorption lines, especially in the optical spectra.

Many previous studies have proposed empirical relations between the overall metallicity and the metal-sensitive observable in photometry or low- to medium-resolution spectroscopy. These relations are empirically calibrated by binary systems consisting of M-dwarf secondaries and FGK primaries for which reliable chemical abundances are determined by standard abundance analysis. Stars in a binary system are formed together from the same molecular cloud; thus, their chemical abundances can be regarded as identical, typically within the level of 0.02 dex, and occasionally differing up to approximately 0.1 dex. This has been confirmed by several studies using binary systems comprised of FGK stars (e.g., Desidera et al. 2004, 2006, Hawkins et al. 2020).

Bonfils et al. (2005) first derived the relation between the K-band magnitude, $V-K$ color, and the metallicity for M dwarfs. Following Rojas-Ayala et al. (2012), who used the strong metal lines in the K_s-band medium-resolution spectra, Mann et al. (2013a, 2014) established the empirical calibrations based on medium-resolution spectra in each band of visible, J-, H-, and K-bands. Recently, some data-driven approaches have been developed. Birky et al. (2020) applied the supervised machine learning code to the APOGEE spectra (H-band, $R \sim 22,500$; Majewski et al. 2017) of 5,875 M dwarfs to simultaneously derive the stellar parameters, including the metallicity. Maldonado et al. (2020) determined abundances of individual elements from high-resolution optical spectra using principal component analysis and sparse Bayesian method by using a training dataset of 19 binary pairs of M-dwarf companions and FGK primary stars.

The empirical calibrations above are useful for the exploration of global trends of overall metallicity. An advantage of the empirical methods is that they are available over a wide temperature range because they only need the observation of M dwarfs in binary systems with hotter stars and do not depend on other stellar parameters or the accuracy of the model. For example, the empirical formula of Mann et al. (2014) using medium-resolution K-band spectra was calibrated in the range covering all M dwarfs as late as M9.5V. They are not, however, able to address abundance variations between the individual elements.

The most preferable way to directly address these abundances is to analyze individual absorption lines in high-resolution spectra with model atmospheres. Mould (1976) first determined the iron and titanium abundances of M dwarfs with the model comparison on a line-by-line basis. Since then, several studies have attempted the

chemical analysis of M dwarfs using model atmospheres, such as synthetic spectral fitting and equivalent width comparison (e.g., Valenti et al. 1998; Zboril & Byrne 1998; Woolf & Wallerstein 2005; Bean et al. 2006), along with the progress of the model atmospheres for cool objects (e.g., Allard & Hauschildt 1995; Hauschildt et al. 1999).

In the last decade, several high-resolution near-infrared spectrometers have become available for the purpose of radial velocity surveys. Their increasing data of M dwarfs have led to advances in their chemical analysis. Their near-infrared spectra are relatively free from the complicated and crowded molecular bands found in the visible spectra, and are therefore more suitable for line-by-line analysis of atomic lines. Önehag et al. (2012), Lindgren et al. (2016), and Lindgren & Heiter (2017) analyzed the atomic lines of various elements in high-resolution ($R \sim 50,000$) J-band CRIRES (Kaeufl et al. 2004) spectra of early- to mid-M dwarfs to derive their metallicities by fitting synthetic model spectra. They verified the reliability of the results using five M dwarfs in binary systems with FGK primaries. They reported that the results of both components are generally consistent within 0.01–0.04 dex and at most 0.11 dex. Rajpurohit et al. (2018b) performed overall spectral fitting on the APOGEE spectra of 45 early- to mid-M dwarfs to determine the stellar parameters, including the metallicity. Rajpurohit et al. (2018a) conducted spectral fitting on a variety of atomic lines and OH molecular lines in the high-resolution ($R \sim 80,000$–$100,000$) visible and near-infrared spectra of 292 early- to late-M dwarfs taken by CARMENES to infer the stellar parameters, including the metallicity. Passegger et al. (2019) also derived the stellar parameters for a similar set of objects from the CARMENES spectra with a higher signal-to-noise ratio (S/N) by carefully selecting a limited number of absorption lines that are exclusively sensitive to the parameters of interest. Although their derived metallicities show better agreement with previous estimates through calibrated methods, there remain some systematic trends. This results in a narrower metallicity distribution than the estimates for the same objects in the literature. It was also noted that the metallicity derived only from the near-infrared spectra tends to be higher than that derived only from the visible spectra which shows better agreement with literature values. Thus, they pointed out the possibility of wavelength dependency of synthetic model grids. Souto et al. (2020) performed spectral fitting of APOGEE spectra to determine the metallicities of 21 early- to mid-M dwarfs, 11 of which form binary systems with FGK primary stars. They confirmed that their results for the 11 M

dwarfs are consistent with the metallicities of the corresponding primaries with a mean difference of 0.04 dex.

Among these attempts, systematic differences in derived metallicities between different works are found in some cases. They used different sets of absorption lines associated with different species to infer the overall metallicity. One possible improvement to reliably determine metallicity is to consider the abundance ratios of individual elements. Tsuji & Nakajima (2014), Tsuji et al. (2015), Tsuji & Nakajima (2016), and Tsuji (2016) determined the carbon and oxygen abundances and even the carbon isotopic ratios for M dwarfs based on CO and H_2O lines in K-band spectra with a resolution of ~20,000. Veyette et al. (2016) found that the relative abundance of carbon to oxygen changes the pseudo-continuum of visible to near-infrared spectra of M dwarfs, which affects the derivation of the metallicity, particularly for empirical calibration methods. Veyette et al. (2017) developed a semi-empirical approach to determine the abundances of Fe and Ti. They performed high-resolution ($R \sim 25,000$) Y-band spectroscopy on 29 M dwarfs that form physical binaries with FGK stars. They found a discrepancy between the equivalent width (EW) measured for the M-dwarf secondaries and those calculated from the model adopting Fe and Ti abundances of the FGK primaries. They empirically determined a transformation formula for the measured EWs to obtain an agreement with the calculated ones. Souto et al. (2017, 2018) determined the abundances of 13 elements for two early-M dwarfs and eight elements for one mid-M dwarf using atomic and molecular lines in the APOGEE spectra. Souto et al. (2020) also constrained the carbon and oxygen abundances of 21 M dwarfs in the process of estimating their effective temperatures based on the H_2O and OH molecular lines. Hejazi et al. (2020) determined the [M/H] and [α/Fe] of 1544 high proper-motion M dwarfs with the template fitting of the model spectra to the visible medium-resolution spectra. They evaluated the precision of their derivation by confirming the consistency between the results for the M dwarf pairs in 48 binary systems. Woolf & Wallerstein (2020) determined the [Fe/H] and [Ti/H] of volume-limited 106 early-M dwarfs with the equivalent width analysis on the atomic lines in visible spectra with a resolution of ~33,000.

As listed above, although there have been numerous attempts to determine the metallicity and elemental abundances of M dwarfs, no studies have simultaneously and homogeneously determined the abundances of individual elements in a way that is

consistent with both model calculations and binary observations. While developments such as empirical calibration and the application of machine learning are promising, it is still indispensable to understand M-dwarf composition based on the understanding of the physics and chemistry in low-temperature atmospheres. It is also important to investigate the meaning of abundance determination for individual elements in a consistent manner, and whether the commonly used assumption of scaled-solar abundance ratios is valid. We need a method of abundance determination for M dwarfs that is based on model atmospheres but also consistent with the expected abundance uniformity in binary systems.

1.5 Goal of the thesis

The main objectives of this thesis are to grasp the abundance distribution of individual elements of nearby M dwarfs as promising planet-host candidates. We aim to provide the first reliable measurement of elemental abundance ratios for a decent amount of homogeneous sample of objects with $T_{\rm eff} < 3200$ K.

We determine the abundances with the line-by-line EW analysis using high-resolution near-infrared spectra obtained with CARMENES and IRD. The analysis method has to be assessed and calibrated anew even though it is based on the standard method for sun-like stars, because the atmosphere of M dwarfs and resulting spectra largely differ from those of sun-like stars due to their low-temperature and molecular line forest. None of the previous studies using high-resolution near-infrared spectra have verified the abundance analysis of elements other than Fe and Ti.

In Chapter 2, we verify our analysis method by confirming the agreement between the elemental abundances of M dwarfs in physical binary systems with G or K dwarfs and those of the primary stars. We study binary systems including mid-M dwarfs that are not well studied by previous studies. We also report the contribution of individual error sources. In Chapter 3, we apply the verified abundance-analysis method to 13 M dwarfs among the target stars of the IRD-SSP planet search project. Combining the resulting elemental abundances with the kinematics calculated from astrometric measurements of Gaia, we discuss the stellar populations of individual M dwarfs. We also explore the possibility to determine temperatures of M dwarfs from the line-by-line analysis of FeH molecular lines in Y-band. Finally, we summarize the

conclusion and present our future prospects in Chapter 4.

2

Verification of chemical analysis by Binary Systems

This chapter is based on Ishikawa et al. (2020).

2.1 Overview

Chemical analysis of M dwarfs based on model atmospheres has shown promise as a straightforward way to determine elemental abundances. However, the validity of the results and the potential problems inherent to the cool objects must be confirmed. One typical and preferable way to verify the results of abundance analysis is the comparison of stars in binary systems. In this chapter, we present the abundance determination of eight individual elements for two early-M and three mid-M dwarfs that belong to binary systems with G- or K-type stars.

By examining the effects of variations in elemental abundance ratios assumed in the analysis on the abundances derived for certain elements, we demonstrate the

importance of determining individual elemental abundances consistently. The chemical composition of M dwarfs and its effects on the spectra cannot be accurately described by the overall metallicities scaled from the solar chemical composition alone.

We introduce our targets and data in Section 2.2. We describe how we exploit them to derive the abundances of individual elements and errors in Section 2.3 and present the results in Section 2.4. We discuss the newly found problems and the remedies in Section 2.5. In Section 2.6, we summarize the chapter.

2.2 Target selection and data

We selected five M dwarfs that are reported to form common proper-motion binary systems with G- or K-type stars. The high-resolution near-infrared spectra observed by CARMENES (Calar Alto high-Resolution search for M dwarfs with Exo-earths with Near-infrared and optical Échelle Spectrographs) of four of the M dwarfs are obtained from the CARMENES GTO Data Archive[1] (Reiners et al. 2018). We observed another M dwarf (G 102-4) with CARMENES in a separate program (PI: M. Kuzuhara, Proposal Number: H18-3.5-091, F19-3.5-091). We stacked the data of G 102-4 taken in three separate nights: December 14, 2018; January 28, 2019; and March 14, 2019. The total exposure times for each night were 1798 s, 1398 s, and 2196 s, respectively, but the data in December and January fell short of the expected S/N due to the weather conditions. Basic information and data quality for each object are provided in Table 2.1. The near-infrared channel of CARMENES covers the wavelength range of 960–1710 nm (Y-, J-, and H-bands) with a spectral resolution of $R \sim 80{,}000$. There are gaps in the wavelength coverage of CARMENES. These are mostly less than 15 nm and are located between adjacent echelle orders or in the center of each echelle order. The gap in the center of each order is induced by a small gap between the two detectors.

The CARMENES data are provided as the one-dimensional spectra with vacuum wavelengths. They were reduced by the CARACAL pipeline (e.g., Zechmeister et al. 2014; Caballero et al. 2016). We normalized the spectra by fitting cubic spline curves to the continuum level of each echelle order. This procedure was conducted with the interactive mode of PyRAF[2]. Further adjustment of the continuum level close to each

[1] http://carmenes.cab.inta-csic.es/gto/jsp/reinersetal2018.jsp

[2] PyRAF is a product of the Space Telescope Science Institute, which is operated by AURA for NASA.

Table 2.1: Basic information of the target M dwarfs (in order of $T_{\rm eff}$)

Name	R.A.	Decl.	SpT*	$T_{\rm eff}$	$\log g$	Name of	SpT* of	[Fe/H] of	S/N†
	J2000.0			(K)		Primary	Primary	Primary	(1000 nm)
HD 233153	05:41:30.73	+53:29:23.3	M1.0V	3765±60	4.70±0.13	HD 37394	K1V	0.04±0.02	158
HD 154363B	17:05:13.78	−05:05:39.2	M1.5V	3658±67	4.79±0.21	HD154363A	K5V	−0.62±0.05	182
BX Cet	02:36:15.27	+06:52:17.9	M4.0V	3284±60	4.94±0.13	HD 16160A	K0V	−0.20±0.02	122
G 102-4	05:28:56.51	+12:31:53.5	M4.0V	3246±57	4.97±0.20	HD 35956	G0V	−0.05±0.02	107
ρ^{01} Cnc B	08:52:40.86	+28:18:58.8	M4.5V	3166±61	4.94±0.14	HD 75732	G8V	0.29±0.04	56

* Spectral type † Signal-to-noise ratio

absorption line was also made in the process of EW measurement. We merged the echelle orders into one spectrum for each object. The spectra were Doppler-shifted to the stellar rest frame based on the radial velocity estimated by cross-correlation with the model spectra calculated from atomic line data.

2.3 Abundance analysis

Our abundance analysis is based on the standard technique using a comparison between the EWs from observed spectra and those from synthetic spectra calculated with the one-dimensional (1D) LTE radiative transfer code (see Section 2.3.2 for details). The process is well established for visible spectra of FGK-type stars (e.g., Jofré et al. 2019). However, there are difficulties in the analysis of near-infrared spectra of M dwarfs that have not yet been investigated well (see Section 2.5). We carefully selected useful absorption lines for abundance analysis and employed valid atmospheric models for the temperature range of our targets.

2.3.1 Stellar parameters

For the calculation of model spectra, we need to set the stellar parameters, i.e., effective temperature $T_{\rm eff}$, surface gravity $\log g$, micro-turbulent velocity ξ, and elemental abundance ratios [X/H].

We adopted the literature values for $T_{\rm eff}$ and $\log g$ of the target and considered the errors propagated from the uncertainties reported. The surface gravity is not directly reported in some cases but can be calculated from the masses and radii. We referred to Mann et al. (2015) (hereafter Man15) for the effective temperatures, masses, and radii

of HD 233153, BX Cet, and ρ^{01} Cnc B. They derived the effective temperature by fitting the model spectra from the PHOENIX BT-Settl model atmosphere (Allard et al. 2012) to the observed medium-resolution ($R \sim 1000$) visible spectra. They estimated the masses using the empirical mass–luminosity (mass–M_K) relation in Delfosse et al. (2000) and the radii from $T_{\rm eff}$, bolometric flux $F_{\rm bol}$, and distance using the Stefan–Boltzmann law. $F_{\rm bol}$ was calculated by integrating the medium-resolution visible and near-infrared spectra complemented by the best-fit spectra from the BT-Settl model. We referred to Gaidos et al. (2014) for the same set of parameters of HD 154363B. They derived $T_{\rm eff}$ and the mass in the same manner as Man15 but employed the empirical $T_{\rm eff}$–radius relation in Mann et al. (2013b) for the radius. We referred to Terrien et al. (2015) for $T_{\rm eff}$ of G 102-4, which was estimated using the H_2O indices in the K-band defined in Mann et al. (2013b). We used this $T_{\rm eff}$ to calculate the radius and mass by the radius–$T_{\rm eff}$ relation in Man15 and the mass–radius relation in Schweitzer et al. (2019), respectively. Finally, we used the masses and radii above to calculate the surface gravity $\log g$ for each object.

The micro-turbulent velocity ξ of M dwarfs can be assumed to be less than 1 km s^{-1}, as demonstrated observationally by Bean et al. (2006) and theoretically by Wende et al. (2009). We set ξ to 0.5 km s^{-1} for all objects for simplicity. The changes in the resulting abundances by varying ξ from 0.0 km s^{-1} to 1.0 km s^{-1} were included in the error estimate.

Note that the macro-turbulence and spectral resolution both have the effect of broadening line profiles, but do not affect the EW.

The $T_{\rm eff}$ and $\log g$ adopted in our analysis, and the associated errors, are given in Table 2.1. Note that we give the metallicities of the primaries in the table only for comparison purposes.

2.3.2 Synthetic spectra

Synthetic spectra are calculated with 1D LTE radiative transfer code for a variety of individual elemental abundances assumed. The line lists with transition probabilities we used are described in the next subsection. We apply the radiative transfer code constructed based on the same assumptions for model atmospheres of Tsuji (1978), i.e., 1D plane-parallel geometry, local thermodynamical equilibrium (LTE), radiative and

hydrostatic equilibrium, and chemical equilibrium of reactions in gas.

For the atmospheric layer structure, we employed the 1D plane-parallel LTE model atmosphere of MARCS[3] (Gustafsson et al. 2008). It was constructed with physical assumptions of 1D plane-parallel geometry, hydrostatic equilibrium, LTE, and mixing-length convection. The MARCS team also provides the grid calculated with a spherical geometry, but in M dwarfs, the layer of the atmosphere is so thin compared to the stellar radius that the difference of geometry does not significantly change the atmospheric structure. Thus, we used the plane-parallel models in this study to match the radiative transfer code. The molecular line opacities in the MARCS model are computed with the opacity sampling method, where only a limited but adequate number of lines, with significant contribution to the total opacity, are considered at each monochromatic wavelength point.

The grids of the atmospheric structure for $T_{\rm eff}$, $\log g$, ξ, and [Fe/H] are separated at intervals of 100 K, 0.5 dex, 1 km s^{-1}, and 0.25 dex, respectively. Among the seven different "metallicity classes", we used the "standard", which reflects the typical elemental abundance ratios in stars in the solar neighborhood. In the models on the metal-poor side ([Fe/H] < 0.0), [α/Fe] is set to increase by 0.1 dex for every 0.25 dex decrease in [Fe/H] from 0.0. We interpolated the grid for our analysis.

Note that dust formation and dust opacity are not considered in either the spectral synthesis calculation or the construct of the MARCS model atmosphere. The target M dwarfs are hotter than 2800 K, in which $T_{\rm eff}$ range the dust formation in the atmosphere is negligible (e.g., Allard et al. 2013).

We compared the temperature profiles as a function of pressure (P–T profiles) of the MARCS with those of the PHOENIX-ACES model grid of Husser et al. (2013) that was specifically designed for cool dwarfs. The differences in temperature in the typical depth of line formation are less than 100 K, and thus do not have a significant impact on our results.

2.3.3 Spectral lines

The spectral line data for all atoms and major molecules were taken from the Vienna Atomic Line Database (VALD; Kupka et al. 1999, Ryabchikova et al. 2015). We also

[3] https://marcs.astro.uu.se/

added the data of FeH molecular lines, which form the prominent absorption band head around 1000 nm, using the line list edited by Plez (Önehag et al. (2012)) to avoid contamination of the FeH lines on atomic lines.

We identified atomic absorption lines by comparing the observed spectra to the synthetic spectra. We identified many atomic lines in the wide wavelength range of *Y*-, *J*-, and *H*-bands, but they could not all be used for the analysis because of the following difficulties: (1) The existence of many weak but unidentified absorption lines makes it impossible to robustly determine the continuum level; (2) Blending of other absorption lines; (3) Strong wing components appear even in relatively shallow absorption lines in the spectra of M dwarfs compared to those of FGK stars due to the high pressure of M-dwarf atmospheres (pressure broadening; see below for details); (4) The line strength is sensitive to changes in abundance of some elements other than the species responsible for the absorption line (see Section 2.5.1).

Comparing the observed and synthetic spectra, we carefully selected the candidate absorption lines that were not affected significantly by issues (1) or (2). We made the final line list considering issues (3) and (4), and the number of candidate lines for each element. For example, we excluded five Fe I lines from the analysis of mid-M dwarfs due to issues (3) and (4), whereas we did not exclude the Mg I line, which is a unique line available for the analysis, even though it had widely broadened wings and low sensitivity to Mg abundance. The information on the spectral lines used for abundance determination is presented in Table 2.2. Some lines of interest, such as the only Si I line unaffected by the telluric contamination, fall into the gaps of the CARMENES spectra and cannot be analyzed.

Table 2.2: Line list

Species	λ (nm)*	$E_{\rm low}$ (eV)†	$\log gf$‡	vdW §
Na I	1074.9393	3.191	−1.294	N/A
Na I	1083.7814	3.617	−0.503	N/A
Na I	1268.2639	3.617	−0.043	−6.653
Mg I	1183.1409	4.346	−0.333	−7.192
K I	1177.2861	1.617	−0.450	−7.326
K I	1177.6061	1.617	0.510	−7.326

Table 2.2 (Continued)

Species	λ (nm)*	$E_{\rm low}$ (eV)†	$\log gf$‡	vdW §
K I	1243.5675	1.610	−0.439	−7.022
Ca I	1034.6654	2.932	−0.300	−7.480
Ca I	1195.9227	4.131	−0.849	−7.300
Ca I	1281.9551	3.910	−0.765	−7.520
Ca I	1282.7375	3.910	−0.997	−7.520
Ca I	1283.0568	3.910	−1.478	−7.520
Ca I	1291.2601	4.430	−0.224	−7.710
Ca I	1303.7119	4.441	−0.064	−7.710
Ca I	1306.1457	4.441	−1.092	−7.710
Ti I	967.8197	0.836	−0.804	−7.800
Ti I	969.1530	0.813	−1.610	−7.800
Ti I	972.1626	1.503	−1.181	−7.780
Ti I	973.1075	0.818	−1.206	−7.800
Ti I	974.6277	0.813	−1.306	−7.800
Ti I	977.2980	0.848	−1.581	−7.800
Ti I	979.0372	0.826	−1.444	−7.800
Ti I	983.4836	1.887	−1.130	−7.634
Ti I	1000.5831	2.160	−1.210	−7.780
Ti I	1005.1583	1.443	−1.930	−7.780
Ti I	1039.9651	0.848	−1.539	−7.810
Ti I	1058.7533	0.826	−1.775	−7.810
Ti I	1066.4544	0.818	−1.915	−7.810
Ti I	1077.7818	0.818	−2.666	−7.810
Ti I	1178.3767	1.443	−2.170	−7.790
Ti I	1180.0415	1.430	−2.280	−7.790
Ti I	1189.6132	1.430	−1.730	−7.790
Ti I	1281.4983	2.160	−1.390	−7.750
Ti I	1282.5180	1.460	−1.190	−7.790
Ti I	1292.3433	2.154	−1.560	−7.750
Cr I	1080.4319	3.011	−1.562	−7.780

Table 2.2 (Continued)

Species	λ (nm)*	$E_{\rm low}$ (eV)†	$\log gf$‡	vdW §
Cr I	1082.4625	3.013	−1.520	−7.780
Cr I	1291.3622	2.708	−1.779	−7.800
Cr I	1294.0559	2.710	−1.896	−7.800
Mn I	1290.3289	2.114	−1.070	N/A
Mn I	1297.9459	2.888	−1.090	N/A
Fe I	1038.1843	2.223	−4.148	−7.800
Fe I	1039.8643	2.176	−3.393	−7.800
Fe I	1061.9630	3.267	−3.127	−7.780
Fe I	1078.6004	3.111	−2.567	−7.790
Fe I	1088.4739	2.845	−3.604	−7.810
Fe I	1089.9284	3.071	−2.694	−7.790
Fe I	1142.5447	2.198	−2.700	−7.820
Fe I	1161.0750	2.198	−2.009	−7.820
Fe I	1164.1446	2.176	−2.214	−7.820
Fe I	1178.6490	2.832	−1.574	−7.820
Fe I	1256.0432	2.279	−3.626	−7.820
Fe I	1288.3289	2.279	−3.458	−7.820

* Wavelength in vacuum † Lower excitation potential

‡ Oscillator strength § Van der Waals damping parameter

Owing to the large surface gravity, the pressure broadening (van der Waals broadening) induced mainly by neutral hydrogen and molecular hydrogen works strongly in M dwarfs. The pressure broadening dominates the total width of many lines and cannot be ignored, even in relatively weak lines. We treated the broadening with the van der Waals (vdW) damping parameters calculated by Barklem et al. (2000) if the data were incorporated in the VALD line lists. For the absorption lines of Na and Mn without the reported damping data, we adopted the hydrogenic approximation of Unsöld (1955) with an enhancement factor, which is introduced conventionally to model the wings correctly. The enhancement factors applied in previous studies are mostly between 1.0 and 5.0. We found that an enhancement factor of 1.0–1.9

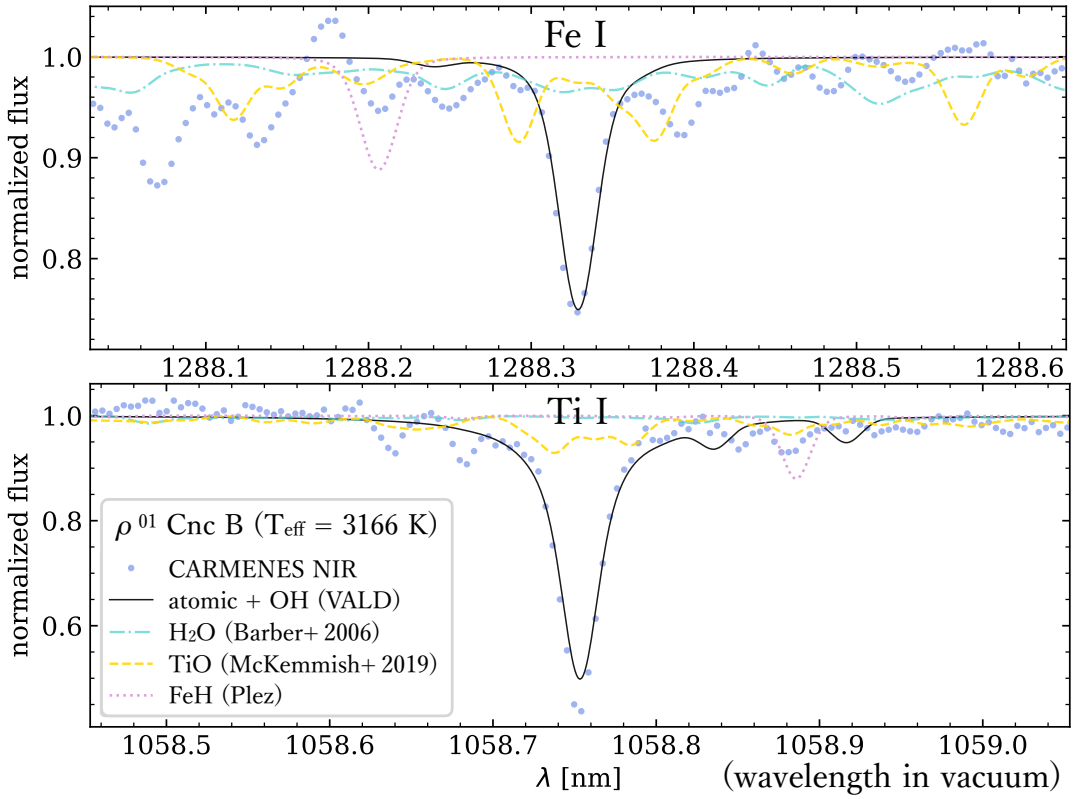

Figure 2.1: Two atomic lines used in the analysis of ρ^{01} Cnc B ($T_{\rm eff}$ = 3166 K) and possible molecular lines in the vicinity. The solid-line synthetic spectrum (black line) is based on the stellar parameters and calculated using the line list from VALD, which includes atomic lines and OH lines. The other synthetic spectra are calculated with the H_2O line list of Barber et al. (2006) (cyan dot-dashed line), the TiO line list of McKemmish et al. (2019) (yellow dashed line), and the FeH line list of Plez (pink dotted line). The observed spectrum of ρ^{01} Cnc B is shown by blue dots.

closely reproduces the abundance results for the other elements obtained by the analysis using the vdW damping parameters of Barklem et al. (2000). We adopted 1.4 for Mn based on the empirical approximation by Ryan (1998), and 1.0 for Na because Weidemann (1955) demonstrated that the lines of alkali metals can be reproduced well without an enhancement factor. We confirmed that these values are adequate for visual comparison between the line profiles of the models and observed data. When we varied the enhancement factor within 1.0–1.9, the variations in the resulting abundances from those lines were at most 0.05 dex.

We ascertained that the contamination of stellar H_2O lines is negligible in the wavelength region used in the present work, although the *K*-band spectra and some parts of the *H*-band spectra of M dwarfs were reported to be affected by numerous weak lines of H_2O changing the apparent continuum level (Tsuji et al. 2015). Examples of the small contribution of H_2O lines around the atomic lines used for mid-M dwarfs are shown in Fig. 2.1. For each panel, approximately 300 H_2O lines within 0.6 nm of the atomic line are included in the calculation. In the spectra of mid-M dwarfs, the depths of the most H_2O lines are significantly less than 1 % (and at most ~5 %) of the continuum level, and they are sufficiently sparse not to affect the continuum flux drastically. The contribution of H_2O is even smaller in the spectra of early-M dwarfs.

The possible contributions of the TiO and FeH lines are also shown in Fig. 2.1. Most of the relatively strong (depth ~10 %) TiO lines seen in the synthetic spectra were not found in the observed data. The data of TiO lines in the near-infrared wavelength range are not sufficiently accurate for use in the analysis of high-resolution spectra, although we employed the up-to-date TiO line list, Toto (McKemmish et al. 2019). The figure provides a conservative estimate indicating that the possible molecular lines do not have a significant effect on our analysis of atomic lines.

2.3.4 Equivalent width measurement

We measured the EWs (e.g., Nissen & Gustafsson 2018) of the absorption lines using the PyRAF task "splot" by fitting Gaussian profiles to the observed line profiles. For strong lines with wide wings that cannot be reproduced sufficiently by Gaussian profiles, we fitted Voigt profiles instead. For the apparently overlapping absorption lines, we simultaneously fitted multiple Gaussian and/or Voigt profiles using the

deblend fitting mode of splot. In the process of profile fitting, we redetermined the continuum level by visually checking the spectral range of more than ~2 nm around the absorption line.

Although sodium is one of the most important elements in the temperature regime of M dwarfs (see Section 2.5.1 for details), there are no absorption lines suitable for the above procedure for EW measurement. The self-blending of multiple Na I lines, the heavy blending of other spectral lines, or the overly broad wings deviated from the Gaussian or Voigt profiles hindered measurement with splot. Instead, we determined the EWs of Na I lines with model fitting, treating the Na abundances and Gaussian width (representing the spectral resolution and macro-turbulence) as free parameters. An example of the Na I line at 1083.78 nm is shown in Fig. 2.2. This apparently single line actually consists of three lines, which are simultaneously used to fit the model spectra. The wavelengths used in the fitting are selected to cover from the line wings to the core while excluding the blending of unidentified absorption lines, telluric contamination, significant asymmetry, and outliers. Note that the exclusion of the outliers does not significantly change the final result.

We also applied the fitting of model spectra to the manganese lines to consider the hyperfine structure (hfs) splitting. We employed the experimental oscillator strengths (gf-values) of individual hfs components reported by Blackwell-Whitehead et al. (2011) to reproduce the broad line profile of the Mn I lines that could not be fitted satisfactorily by model spectra, calculated by assuming it to be a single line. Figure 2.3 shows the spectral fitting of the Mn I line at 1297.95 nm of ρ^{01} Cnc B with the contribution of each hfs component illustrated.

For G 102-4, the line profiles are generally broad and the best-fit value of the Gaussian width is approximately 12 km s^{-1}, although the other objects indicate a width of ~5 km s^{-1}. This line broadening suggests a large rotational velocity. However, the line profile is well approximated by a Gaussian profile in the quality of our spectra; hence, we did not apply a more detailed rotational profile fitting in the present work. We also found that G 102-4 exhibits Hα emission in the visible data of CARMENES, which indicates high magnetic activity and supports the possibility of rapid rotation.

All the measured EWs are listed in Table 2.3.

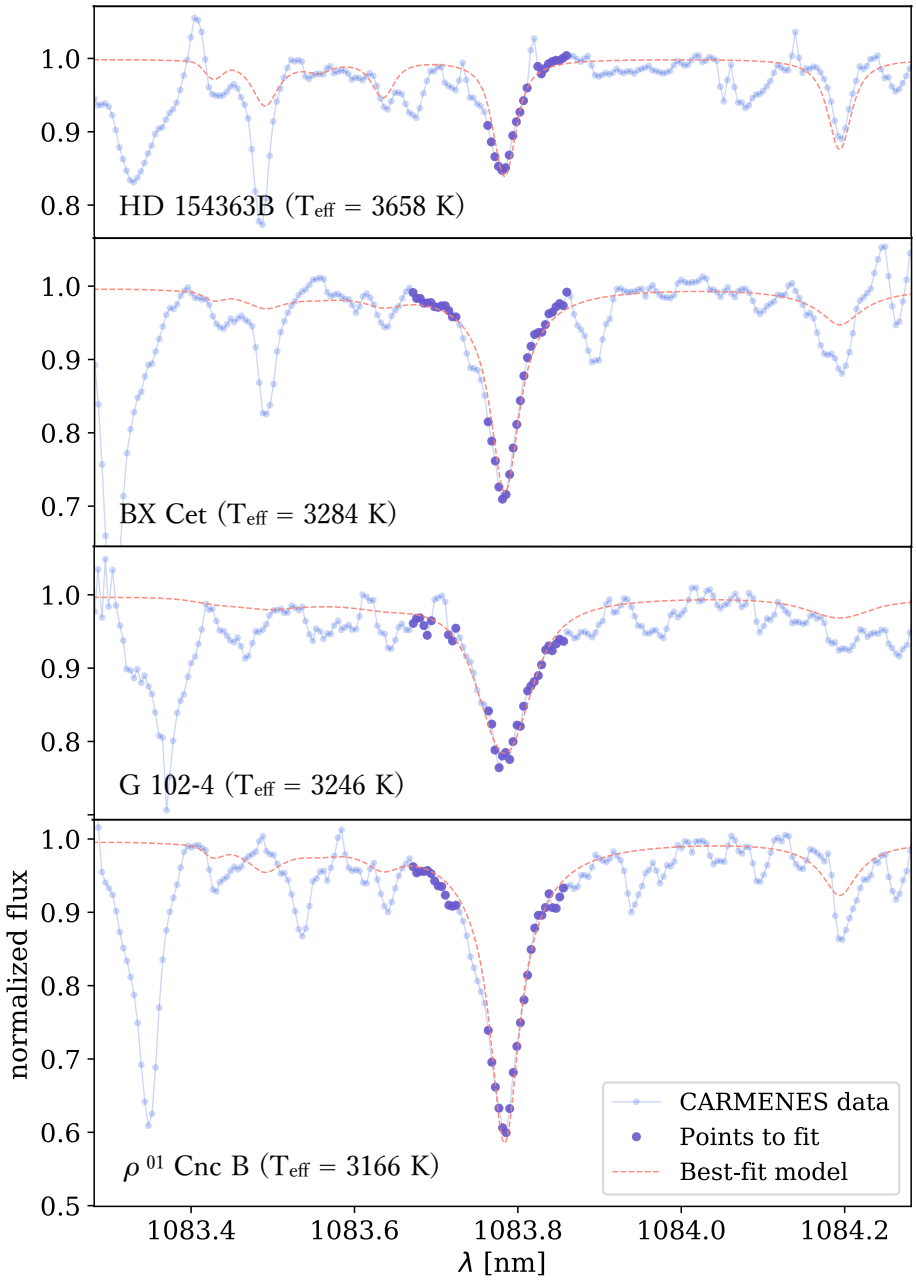

Figure 2.2: CARMENES spectra (blue and purple dots) and synthetic model spectra calculated with the best-fit abundances (red dashed lines) around the Na I line at 1083.78 nm. The larger purple dots are the data used for the fitting (1083.67–1083.86 nm). The wavelength range blended with unidentified lines (1083.73–1083.76 nm) and some outliers were excluded from the fitting.

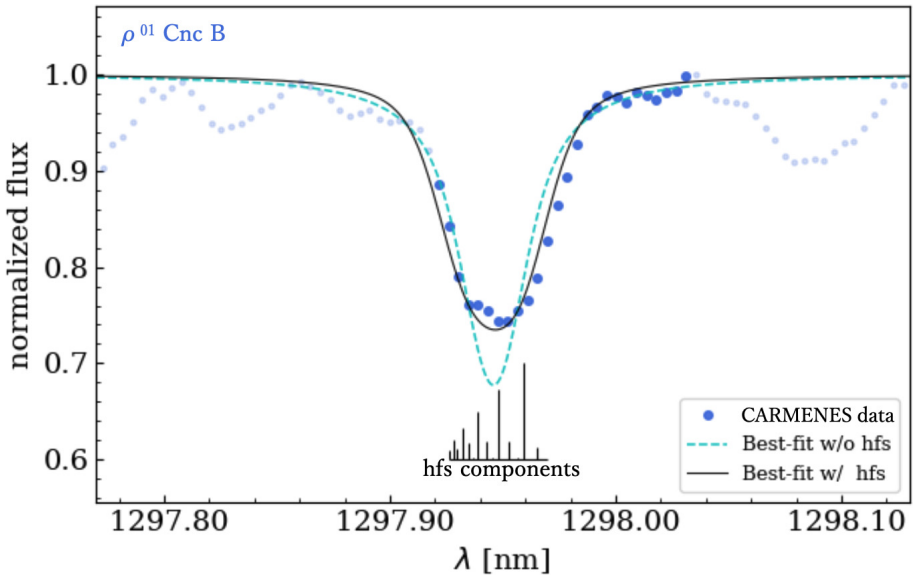

Figure 2.3: Comparison between the best-fit model spectra calculated with and without considering the hfs splitting of the Mn I line at 1297.9 nm (black solid line and cyan dashed line, respectively). The blue dots are the CARMENES spectra of ρ^{01} Cnc B used for the fitting (the small pale dots are not used because of the line blending or uncertain continuum level). The positions of the hfs components are represented by vertical lines, the lengths of which are proportional to the gf-values.

Table 2.3: Measured EWs in units of [pm]

Species	λ (nm)*	HD 233153	HD 154363B	BX Cet	G 102-4	ρ^{01} Cnc B	BD-02 2198†
Na I	1074.9393	0.00	2.27	0.00	0.00	0.00	4.68
Na I	1083.7814	0.00	4.99	14.14	16.15	25.08	7.03
Na I	1268.2639	30.97	0.00	0.00	0.00	0.00	0.00
Mg I	1183.1409	98.28	106.90	57.98	65.08	52.86	114.30
K I	1177.2861	17.52	19.71	0.00	50.90	0.00	26.51
K I	1177.6061	0.00	0.00	0.00	119.30	0.00	0.00
K I	1243.5675	27.63	24.99	51.23	0.00	0.00	32.84
Ca I	1034.6654	103.70	82.63	0.00	0.00	0.00	98.95
Ca I	1195.9227	0.00	6.84	0.00	0.00	0.00	12.48
Ca I	1281.9551	21.85	0.00	20.16	0.00	22.04	0.00
Ca I	1282.7375	15.36	8.78	11.34	0.00	12.90	18.24
Ca I	1283.0568	6.78	4.63	5.00	0.00	7.30	7.34
Ca I	1291.2601	9.65	0.00	0.00	0.00	0.00	0.00
Ca I	1303.7119	13.93	10.52	0.00	11.19	11.55	15.18
Ca I	1306.1457	3.55	2.96	0.00	2.45	3.31	3.46
Ti I	967.8197	51.90	44.03	47.25	59.65	45.42	51.29
Ti I	969.1530	0.00	0.00	0.00	33.29	0.00	0.00
Ti I	972.1626	14.65	11.89	12.02	0.00	14.20	14.73
Ti I	973.1075	0.00	0.00	0.00	42.84	32.81	0.00
Ti I	974.6277	0.00	0.00	0.00	40.96	0.00	0.00
Ti I	977.2980	25.06	22.87	25.54	23.00	23.96	26.39
Ti I	979.0372	0.00	27.21	0.00	0.00	0.00	30.08
Ti I	983.4836	0.00	9.44	7.61	4.54	6.29	0.00
Ti I	1000.5831	8.43	5.00	3.99	2.88	0.00	6.90
Ti I	1005.1583	0.00	6.80	5.79	0.00	0.00	0.00
Ti I	1039.9651	25.15	26.02	28.36	33.42	30.11	27.34
Ti I	1058.7533	24.98	26.44	25.66	28.47	25.04	27.39
Ti I	1066.4544	25.39	24.30	24.91	25.67	25.00	25.54
Ti I	1077.7818	14.18	9.27	12.79	0.00	0.00	15.05
Ti I	1178.3767	0.00	0.00	6.29	5.37	6.73	0.00
Ti I	1180.0415	8.68	0.00	7.57	0.00	6.96	0.00
Ti I	1189.6132	13.38	0.00	0.00	14.95	11.56	13.93
Ti I	1281.4983	9.37	6.09	5.30	0.00	5.74	0.00
Ti I	1282.5180	0.00	26.36	25.36	26.18	25.04	0.00
Ti I	1292.3433	6.17	0.00	0.00	0.00	0.00	0.00
Cr I	1080.4319	4.37	0.00	0.00	1.60	2.21	4.36

Table 2.3 (Continued)

Species	λ (nm)*	HD 233153	HD 154363B	BX Cet	G 102-4	ρ^{01} Cnc B	BD-02 2198†
Cr I	1082.4625	4.63	2.10	1.98	0.00	0.00	0.00
Cr I	1291.3622	10.68	0.00	0.00	0.00	0.00	12.66
Cr I	1294.0559	0.00	3.92	3.85	0.00	0.00	10.03
Mn I	1290.3289	44.08	23.85	0.00	28.83	0.00	41.86
Mn I	1297.9459	17.66	0.00	10.66	12.25	12.65	0.00
Fe I	1038.1843	5.27	2.38	2.03	0.00	2.45	4.26
Fe I	1039.8643	10.61	6.28	7.32	6.76	9.13	11.84
Fe I	1061.9630	1.99	0.00	0.00	0.00	0.00	1.78
Fe I	1078.6004	6.41	3.81	3.23	0.00	4.62	6.33
Fe I	1088.4739	4.19	0.00	0.00	0.00	0.00	0.00
Fe I	1089.9284	4.02	2.39	0.00	3.38	2.65	7.06
Fe I	1142.5447	20.96	16.35	0.00	0.00	0.00	0.00
Fe I	1161.0750	35.89	26.66	0.00	0.00	0.00	0.00
Fe I	1164.1446	0.00	28.31	0.00	0.00	0.00	0.00
Fe I	1178.6490	27.76	0.00	0.00	0.00	0.00	0.00
Fe I	1256.0432	7.66	3.59	0.00	0.00	0.00	0.00
Fe I	1288.3289	0.00	10.87	8.47	0.00	10.85	0.00

* Wavelength in vacuum † The analysis of BD-02 2198 is described in 2.7.

2.3.5 Abundance determination

We calculated the theoretical EWs from the synthetic spectra described in Section 2.3.2.

In the first step, we adopted a model atmosphere with the solar composition (Asplund et al. 2009). We also assumed all elemental abundances to be solar values when initially calculating the synthetic spectra. We varied the elemental abundance [X/H] in the spectral synthesis until the theoretical EW of the i th line of the element X matched the observed EW$_i$. We determined the elemental abundance [X/H]$_i$ for each absorption line i, and obtained the abundance of the element X by averaging [X/H]$_i$ from all lines of X.

In the second step, we updated the model atmosphere by adopting the overall metallicity ([M/H]) that corresponds to the Fe abundance ratio ([Fe/H]) determined by the previous step. In the spectral synthesis, we adopted the individual elemental abundances determined by the previous step as the assumed values. For the abundances

of α elements that were not measured in the present work (e.g., C, O, Si, S), we adopted the average of the abundance ratios of measured α elements (e.g., Mg, Ca; we did not use Ti because of the large uncertainty discussed in Section 2.5.2). In addition, we assumed the abundance ratios ([X/H]) of all the other unmeasured elements to be identical to that of iron ([Fe/H]). Based on these settings, we redetermined the abundances of individual elements in the same manner as in the first step.

Based on these results, we again updated the model atmosphere and elemental abundances assumed in the next step. These steps were iterated until the resulting [Fe/H] agreed with the [M/H] assumed in the model atmosphere within 0.005 dex to obtain the final results.

2.3.6 Error estimation

We calculated the total error of the abundance for each element as the quadrature sum of four types of errors. The error size from each source is tabulated in Table 2.4, and the contribution of each to the total error is described in Section 2.4.1.

(1) Errors due to random noise in spectral lines, uncertainties in the line data, and measurement uncertainty ($\sigma_{\rm SEM}$). These are estimated as the standard error of the mean (SEM) by dividing the standard deviation of the resulting [X/H] from individual absorption lines by the square root of the number of absorption lines used in the analysis ($N_{\rm line}$). For the species for which we used fewer than four absorption lines, we substituted the standard deviation of Fe abundance and divided it by the square root of the number of lines of the species. This is because the number of Fe I lines is at least four, with the exception of G 102-4. We used only two Fe I lines for G 102-4, but the standard deviation from the two lines is comparable to the standard deviation from the results of five Fe I lines for another mid-M dwarf, ρ^{01} Cnc B.

(2) Errors propagated from uncertainties of the three stellar parameters: $T_{\rm eff}$, $\log g$, and ξ ($\sigma_{T_{\rm eff}}$, $\sigma_{\log g}$, and σ_{ξ}, respectively). We performed the entire analysis procedure by assuming the minimum or maximum value in the uncertainty range for each parameter to obtain the change in the results as the error.

(3) Errors caused by uncertainties in the abundances of other elements ($\sigma_{\rm OE}$). Here, we conservatively adopted 0.2 dex as the uncertainties, referring to the errors due to the other sources (1), (2), and (4). For each element, we repeated the entire procedure

assuming the abundances of the other elements homogeneously to be 0.2 dex higher or lower than our final results. We adopted the variation in the result as the error size.

(4) Errors arising from the uncertainty of the continuum-level determination due to noise or possible weak features around the spectral lines ($\sigma_{\rm cont}$). We estimated the error by abundance analysis using the same procedure by changing the continuum level. The possible ranges of the continuum level were estimated by visual inspection of the Fe I and Na I lines. The rate of change in EW when the continuum level was varied within each of these ranges was found to correlate with the EW value of the absorption line. To estimate the rate of change for all the other lines based on this correlation, we performed linear fitting to obtain the empirical equations as follows:

$$\Delta{\rm EW}_{\rm min}/{\rm EW} = -0.145 + 0.0093\,{\rm EW}, \quad (2.1)$$

$$\Delta{\rm EW}_{\rm max}/{\rm EW} = 0.230 - 0.0105\,{\rm EW}, \quad (2.2)$$

$$\Delta{\rm EW}_{\rm min}/{\rm EW} = -0.049 + 0.0001\,{\rm EW}, \quad (2.3)$$

$$\Delta{\rm EW}_{\rm max}/{\rm EW} = 0.157 - 0.0042\,{\rm EW}, \quad (2.4)$$

where the EWs are measured in units of pm. $\Delta{\rm EW}_{\rm min}$ and $\Delta{\rm EW}_{\rm max}$ are the changes in EWs when the minimum and maximum possible continuum levels are adopted, respectively. Equations (2.1) and (2.2) are valid for relatively weak lines with EWs less than ~10 pm, and (2.3) and (2.4) correspond to stronger lines. We verified from the Fe I and Na I lines that the departure of the estimate by the empirical relation from that by the visual inspection for each line is almost less than 10 %, which has a negligible effect on the final error size.

We applied these equations to all absorption lines to estimate the errors associated with the continuum level determination. A $\Delta{\rm EW}_{\rm min}/{\rm EW}$ or $\Delta{\rm EW}_{\rm max}/{\rm EW}$ value of 0.05 was adopted in the case for which the values obtained from the above equations were smaller than 0.05. We took the average of the errors arising from $\Delta{\rm EW}_{\rm min}$ and $\Delta{\rm EW}_{\rm max}$ as the error for each line. We calculated the root mean square (RMS) of the errors for all lines of an element and divided it by the square root of the number of absorption lines to obtain the standard error of the resulting abundance of the element. The rate of change in EW ranged within 5–20 % and the resulting abundance error was sufficiently small to be overwhelmed by other error sources.

2.4 Results

We present the abundances obtained for each object in Table 2.4 with the contributions of individual error sources.

2.4.1 Contributions of individual error sources

We found that the error source that dominates the total error budget varies depending on the elements and objects. In most cases, $\sigma_{\rm SEM}$, $\sigma_{\rm OE}$, and/or $\sigma_{\log g}$ are dominant, whereas $\sigma_{T_{\rm eff}}$ and $\sigma_{\rm cont}$ have minor contributions. This is different from the case of the chemical analysis of FGK dwarfs, in which the uncertainty of $T_{\rm eff}$ has a large impact on the derived elemental abundances. The fact that $\sigma_{\rm OE}$ significantly contributes to the total error demonstrates the sensitivity of the line strengths to the abundance of elements other than the species responsible for the absorption, which is a phenomenon unique to M dwarfs (see Section 2.5.1). σ_{ξ} has negligible contributions through all the elements of our objects. The line broadening is controlled by other mechanisms in the temperature regime of M dwarfs. One of these is pressure broadening, the treatment of which is described in Section 2.3.3. The pressure broadening is subject to $\log g$, which is a reason for the large values of $\sigma_{\log g}$. Note that the change in $\log g$ changes the ionization rate of some elements, which also changes the abundance results from neutral lines in the same direction as the effect of pressure broadening.

For the two early-M dwarfs with temperatures ~3700 K, $\sigma_{\rm SEM}$ and $\sigma_{\rm OE}$ are dominant for most elements, and $\sigma_{\log g}$ comparably contributes to the total errors for certain elements (Mg, K, Ca, and Ti). The relatively small $\sigma_{\log g}$ of HD 233153 is attributed to the relatively small uncertainty of $\log g$ for the object.

For the three mid-M dwarfs with temperatures of ~3200 K, the principal error source is $\sigma_{\rm OE}$ or $\sigma_{\log g}$ for many elements. The absolute sizes of $\sigma_{\rm OE}$ are noticeably larger in the mid-M dwarfs (0.08–0.31) than in the early-M dwarfs (0.02–0.16). The cause of this result is discussed in Section 2.5.1. The absolute sizes of $\sigma_{\log g}$ are also larger in the mid-M dwarfs, and their trend found between different elements is almost the same as that found in the early-M dwarfs except for Ti, for which $\sigma_{\log g}$ is more significant in the mid-M dwarfs. This is partly because the pressure broadening becomes dominant in the Ti I line profiles as the temperature drops. The main reason,

Table 2.4: Abundance results with the individual contribution of each error source

Object	Element	[X/H]	$N_{\rm line}$	$\sigma_{\rm SEM}$	$\sigma_{T_{\rm eff}}$	$\sigma_{\log g}$	σ_{ξ}	$\sigma_{\rm OE}$	$\sigma_{\rm cont}$	$\sigma_{\rm Total}$
HD 233153	Na	0.06	1	0.20	$0.00^{\downarrow}$	$0.02^{\downarrow}$	0.00	$0.02^{\uparrow}$	0.03	0.20
	Mg	0.09	1	0.20	$0.08^{\downarrow}$	$0.02^{\downarrow}$	$0.01^{\uparrow}$	$0.09^{\uparrow}$	0.05	0.24
	K	0.15	2	0.14	$0.02^{\uparrow}$	$0.04^{\downarrow}$	$0.02^{\downarrow}$	$0.05^{\uparrow}$	0.04	0.16
	Ca	0.22	7	0.08	$0.01^{\downarrow}$	$0.02^{\downarrow}$	$0.01^{\downarrow}$	$0.05^{\uparrow}$	0.03	0.10
	Ti	0.36	12	0.04	$0.04^{\downarrow}$	$0.01^{\downarrow}$	$0.04^{\downarrow}$	$0.14^{\uparrow}$	0.02	0.16
	Cr	0.23	3	0.11	$0.04^{\downarrow}$	$0.01^{\uparrow}$	$0.03^{\downarrow}$	$0.08^{\uparrow}$	0.06	0.16
	Mn	0.31	2	0.14	$0.05^{\downarrow}$	$0.01^{\downarrow}$	$0.02^{\downarrow}$	$0.10^{\uparrow}$	0.04	0.18
	Fe	0.14	10	0.06	$0.04^{\downarrow}$	$0.01^{\uparrow}$	$0.03^{\downarrow}$	$0.09^{\uparrow}$	0.03	0.13
HD 154363B	Na	−0.41	2	0.13	$0.04^{\uparrow}$	$0.03^{\downarrow}$	$0.01^{\downarrow}$	$0.02^{\uparrow}$	0.03	0.15
	Mg	0.17	1	0.19	$0.04^{\downarrow}$	$0.11^{\downarrow}$	$0.01^{\downarrow}$	$0.16^{\uparrow}$	0.05	0.27
	K	−0.05	2	0.13	$0.07^{\uparrow}$	$0.11^{\downarrow}$	$0.02^{\downarrow}$	$0.06^{\uparrow}$	0.03	0.20
	Ca	−0.13	6	0.05	$0.03^{\uparrow}$	$0.07^{\downarrow}$	$0.01^{\downarrow}$	$0.07^{\uparrow}$	0.03	0.12
	Ti	0.05	13	0.03	$0.00^{\uparrow}$	$0.09^{\downarrow}$	$0.04^{\downarrow}$	$0.19^{\uparrow}$	0.02	0.22
	Cr	−0.36	2	0.13	$0.01^{\downarrow}$	0.00	$0.02^{\downarrow}$	$0.10^{\uparrow}$	0.06	0.18
	Mn	−0.47	1	0.19	$0.01^{\uparrow}$	$0.09^{\downarrow}$	$0.03^{\downarrow}$	$0.15^{\uparrow}$	0.05	0.26
	Fe	−0.34	9	0.06	$0.00^{\downarrow}$	$0.04^{\downarrow}$	$0.03^{\downarrow}$	$0.13^{\uparrow}$	0.03	0.15
BX Cet	Na	−0.10	1	0.02	$0.08^{\uparrow}$	$0.07^{\downarrow}$	$0.00^{\downarrow}$	$0.08^{\uparrow}$	0.03	0.14
	Mg	−0.17	1	0.02	$0.04^{\uparrow}$	$0.11^{\downarrow}$	$0.01^{\downarrow}$	$0.19^{\uparrow}$	0.04	0.23
	K	−0.18	1	0.02	$0.16^{\uparrow}$	$0.14^{\downarrow}$	$0.01^{\downarrow}$	$0.10^{\uparrow}$	0.04	0.24
	Ca	−0.14	3	0.01	$0.06^{\uparrow}$	$0.07^{\downarrow}$	$0.01^{\downarrow}$	$0.13^{\uparrow}$	0.03	0.16
	Ti	0.00	14	0.03	$0.10^{\uparrow}$	$0.13^{\downarrow}$	$0.02^{\downarrow}$	$0.27^{\uparrow}$	0.02	0.32
	Cr	−0.26	2	0.02	$0.04^{\uparrow}$	$0.03^{\downarrow}$	$0.01^{\downarrow}$	$0.12^{\uparrow}$	0.06	0.15
	Mn	−0.08	1	0.02	$0.06^{\uparrow}$	$0.07^{\downarrow}$	$0.01^{\downarrow}$	$0.16^{\uparrow}$	0.06	0.20
	Fe	−0.21	4	0.01	$0.05^{\uparrow}$	$0.05^{\downarrow}$	$0.02^{\downarrow}$	$0.14^{\uparrow}$	0.04	0.16
G 102-4	Na	−0.04	1	0.14	$0.08^{\uparrow}$	$0.12^{\downarrow}$	$0.00^{\downarrow}$	$0.09^{\uparrow}$	0.04	0.22
	Mg	−0.02	1	0.14	$0.04^{\uparrow}$	$0.18^{\downarrow}$	$0.01^{\downarrow}$	$0.20^{\uparrow}$	0.04	0.31
	K	−0.03	2	0.10	$0.18^{\uparrow}$	$0.26^{\downarrow}$	$0.01^{\downarrow}$	$0.13^{\uparrow}$	0.03	0.36
	Ca	−0.26	2	0.10	$0.03^{\uparrow}$	$0.08^{\downarrow}$	$0.00^{\downarrow}$	$0.11^{\uparrow}$	0.04	0.18
	Ti	0.03	13	0.05	$0.10^{\uparrow}$	$0.23^{\downarrow}$	$0.02^{\downarrow}$	$0.28^{\uparrow}$	0.02	0.38
	Cr	−0.31	1	0.14	$0.03^{\uparrow}$	$0.04^{\downarrow}$	$0.01^{\downarrow}$	$0.12^{\uparrow}$	0.08	0.21
	Mn	−0.17	2	0.10	$0.08^{\uparrow}$	$0.16^{\downarrow}$	$0.02^{\downarrow}$	$0.18^{\uparrow}$	0.04	0.28
	Fe	−0.18	2	0.10	$0.05^{\uparrow}$	$0.09^{\downarrow}$	$0.02^{\downarrow}$	$0.14^{\uparrow}$	0.06	0.21
ρ^{01} Cnc B	Na	0.42	1	0.13	$0.14^{\uparrow}$	$0.19^{\downarrow}$	$0.02^{\downarrow}$	$0.16^{\uparrow}$	0.03	0.31
	Mg	0.23	1	0.13	$0.08^{\uparrow}$	$0.20^{\downarrow}$	$0.02^{\downarrow}$	$0.17^{\uparrow}$	0.04	0.30
	Ca	0.23	5	0.08	$0.08^{\uparrow}$	$0.15^{\downarrow}$	$0.02^{\downarrow}$	$0.14^{\uparrow}$	0.03	0.24
	Ti	0.59	13	0.03	$0.17^{\uparrow}$	$0.31^{\downarrow}$	$0.06^{\downarrow}$	$0.31^{\uparrow}$	0.02	0.48
	Cr	0.14	1	0.13	$0.06^{\uparrow}$	$0.09^{\downarrow}$	$0.02^{\downarrow}$	$0.12^{\uparrow}$	0.09	0.22
	Mn	0.43	1	0.13	$0.11^{\uparrow}$	$0.18^{\downarrow}$	$0.04^{\downarrow}$	$0.17^{\uparrow}$	0.06	0.31
	Fe	0.26	5	0.06	$0.09^{\uparrow}$	$0.13^{\downarrow}$	$0.04^{\downarrow}$	$0.15^{\uparrow}$	0.04	0.23

The calculation of $\sigma_{\rm SEM}$ is depicted in (1) of Section 2.3.6. Those of $\sigma_{T_{\rm eff}}$, $\sigma_{\log g}$, and σ_{ξ} are described in (2). Those of $\sigma_{\rm OE}$ and $\sigma_{\rm cont}$ are described in (3) and (4), respectively. $\sigma_{\rm Total}$ is the quadrature sum of all errors. $^{\uparrow\downarrow}$: For the errors caused by the uncertainty of stellar parameters ($\sigma_{T_{\rm eff}}$, $\sigma_{\log g}$, and σ_{ξ}, and $\sigma_{\rm OE}$), those marked with $^{\uparrow}$ show an upward change in the results when the parameters are increased. Those with $^{\downarrow}$ show the opposite.

Table 2.5: Error-weighted RMS of the abundance differences of the M dwarfs from their G/K-type primaries for each element or object

Species or object	Error-weighted RMS of differences
Na	0.07
Mg	0.33
Ca	0.17
Ti	0.21
Cr	0.17
Mn	0.29
Fe	0.15
HD 233153	0.23
HD 154363B	0.30
BX Cet	0.13
G 102-4	0.16
ρ^{01} Cnc B	0.12

Potassium is excluded because its abundances for the primary stars were not reported.

however, is that the change in assumed $\log g$ alters the abundances of other elements assumed in the analysis, which causes a substantial change in the final Ti abundances (see Section 2.5.2). The total errors of [Ti/H] for all the three mid-M dwarfs are larger than 0.3 dex. We discuss the difficulty of constraining [Ti/H] in more detail in Section 2.5.2. $\sigma_{T_{\rm eff}}$ contributes to the total errors as much as the aforementioned two sources for certain elements, especially Na, K, and Ti. $\sigma_{\rm SEM}$ is also a main contributor to the total errors for many elements of G 102-4 and ρ^{01} Cnc B. $\sigma_{\rm cont}$ is almost negligible in all elements except for Cr, where it is comparable to or larger than the errors of other sources, e.g., $\sigma_{\log g}$.

2.4.2 Consistency check with G/K-type primaries

Figure 2.4 shows the comparison of chemical abundances between our results for the M-dwarf secondaries and the values for the G/K-type primaries reported by Montes et al. (2018) (hereafter Mon18), who determined the abundances using high-resolution visible spectra. The K abundances of our results are plotted here, to compare the abundance ratios to those of other elements, although the abundance of this element for the primaries was not determined by Mon18. The abundances of the other seven elements determined for M dwarfs generally agree with those of the primaries within

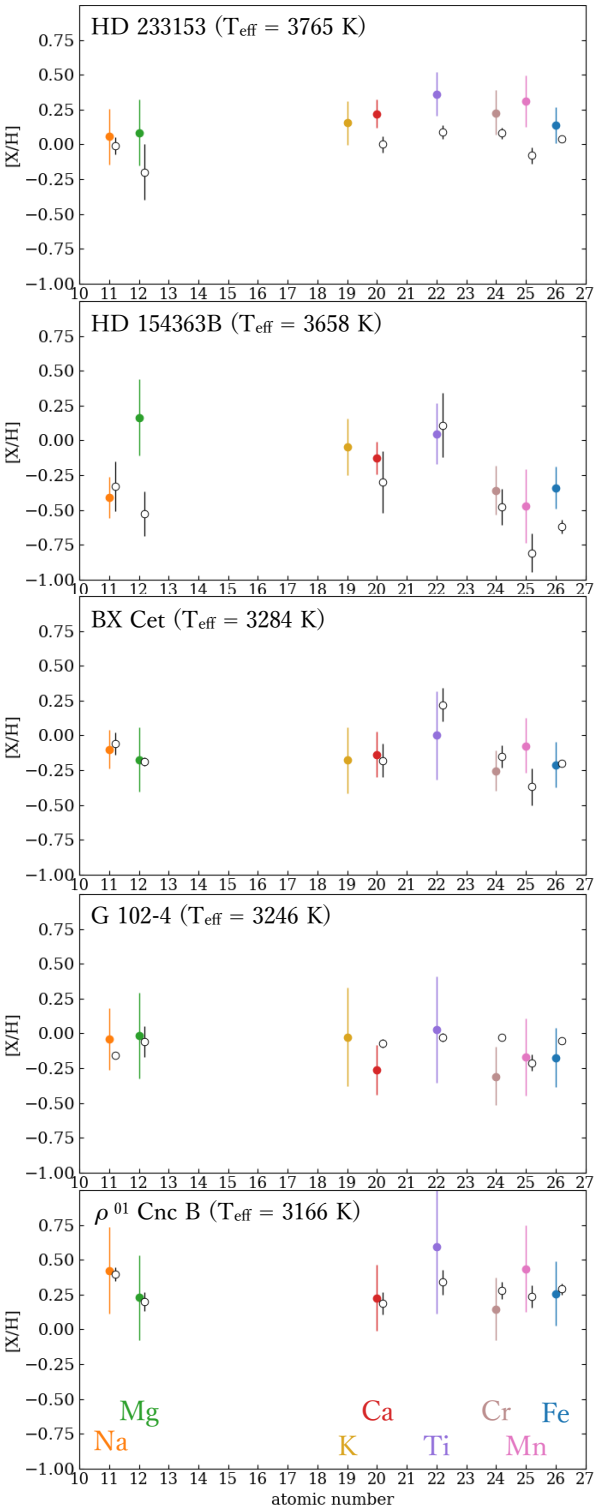

Figure 2.4: Abundance ratios [X/H] of individual elements for each binary pair as a function of atomic number. The color-filled circles represent the abundances of the M-dwarf secondaries we determined, and the black open circles (horizontally shifted for clarity) represent those of the G/K-type primaries reported by Montes et al. (2018). The error bars for M dwarfs correspond to $\sigma_{\rm Total}$ in Table 2.4, whereas those for the G/K-type primaries are the uncertainties reported by Montes et al. (2018), which are calculated similarly to the $\sigma_{\rm SEM}$ in our analysis.

the error margins. Note that the error bars for the abundances of the primaries reported by Mon18 contain only the line-to-line scatters divided by the square root of the number of spectral lines used in the analysis. Mon18 specifically compiled the abundances of FGK stars in binary or multiple systems with M dwarfs. We chose Mon18 for comparison because it was the most recent work to cover all the primary stars of the binary systems studied here. Mon18 reported that their results agreed well with previously published ones and no significant offset was detected.

To examine the consistency between our resulting abundances of M dwarfs and the reported abundances of their primaries, we calculated the RMS of the abundance differences between an M dwarf and its primary for each element (five binary pairs) and for each object (seven elements). In the process to obtain the mean, we gave a weight to each binary pair computed from the inverse of the quadrature sum of errors for both binary components. The calculated values are given in Table 2.5. The derived values are similar to or slightly smaller than the sizes of $\sigma_{\rm Total}$ in Table 2.4, typically ranging from 0.15 to 0.25. The exceptions are those for Mg, Mn, and HD 154363B, for which the reasons are examined below.

As shown in Fig. 2.4, the large difference in abundance of Mg is solely due to the large difference seen in HD 154363B (see Section 2.5.3). The abundances of Mn, in contrast, appear to be systematically higher in M dwarfs than in the primaries. Note that the obtained Mn abundance is even higher if we analyze the Mn I lines without considering the hfs. Mon18 mentioned that the general trend of their [Mn/Fe] is not consistent with the Galactic chemical evolution trends studied for 1111 FGK stars by Adibekyan et al. (2012a), possibly because of the scarcity of useful lines. From Figure A2 of Mon18, the difference is typically approximately 0.1 dex. Assuming the actual [Mn/H] values of the primaries are higher than their estimates by 0.1 dex, the departure of our results from those of Mon18 decreases. The large RMS value of the difference in abundance obtained for HD 154363B is caused by Mg and Fe, as discussed in Section 2.5.3.

Finally, we calculated the error-weighted RMS of all the differences in abundance of each element for each binary pair (i.e., 35 data) to obtain 0.20 dex. It was consistent with the typical estimated size of $\sigma_{\rm Total}$. In conclusion, assuming that the abundance measurements for GK stars are robust, our determination of the elemental abundances of early- to mid-M dwarfs is reliable within a typical precision of 0.2 dex.

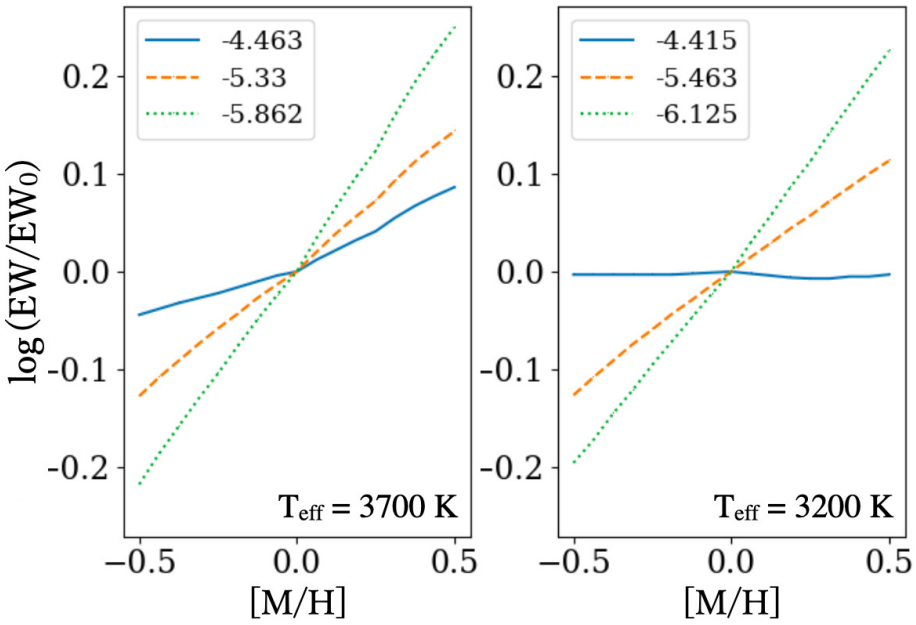

Figure 2.5: Sensitivity of the EWs of Fe I lines in model spectra to the assumed overall metallicity [M/H]. The values on the vertical axis show the logarithmic EW normalized by the value at [M/H] = 0.0 (EW_0). $T_{\rm eff}$ is assumed to be 3700 K and 3200 K for the left- and right-hand panels, respectively. $\log g$ = 4.9 and ξ = 0.5 for both panels. The blue solid line, orange dashed line, and green dotted line refer to relatively strong, medium, and weak lines, respectively. The legend in the upper-left-hand corner shows $\log(EW_0/\lambda)$, i.e., the logarithmic EW normalized by the wavelength in the case of [M/H] = 0.0.

2.5 Discussion

2.5.1 Sensitivity of line strength to abundances of elements other than the absorber

Through line selection for abundance analysis, we found that many atomic lines are not sensitive to variations in the overall metallicity, especially in the spectra of mid-M dwarfs. Figure 2.5 shows how the variation of overall metallicity assumed in the calculation alters the EWs of three Fe I lines in the model spectra as examples. It is widely recognized that stronger lines are less sensitive to absorber abundance due to the effect of saturation, as described by the so-called curve of growth. This explains the

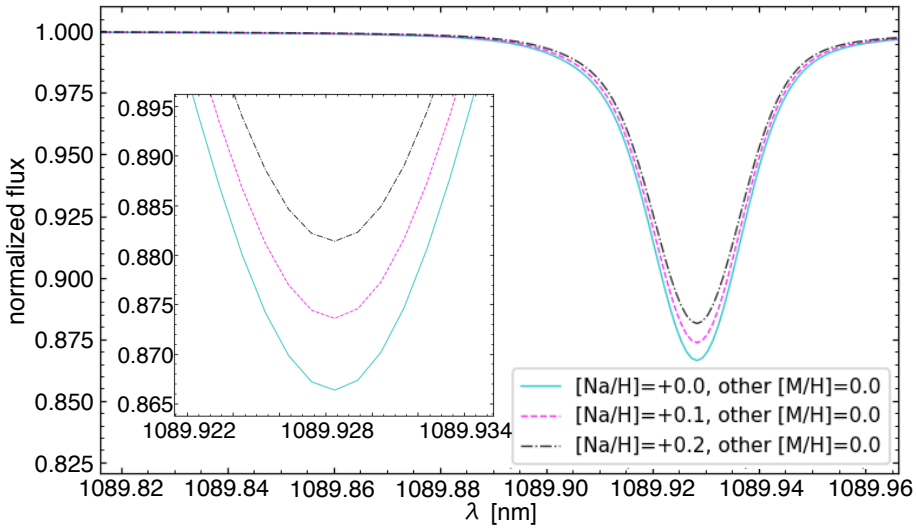

Figure 2.6: Effect of Na abundance on an Fe I line. The three spectra were calculated assuming different Na abundances and the same solar abundances of other elements, including Fe. The internal panel presents an enlarged view of the line center.

difference between the slopes of the three lines in both panels of Fig. 2.5. However, the blue solid liine in the right panel is almost flat, indicating that this strong line of mid-M dwarfs retains almost no sensitivity to the overall metallicity. This cannot be explained by the saturation alone and requires further explanation.

We found that the low sensitivity of the absorption lines to the overall metallicity is attributed to the influence of elements other than the species responsible for the absorption. For example, when higher metallicity is assumed, the higher Fe abundance strengthens the Fe I lines, but simultaneously, the higher abundances of other elements make them weaker. In particular, elements with low ionization potential (e.g., Na, Ca) cause prominent effects. The absorption profiles of an Fe I line with varying Na abundance assumed in the calculation are shown in Fig. 2.6. This demonstrates that an increase in Na abundance weakens the Fe I line. Similar effects are also found when another element is increased.

This phenomenon can be interpreted by considering the continuous absorption induced by negative hydrogen ions (H^-). The bound-free transition of H^- is the dominant opacity source at near-infrared wavelengths ($< 1.6\,\mu$m) in the atmospheres of stars similar to or cooler than the Sun. The increase in metal species, which are

more or less ionized to release electrons, increases the electron pressure, promoting the binding reaction of hydrogen and electrons. The resulting increase in H^- increases the continuous absorption coefficient κ_ν. The larger κ_ν reduces the continuum-normalized depths of absorption lines following the formula for the case of weak absorption lines (Gray 2005):

$$\frac{F_c - F_\nu}{F_c} \sim \text{constant}\, \frac{l_\nu}{\kappa_\nu}, \tag{2.5}$$

where F_ν is the flux at a certain wavelength ν inside the absorption line, F_c is the flux at wavelengths outside the absorption line, and l_ν is the line absorption coefficient at ν.

The effect of the change in abundance of a certain element on the continuous opacity depends on both its abundance and the ionization rate. Atomic species with lower ionization potential and higher abundance have larger contributions to the electron pressure. To elucidate which species dominate the effects, we solved Saha's equation of ionization to determine the contribution of each element to the electron pressure. The relative contributions of major species to the electron pressure are illustrated in Fig. 2.7. We found that Na, Ca, and Mg are the dominant electron donors in the temperature range of early- and mid-M dwarfs, with many other species also contributing to some degree.

The phenomena reported here also explain some features of the error sizes presented in Table 2.4. The $\sigma_{\rm OE}$ of an element becomes larger in mid-M than early-M dwarfs because the continuous opacity becomes more sensitive to the abundances of other elements. The small $\sigma_{\rm OE}$ of Na compared to other elements is attributed to the fact that the strength of Na I lines is relatively insensitive to the change in abundance of other elements, because Na itself is the most dominant electron source. The Na abundance controls continuous opacity to a greater extent than that of the other elements. For mid-M dwarfs, the $\sigma_{\log g}$ values are large even for elements for which the lines do not have broad wings. This is due to the sensitivity of the abundance results of Na, Mg, and Ca, which are obtained from broad lines, to the change in $\log g$. In the iterative procedure, the variations in these abundance results also induce a substantial change in the abundance results of the other elements through the change in continuous opacity.

In conclusion, we argue that it is risky to independently determine the abundance ratios of certain elements without considering the variation in the abundance of other elements. Consistent abundance ratios for each object need to be applied to the

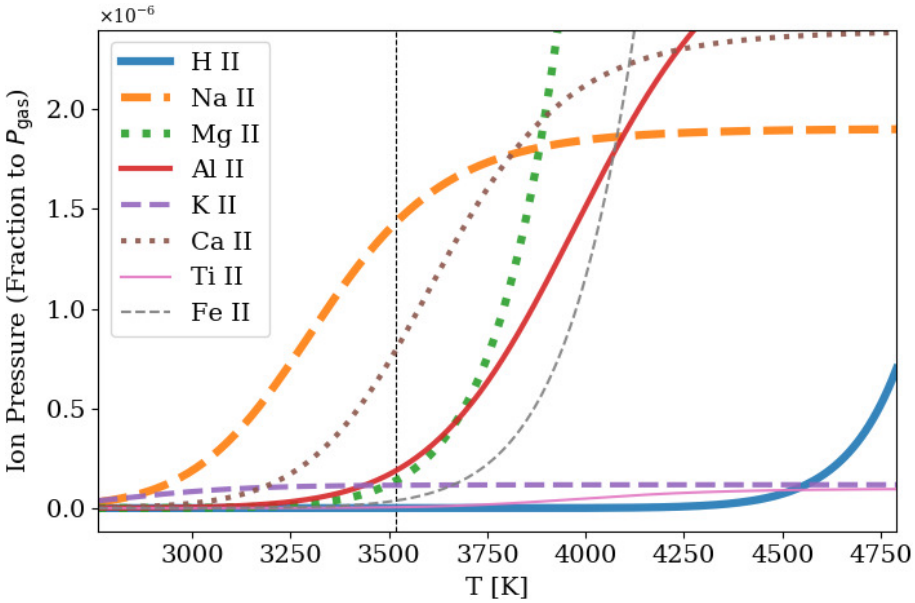

Figure 2.7: Degree of contribution of each element to the electron pressure as a function of temperature. The vertical axis shows the ratio of the partial pressure of the singly ionized species to the total gas pressure. It is calculated assuming the total gas pressure $P_{\rm gas} = 1.2 \times 10^6$ dyn cm^{-2}, and the total electron pressure $P_{\rm e} = 3.4$ dyn cm^{-2}, which are the values in the atmospheric depth with $\tau_{1200\rm nm} = 1.0$ under the condition of mid-M dwarfs with solar composition ($T_{\rm eff}$, $\log g$, ξ, [M/H]) = (3200, 5.0, 0.0, 0.0). The atmospheric temperature at that depth is indicated by the vertical dashed line ($T_{\rm eff} = 3518$ K). Note that the values on the vertical axis presented for other temperatures do not necessarily match the actual fractions at the depth of the temperatures in the stellar atmosphere because of the fixed $P_{\rm gas}$ and $P_{\rm e}$.

analysis to obtain abundance ratios and even the overall metallicity.

2.5.2 Titanium lines

It is difficult to constrain the Ti abundance despite the large number of notable Ti I lines in the near-infrared spectra of M dwarfs. The Ti I lines show little response to the overall metallicity in the spectra of early-M dwarfs. A negative correlation even appears between the Ti I line strengths and the overall metallicity at $T_{\rm eff} < 3400$ K. This is a unique behavior found only for the absorption lines of Ti among all the elemental lines used.

This is attributed to the abundance changes of elements other than Ti. We investigated the response of the Ti I lines in the model spectra separately to the abundances of Ti and of all the other elements, as shown in the upper three panels in Fig. 2.8. The left-hand panel shows the natural behavior of Ti I lines getting stronger as the Ti abundance increases. The weaker lines show higher sensitivity to Ti abundance, as expected from a curve of growth. The middle panel, in contrast, shows that the increase in the other elemental abundances weakens the Ti I lines. This relation does not have a significant dependence on individual absorption lines. The negative slope shown here is steeper than the positive slope of the left-hand panel. As a result of both effects, the EWs of the Ti I lines gradually decrease as the overall metallicity increases, as shown in the right-hand panel.

The same plots for Fe are shown for comparison in the lower panels of Fig. 2.8. The value of "slope'' hereafter is simply calculated as the change of the log (EW) corresponding to the change of [X/H] from −0.5 to +0.5. The slopes in the upper left-hand panel of Fig. 2.8 for Ti range from 0.45 to 0.78, which are not appreciably different from the slopes in the lower left-hand panel for Fe. In contrast, the slopes of the plots in the upper middle panel range from −0.82 to −0.68, which are significantly steeper than any plots of the other elements, including those for Fe in the lower middle panel. Hence, the unique behavior found for Ti I lines is not due to the sensitivity of the line strengths to [Ti/H], but rather the abundances of other elements.

We found that the Ti I line strengths have a negative correlation with the oxygen abundances assumed in the calculation. Figure 2.9 shows the modeled EWs of the Ti I lines as functions of [O/H] and [O, C/H]. The EWs sharply decrease with the

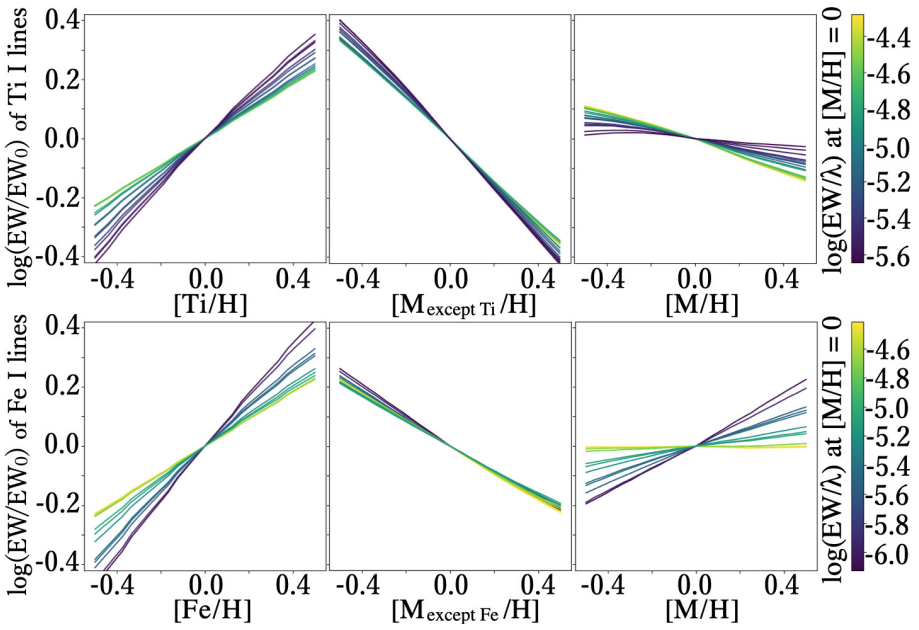

Figure 2.8: Upper panels show the sensitivity of the EWs of all Ti I lines used in the analysis to the Ti abundance in the left-hand panel, to the abundances of all elements except for Ti in the center panel, and to the overall metallicity including Ti in the right-hand panel. The vertical axis is the same as that in Fig. 2.5. All the spectra were calculated with $T_{\rm eff}$ = 3200 K, $\log g$ = 4.9, and ξ = 0.5 km s^{-1}. The color bar indicates $\log({\rm EW}_0/\lambda)$, i.e., the logarithmic EW at [M/H] = 0.0, normalized by the wavelength. The lower three panels are the same plots as in the upper panels but for Fe instead of Ti.

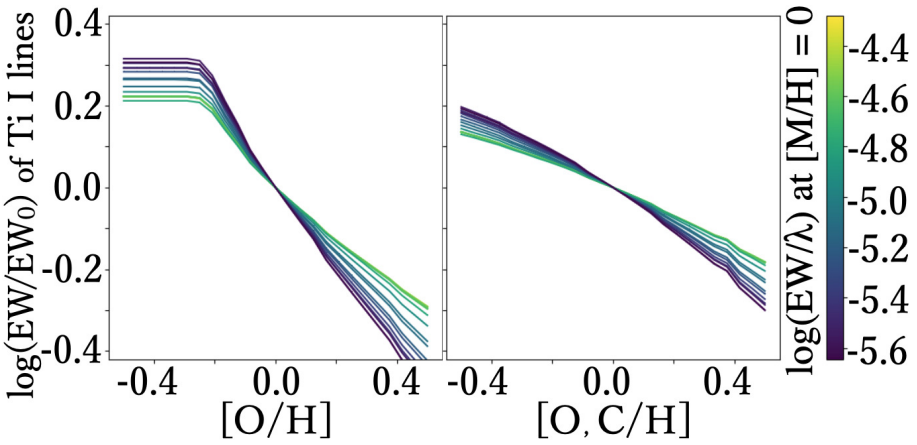

Figure 2.9: Same plots as in the upper left-hand panel of Fig. 2.8, but for oxygen abundance [O/H] in the left-hand panel, and for oxygen and carbon abundance [O, C/H] in the right-hand panel.

increase in oxygen. This is due to the decrease in neutral titanium (Ti I) as a result of the formation of titanium oxide molecules (TiO) in M dwarfs. Note that the flat part appearing at [O/H] ≤ -0.25 dex in the left-hand panel is due to the depletion of oxygen available to form TiO. The oxygen below this level is mainly combined with carbon to form CO; thus, the flat part is not seen if [C/H] also changes together with [O/H], as shown in the right-hand panel. The sensitivity of Ti I lines to O and C abundances assumed in the analysis explains the particularly steep slopes for the Ti I lines in the upper middle panel of Fig. 2.8. We note that the influence of the variation in [O, C/H] on the strength of any other atomic lines used is negligible.

For a complete understanding of the peculiar behavior of Ti I lines, we also examined the influence of additional possible factors other than elemental abundances. Firstly, we investigated the response of Ti I lines to temperature. Although the sensitivity of EW to $T_{\rm eff}$ differs from line to line depending on the $E_{\rm low}$ of the transition and the line strength, the variation in EW corresponding to a 100 K change in $T_{\rm eff}$ is at most 0.025 dex. When the overall metallicity varies by 0.1 dex, the temperature of the atmospheric layer with $\tau \sim 1$ changes by 100 K because of the so-called line-blanketing effect, which can induce a 0.025 dex change in the EW of Ti I lines in an extreme case. However, this variation is substantially smaller than the variation in Ti I lines due to changes in the oxygen abundances.

Secondly, we examined the influence of the nature of the absorption lines, i.e., the gf-value, $E_{\rm low}$, or EW. To disentangle their separate effects and dependence on elemental species, we probed the behavior of three artificial lines of Cr, the ionization energy (6.764 eV) of which is close to that of Ti (6.820 eV). We set up the parameters of each artificial line, namely the gf-value, $E_{\rm low}$, and EW, such that two were identical to those of the actual Ti I line at 967.8197 nm. As a result, the sensitivity of all the artificial Cr I lines to the variation in abundance of the other elements was shown to be similar to that of the actual Cr I lines, and less than that of the Ti I lines. This indicates that the unique behavior of Ti I lines is not due to any specific nature of the spectral lines.

We conclude that the dominant cause of the unique response of Ti I lines to changes in the overall metallicity is the consumption of neutral Ti atoms by the formation of TiO molecules. This behavior was briefly argued by Mould (1976), who found a similar negative metallicity dependence of Ti I lines in the I-band spectra of mid-M dwarfs and mentioned the effect of TiO formation. Tsuji (1973) demonstrated the partial pressure of each species harboring Ti in stellar atmospheres at different $T_{\rm eff}$, as shown in Fig. 3 of the paper. The abundance of TiO exceeds that of neutral Ti at temperatures less than approximately 2800 K, while Ti^+ ions dominate over neutral Ti at temperatures higher than approximately 3200 K. Because the atmospheric temperature of M dwarfs corresponds to the temperature range in which these transitions occur, the changes in the ionization state of Ti complicate the interpretation of the Ti I lines. Similar transitions are not seen for the other elements analyzed in this study, whereas silicon and zirconium show similar behavior, forming SiO and ZrO at $T < 3000$ K. Special care is required for the analysis of Si I or Zr I lines.

Several previous studies used Ti I lines to estimate the [M/H] or [Fe/H] of M dwarfs (e.g., Passegger et al. 2019, Rajpurohit et al. 2018a, Lindgren et al. 2016). However, the unique behavior of the lines has not been fully discussed. Here, we urge caution in using the Ti I lines as the indicator of [M/H], because the increases in Ti and in the other elements have opposite effects on the strength of the lines. When we derive [Ti/H], we need to analyze the Ti I lines with reliable abundances of other elements, especially O, C, Na, and Ca. Veyette et al. (2017) and Veyette & Muirhead (2018) also used the Ti I lines as indicators of the Ti abundance and the stellar age. The negative correlation between the Fe abundances and EWs of Ti I lines can be seen in some EW pairs measured and tabulated by Veyette et al. (2017). However, they did not

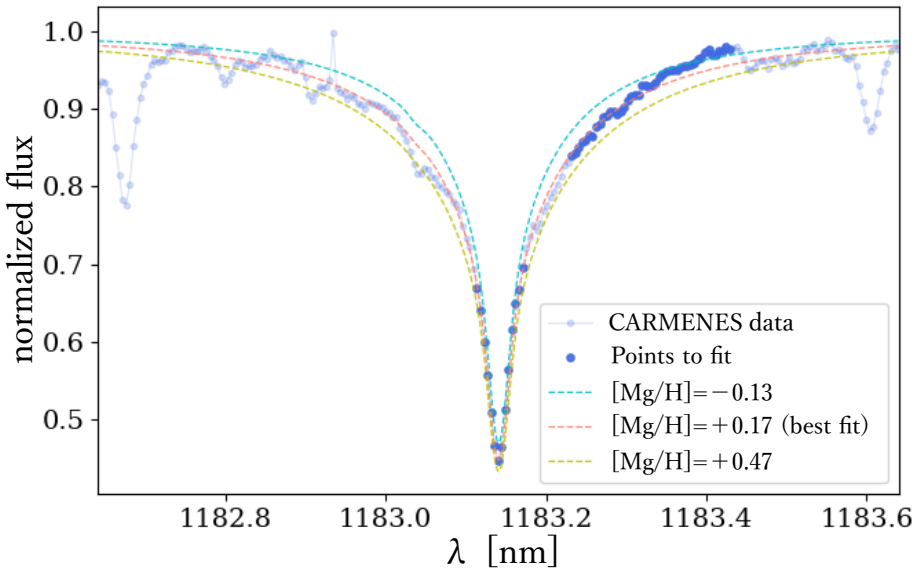

Figure 2.10: Mg I line in the observed spectra of HD 154363B (blue dots; the deep dots are used for fitting and the pale dots are not used) and synthetic model spectra calculated with the best-fit Mg abundance [Mg/H] = 0.13 dex, and with 0.3 dex higher and lower abundances (dashed lines).

estimate the impact of other elements, such as O and Na, which could cause potential uncertainty in their estimates.

2.5.3 HD 154363B

Here, we discuss the noticeable discrepancy in the Fe and Mg abundances between HD 154363B and its primary HD 154363A, as seen in Fig. 2.4. Our abundances of HD 154363B ([Fe/H] = −0.34 ± 0.15; [Mg/H] = 0.17 ± 0.27) deviates from the error range of those of the primary ([Fe/H] = −0.62 ± 0.05; [Mg/H] = −0.53 ± 0.16).

The Mg I line used is relatively deep and broad (EW ∼ 107 pm) with wide damping wings. To examine the effect of possible imperfection of the Voigt profile fitting, we conducted a chi-square fitting between the observed line profile and synthetic spectra (Fig. 2.10). As a result, we derived almost the same abundance result as the EW analysis, confirming that the [Mg/H] of this M dwarf is higher than the value obtained by Mon18 for the primary star.

The overall metallicity of HD 154363B has been studied based on empirical

calibration methods. Gaidos et al. (2014) derived [Fe/H] = −0.39 ± 0.11 from the medium-resolution ($R \sim 1300$) visible spectra. Newton et al. (2014) obtained [Fe/H] = −0.44 ± 0.14 from the medium-resolution ($R \sim 2000$) near-infrared spectra. Both are consistent with our Fe abundance of HD 154363B rather than that of its primary as reported by Mon18.

Lastly, our results with low [Fe/H] and enhanced [Mg/Fe] (0.51 ± 0.31) follow the abundance trends in the thick disk of the Milky Way Galaxy (e.g., Bensby et al. 2014). Although the reason for the discrepancy between our result for HD154363B and that of Mon18 for the primary star is not clear, we regard our abundance results for this M dwarf as reliable from the above inspection.

2.6 Summary

We analyzed the high-resolution near-infrared CARMENES spectra of five M dwarfs belonging to binary systems with G or K dwarfs to determine their abundances of seven to eight individual elements. We verified our determination by comparing our abundances of M dwarfs with those of the primary stars derived by Montes et al. (2018) from high-resolution visible spectra. The results show good agreement, typically within 0.2 dex, without significant systematics.

We calculated the expected precision of the result for each element of each object from the quadrature sum of the errors arising from six different sources to be typically 0.1–0.3 dex. We also investigated the contribution of individual sources to the total error. The dominant error source depends on the elemental species and the stellar temperature.

A notable difference from the standard analysis for FGK stars is the large errors propagated from the uncertainties of $\log g$ and the abundances of elements other than the corresponding species. The derived abundances have high sensitivity to $\log g$ because many lines used in the analysis are affected by pressure broadening under the high $\log g$ of M dwarfs. The abundance results are also affected by the variation of the continuous opacity by H^-, which depends on the abundances of metals especially with low ionization potential, such as Na and Ca. In addition, the strength of Ti I lines in the near-infrared spectra of M dwarfs with $T_{\rm eff} < 3400$ K shows an anti-correlation with the overall metallicity because the increase in oxygen promotes the consumption of

neutral Ti by the formation of TiO molecules.

These results indicate that to constrain the true abundance of any element or even the overall metallicity, it is crucial to determine the consistent abundance ratios of individual elements in the chemical analysis of each M dwarf.

The application of our chemical analysis to the M dwarfs observed by the planet search projects will provide reliable and consistent abundance ratios on a larger sample of nearby M dwarfs than ever before. This information will be useful for the observational understanding of how the occurrence rate and characteristics of planets depend on the elemental abundances of the host M dwarfs.

2.7 Chapter Appendix: Exclusion of BD-02 2198

Table 2.6: Basic information of BD-02 2198 (same format as Table 2.1)

Name	R.A.	Decl.	SpT	$T_{\rm eff}$	$\log g$	Name of	SpT of	[Fe/H] of	S/N
	J2000.0			(K)		Primary	Primary	Primary	(1000 nm)
BD-02 2198	07:36:07.08	−03:06:38.8	M1.0V	3744±82	4.76±0.24	HD 61606 A, B	K3V, K7V	−0.11±0.03	187

Table 2.7: Abundance results and errors (same format as Table 2.4)

Object	Element	[X/H]	$N_{\rm line}$	$\sigma_{\rm SEM}$	$\sigma_{T_{\rm eff}}$	$\sigma_{\log g}$	σ_{ξ}	$\sigma_{\rm OE}$	$\sigma_{\rm cont}$	$\sigma_{\rm Total}$
BD-02 2198	Na	−0.04	2	0.08	0.01	0.01	0.00	0.02	0.05	0.10
	Mg	0.29	1	0.12	0.09	0.05	0.02	0.09	0.05	0.19
	K	0.44	2	0.08	0.02	0.08	0.01	0.06	0.03	0.14
	Ca	0.32	6	0.07	0.01	0.04	0.01	0.05	0.03	0.10
	Ti	0.48	10	0.04	0.05	0.03	0.03	0.15	0.02	0.17
	Cr	0.42	3	0.07	0.05	0.01	0.03	0.08	0.05	0.13
	Mn	0.17	1	0.12	0.05	0.02	0.02	0.10	0.05	0.18
	Fe	0.28	5	0.05	0.05	0.02	0.03	0.08	0.05	0.13

In addition to the sample given in Table 1, we analyzed the spectra of another early-M dwarf, BD-02 2198, obtained from the CARMENES GTO Data Archive. The basic information and abundance results are presented in Tables A1 and A2, respectively. However, we excluded it from our targets in this chapter, based on the kinematic information.

Poveda et al. (2009) reported that this star is a member of a triplet with HD 61606 A and B based on their proper motions, parallaxes, radial velocities, and ages estimated

by the X-ray luminosity. However, they also reported that the difference in their proper motions is larger than the error, and suggested the possibility of dynamical disintegration. We used the latest astrometric data from *Gaia* DR2 (Gaia Collaboration et al. 2018) to compare the escape velocity and actual three-dimensional relative velocity of BD-02 2198 with respect to the barycenter of the HD 61606 AB system. Here, we treated the two K dwarfs as one mass point for simplicity because their distance from BD-02 2198 is almost an order of magnitude larger than the distance between them. The mass of HD 61606 A ($0.82 \pm 0.03\ M_{\odot}$) is sourced from Luck (2017) and those of HD61606B ($0.66 \pm 0.07\ M_{\odot}$) and BD-02 2198 ($0.54 \pm 0.07\ M_{\odot}$) are sourced from Gaidos et al. (2014). The escape velocity of BD-02 2198 from HD 61606 AB is

$$v_{\mathrm{escape}} = \sqrt{\frac{2\mathrm{G}(M+m)}{r}}, \tag{2.6}$$

where G is the gravitational constant, M is the total mass of HD 61606 AB, m is the mass of BD-02 2198, and r is the distance of BD-02 2198 from the barycenter of HD 61606 AB. The result is 0.25 ± 0.01 km s^{-1}. The relative velocity of BD-02 2198 to HD 61606 AB estimated from their proper motions and radial velocities is 1.58 ± 0.43 km s^{-1}, which exceeds the escape velocity by more than 3σ. This confirms that BD-02 2198 is not gravitationally bound by HD 61606 AB.

The results of our abundance analysis on BD-02 2198 show an offset greater than the error margin of the abundances of HD 61606 A reported by Mon18, as seen in Fig. 2.11. We attributed the discrepancy not to the systematic overestimation of our analysis but to the different origins of these objects. Based on the above investigation, we concluded that BD-02 2198 and HD 61606 AB are not members of the same multiple system sharing a common origin, and thus excluded them from the binary comparison in Section 2.4.2.

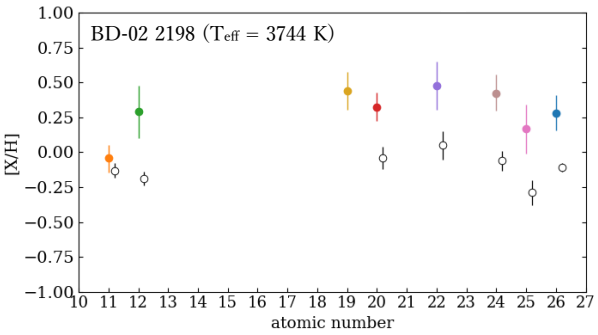

Figure 2.11: Abundances of individual elements we determined for BD-02 2198 (color-filled circles), and those for HD 61606 A determined by Montes et al. (2018) (black open circles). The axes are the same as in Fig. 2.4.

3

Chemical analysis of IRD planet survey

3.1 Overview

Aiming to statistically understand the chemical properties of nearby M dwarfs, which are the primary targets of planet search projects and the most numerous constituents of the Galaxy, we present the abundance analysis for 13 M dwarfs from the targets of the IRD-SSP project as a pilot sample.

The InfraRed Doppler instrument (IRD; Kotani et al. 2018) is a fiber-fed echelle high-resolution near-infrared spectrometer mounted on the Subaru Telescope. It covers the Y-, J-, and H-bands (970–1750 nm) simultaneously with a maximum spectral resolution of ~70,000 and has a laser frequency comb (LFC) for the precise wavelength calibration, which allows radial velocity (RV) measurements with a precision better than 2 m s^{-1}. The main purpose of the instrument is the planet search around nearby mid-M to late-M dwarfs (spectral type later than M4V). Late-M dwarfs are advantageous for the RV detection of the Earth-mass planets (~1–3 $M_\oplus$) in the habitable zone because the large RV signals (~1–5 m s^{-1}) are expected from their low stellar masses (~0.1–0.2

$M_\odot$) and short planetary orbital periods (~3–30 days). The large diameter (8.2 m) of the Subaru Telescope and the wide coverage of the IRD over the near-infrared wavelength where the flux peak of M dwarfs locates enable the systematic survey of fainter, thus late-type, M dwarfs than ever before. The survey project is running since February 2019 in the framework of the Subaru Strategic Program (IRD-SSP).

The high-S/N spectra obtained in the IRD-SSP are the suitable and favorable data set to investigate elemental abundances of nearby M dwarfs. This allows us to grasp the distribution of stellar elemental abundances in the solar vicinity because M dwarfs account for more than 70 % of the nearby stars. Besides, the knowledge of elemental abundances of the IRD-SSP targets will be needed to discuss the characteristics of planets that will be detected on the project.

In this chapter, we determine the chemical composition of 13 M dwarfs observed in the IRD-SSP by the analysis method verified in Chapter 2. In Section 3.2, we introduce our targets and the target selection of IRD-SSP. We describe the analysis on the effective temperatures, elemental abundances, and kinematics of our targets in Section 3.3, and their results in Section 3.4. Based on the results, we discuss the location of our M dwarfs in the Galactic context and its indication to the planet searches in Section 3.5. We summarize the chapter in Section 3.6.

3.2 Targets and data

The same objects are observed in multiple epochs during a five-year survey period of IRD-SSP in order to precisely investigate the RV variations. We used the IRD stellar template spectrum made for each object as a reference for the relative RV on each day (Hirano et al., 2020).

The template spectra are generated by deconvolving from instrumental broadening profiles (IP), removing telluric absorptions, and combining the multiple frames. IRD has another fiber in addition to the one that carries the starlight, to simultaneously observe the wavelength calibration sources generated with an LFC. The IP is derived for each frame and each spectral segment, with a width of ~1 nm, based on the simultaneously observed spectra of LFC. The removal of telluric lines is conducted by fitting the theoretical telluric spectra synthesized with Line-By-Line Radiative Transfer Model (Clough et al., 1992, 2005). The imperfection of the synthesis might leave some telluric

Table 3.1: Basic information of the target M dwarfs

Name	R.A.	Decl.	V_{mag}	J_{mag}	K_{mag}	T_{eff} (K)	log g	Luminosity ($L_\odot$)
GJ 436	11:42:11.09	+26:42:23.7	10.7	6.90	6.07	3456±157	4.804±0.005	0.0233±0.0056
GJ 699	17:57:48.50	+04:41:36.1	9.5	5.24	4.52	3259±157	5.076±0.028	0.0038±0.0010
LSPM J1306+3050	13:06:50.25	+30:50:54.9	15.5	10.23	9.31	2970±157	5.127±0.037	0.0020±0.0005
LSPM J1523+1727	15:23:51.13	+17:27:57.0	14.2	9.11	8.28	3151±157	5.050±0.023	0.0038±0.0010
LSPM J1652+6304	16:52:49.46	+63:04:38.9	14.4	9.59	8.76	3115±157	5.024±0.019	0.0043±0.0011
LSPM J1703+5124	17:03:23.85	+51:24:21.9	13.6	8.77	7.92	3103±157	5.037±0.021	0.0039±0.0010
LSPM J1802+3731	18:02:46.25	+37:31:04.9	15.3	9.72	8.89	2992±157	5.110±0.034	0.0022±0.0006
LSPM J1816+0452	18:16:31.54	+04:52:45.6	15.0	9.80	8.83	3072±157	5.045±0.022	0.0036±0.0009
LSPM J1909+1740	19:09:50.98	+17:40:07.5	13.6	8.82	7.90	3125±157	5.024±0.019	0.0043±0.0011
LSPM J2026+5834	20:26:05.29	+58:34:22.5	14.0	9.03	8.10	3025±157	5.072±0.027	0.0029±0.0008
LSPM J2043+0445	20:43:23.88	+04:45:55.3	15.4	10.08	9.14	2979±157	5.073±0.027	0.0027±0.0007
LSPM J2053+1037	20:53:33.04	+10:37:02.0	13.9	9.35	8.48	3168±157	5.037±0.021	0.0042±0.0011
LSPM J2343+3632	23:43:06.29	+36:32:13.2	12.5	8.11	7.23	3175±157	4.993±0.015	0.0055±0.0014

The stellar parameters are adopted from the TESS Input Catalog (TIC) Version 8.

features. They can be mostly removed by taking the median of the spectra obtained over seasons because the telluric features move against the intrinsic stellar spectra due to the barycentric motion of the Earth.

To ensure the quality of the template spectra of the pilot sample, we selected 13 M dwarfs which were already observed with IRD more than eight times on well-separated nights. Not only the survey targets but also 2 objects observed as RV standards, GJ 436 and GJ 699, are included. Table 3.1 shows the basic information of the targets.

To grasp the underlying property of our sample, we here mention the target selection of the IRD-SSP. It is planned to monitor 60 carefully selected M dwarfs taking 175 observing nights over the five years duration of the project. By the start of the project, 150 objects have been selected in the IRD input catalog. This selection is based on the following six criteria to guarantee the accuracy and efficiency of the RV measurements: (1) J-band magnitudes $J_{mag} < 11.5$, (2) stellar mass $M_\star < 0.25$ $M_\odot$ ($T_{eff} <$ ~3400 K), (3) rotational velocities $v \sin i < 5$ km s^{-1}, (4) no significant Hα emission (EW$_{H\alpha} < -0.75$ Å), (5) rotational periods $P_{rot} > 70$ days, and (6) expected to be a single star. The information of stellar properties used in the criteria is collected from the literature and the pre-selection observations with medium-resolution optical spectroscopy. Figure 3.1 shows the histogram of EW of Hα measured for IRD targets (Sato et al., 2018), where the active stars are screened out by the criterion (4), compared with that of CARMENES targets (Reiners et al., 2018).

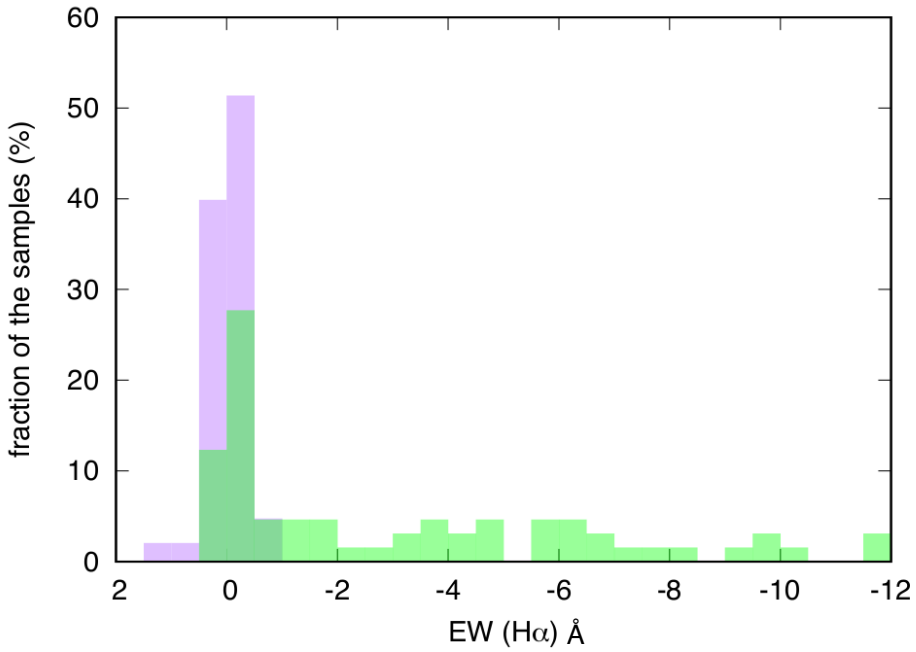

Figure 3.1: Histograms of target fractions (%) for EW of Hα (656.28 nm) in Å. Negative EW values (to the right) indicate an emission, which indicate the objects are relatively active. The IRD-SSP sample (purple) includes only quiet M dwarfs, while the CARMENES GTO sample shows a variety of activity levels. The figure was adapted from the IRD-SSP proposal (Sato et al., 2018).

Thereby, we do not consider the influence of the magnetic field and activity on the analysis in this chapter. It should be noted, however, that almost half or more objects in the volume-limited sample of mid-M to late-M dwarfs are magnetically active (e.g., Jeffers et al., 2018), so we should be aware of a potential selection bias this selection may impose on our results.

3.3 Analysis

We determined the abundances of individual elements for the 13 targets by the analysis method presented in Section 2.3. An overview is given below. We measured EW of an absorption line of interest from the normalized one-dimensional spectra and compared it with EW from synthetic spectra calculated with the radiative transfer code, iteratively modifying the abundance of the responsible element assumed in the calculation until both EWs agree. The radiative transfer is calculated assuming the plane-parallel stratification in homogenous layers, LTE, and hydrostatic, radiative, and chemical equilibrium. The atmospheric layer structure is derived from the interpolated grid of MARCS and the spectral line data are taken from VALD. The dust formation is not considered as dust opacity is still negligible in atmospheres with $T_{\rm eff} > 2800$ K. For each element X, the abundance ratio [X/H] was determined by averaging the results from all absorption lines. Although abundances other than the element of interest were assumed to be solar values in the previous step, in the next step, the abundance results of the previous step are adopted to perform the same analysis. This is iterated until the difference between the assumed value and the result converges to ±0.005 for all elements consistently. We estimated the error $\sigma_{\rm Total}$ by taking the quadrature sum of (1) random scatter between the results from individual lines ($\sigma_{\rm SEM}$), (2) propagated errors from stellar parameters ($\sigma_{T_{\rm eff}}$, $\sigma_{\log g}$, and σ_{ξ}), (3) propagated errors from abundances of all elements except for the one of interest ($\sigma_{\rm OE}$), and (4) propagated errors from the uncertainty of continuum levels ($\sigma_{\rm cont}$).

There are two modifications in the analysis procedure from that in Section 2.3. First, We adopted $T_{\rm eff}$ and $\log g$ values from TESS Input Catalog (TIC) Version 8 (Stassun et al., 2019). The second is the EW measurement procedure. Besides, we also investigate the kinematics of the targets. The details are described in the following subsections.

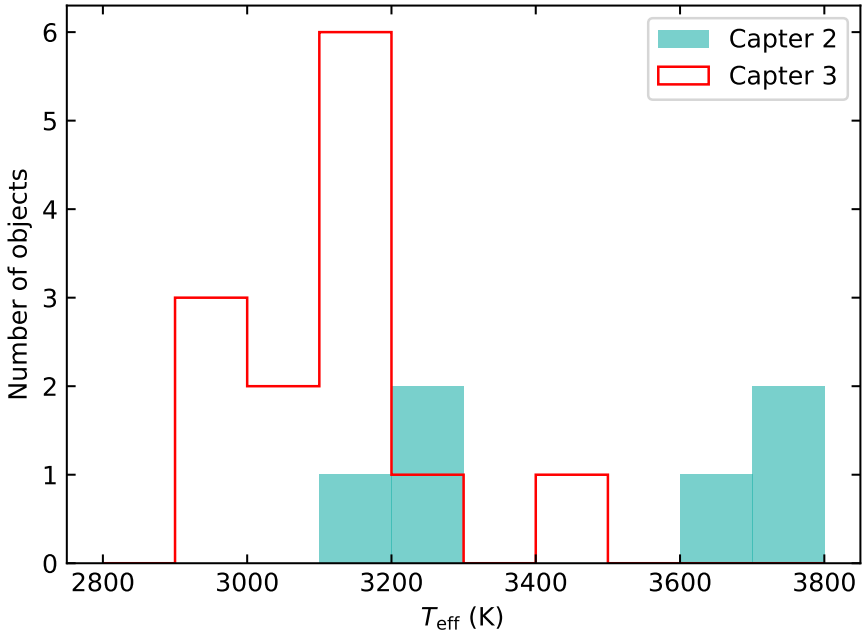

Figure 3.2: The distribution of $T_{\rm eff}$ from TIC of our targets. The green and red histograms show the samples analyzed in Chapter 2 and this chapter, respectively.

3.3.1 Stellar parameters

In the previous chapter, we referred for $T_{\rm eff}$ and $\log g$ to several previous studies as described in Section 2.3.1. In contrast, here we adopted the $T_{\rm eff}$ and $\log g$ stored in the TIC Version 8 for homogeneity in all the targets.

The $T_{\rm eff}$ of M dwarfs in TIC ($T_{\rm eff\text{-}TIC}$) is based on the empirical relation between the $T_{\rm eff}$ and the $G_{\rm BP} - G_{\rm RP}$ color from the Gaia photometry. The empirical relation was calibrated by the sample of Mann et al. (2015, Man15) and their $T_{\rm eff}$ estimates. The typical uncertainty, which is dominated by the fitting scatter, is 157 K. Figure 3.2 shows the adopted $T_{\rm eff\text{-}TIC}$ distribution of the targets comparing with the verification sample analyzed in the previous chapter. The sample of this study includes objects with 100–200 K lower temperatures than those of the sample in Chapter 2. In this temperature range, dust formation in atmospheres is not expected, and, hence, this difference would not have a large impact on the modeling of the atmospheric structure. Examination of the reliability of the abundance analysis for M dwarfs with such

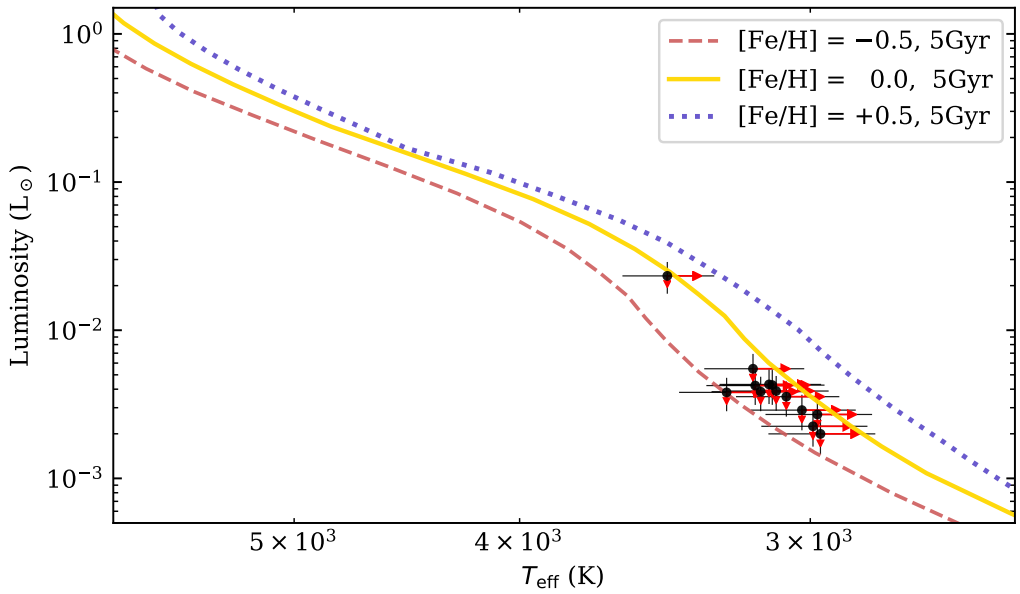

Figure 3.3: HR diagram, i.e., the Luminosity–$T_{\rm eff}$ relations, for the 13 target M dwarfs superimposed on the 5-Gyr theoretical models for [Fe/H] = −0.5, 0.0, +0.5 from the PARSEC library. The black dots and error bars represent the temperature and luminosity recorded in TIC for the 13 objects. The red arrows show the change when the $T_{\rm eff}$ is adjusted downward by 100 K.

temperatures in binary systems is desired in future work. Once the $T_{\rm eff}$ becomes lower than about 2800 K, dust formation may start to affect the spectra (e.g. Tsuji et al., 1996). The Hertzsprung–Russell (HR) diagram of the targets is presented in Figure 3.3 with predictions from the PARSEC stellar evolutionary models version 2.1 (Bressan et al., 2012; Chen et al., 2014) at an age of 5 Gyr for different metallicities. It shows that our target sample covers the mid-M to late-M dwarf stars. All the targets are located between two models of [Fe/H] = 0.0 and −0.5. This might be suggesting that they are all metal-poor or that the $T_{\rm eff\text{-}TIC}$ are systematically overestimated. For example, when the $T_{\rm eff\text{-}TIC}$ is adjusted downward by 100K, the black dots in the HR diagram move according to the direction and length of the red arrows. Note that the luminosity in TIC is calculated by the Stefan-Boltzmann law from the $T_{\rm eff\text{-}TIC}$ and radius estimated from the radius-M_K relation in Man15, thus a downward adjustment of $T_{\rm eff\text{-}TIC}$ also reduces the luminosities.

The $\log g$ in TIC is calculated from the mass and radius, which are estimated from the mass-M_K relation in Mann et al. (2019) and the radius-M_K relation in Man15, respectively. The typical error in the mass-M_K relation is reported to be 2–3 % and that in the radius-M_K relation is 3–4 %. They result in the $\log g$ error of ~0.02–0.03 dex.

The ξ is fixed to 0.5 km s^{-1} for all objects and consider its error of ±0.5 km s^{-1} as same as in Section 2.3.1. All the adopted stellar parameters are tabulated in Table 3.1.

3.3.2 Effective temperature from FeH lines

We also investigated the possibility to determine $T_{\rm eff}$ using FeH molecular lines, which are very sensitive to temperature. Our approach is to find $T_{\rm eff}$ at which the synthetic spectra best reproduce the strengths of FeH lines. An advantage of this approach is that the $T_{\rm eff}$ can be homogeneously determined by the same technique for all the IRD samples, which is suitable for comparing the abundances between individual objects.

The so-called Wing-Ford band of FeH lines at ~990–1020 nm (Wing & Ford, 1969) is one of the most prominent molecular features observed in the near-infrared spectra of M dwarfs. We selected 57 well-isolated FeH lines in the band to measure EW as indicators of the $T_{\rm eff}$. The selected line list is provided in Table 3.2. Since there is no information on the van der Waals damping parameters for these lines, we calculated the pressure broadening by applying the hydrogenic approximation of Unsöld (1955).

Table 3.2: FeH molecular line list

Species	λ (nm)*	$E_{\rm low}$ (eV)†	$\log gf$‡
FeH	990.0494	0.225	-0.663
FeH	990.4994	0.134	-0.770
FeH	990.5874	0.177	-0.712
FeH	990.7749	0.201	-0.686
FeH	991.2003	0.153	-0.791
FeH	991.4707	0.086	-0.954
FeH	991.6444	0.061	-1.075
FeH	992.4867	0.084	-1.111
FeH	992.8899	0.137	-0.891
FeH	993.3278	0.176	-0.760

Table 3.2 (Continued)

Species	λ (nm)*	$E_{\rm low}$ (eV)†	$\log gf$‡
FeH	993.5211	0.056	-1.695
FeH	993.5984	0.066	-0.928
FeH	994.1595	0.199	-0.732
FeH	994.2386	0.343	-0.584
FeH	994.4552	0.139	-0.891
FeH	994.5821	0.173	-0.816
FeH	994.7144	0.053	-0.983
FeH	995.0860	0.407	-0.552
FeH	995.3069	0.156	-0.852
FeH	995.6651	0.376	-0.568
FeH	995.7322	0.194	-0.783
FeH	996.2875	0.175	-0.816
FeH	996.5181	0.442	-0.537
FeH	997.0824	0.216	-0.754
FeH	997.3036	0.410	-0.552
FeH	997.3811	0.196	-0.783
FeH	997.4490	0.108	-1.162
FeH	999.4835	0.051	-1.588
FeH	1000.3446	0.266	-0.700
FeH	1000.7714	0.073	-1.724
FeH	1001.0072	0.334	-0.617
FeH	1001.0404	0.177	-0.883
FeH	1001.9538	0.066	-1.446
FeH	1003.3067	0.427	-0.565
FeH	1003.6239	0.089	-1.775
FeH	1003.9977	0.043	-1.407
FeH	1004.3975	0.322	-0.654
FeH	1005.2318	0.066	-1.544
FeH	1005.5334	0.097	-1.640
FeH	1005.7509	0.239	-0.778

Table 3.2 (Continued)

Species	λ (nm)*	$E_{\rm low}$ (eV)†	$\log gf$‡
FeH	1005.8284	0.051	-1.262
FeH	1006.1634	0.115	-1.684
FeH	1006.5967	0.084	-1.198
FeH	1007.1895	0.262	-0.749
FeH	1008.8971	0.602	-0.488
FeH	1009.4644	0.073	-1.080
FeH	1009.5954	0.288	-0.722
FeH	1009.9352	0.468	-0.550
FeH	1009.9628	0.108	-1.254
FeH	1010.7984	0.106	-1.050
FeH	1011.0859	0.538	-0.523
FeH	1011.5008	0.086	-1.015
FeH	1011.5689	1.043	-0.633
FeH	1011.7964	0.315	-0.697
FeH	1011.9702	0.416	-0.597
FeH	1012.0335	0.108	-1.050
FeH	1013.5384	0.121	-0.993

* Wavelength in vacuum † Lower excitation potential

‡ Oscillator strength

Synthetic spectra based on the line list by Plez reproduce the individual lines in the band well. We confirmed the FeH lines are exclusively sensitive to $T_{\rm eff}$ rather than [Fe/H] or $\log g$. Figure 3.4 shows the EW of FeH lines calculated using model atmospheres normalized to those for $T_{\rm eff}$ = 3000K as a function of $T_{\rm eff}$. The figure demonstrates that the EWs of the FeH lines are sensitive to temperature, though the sensitivity is generally dependent on the line strengths mainly due to saturation effect. A hundred degree change in the assumed $T_{\rm eff}$ changes the EWs by ~0.1 dex. In contrast, the variation in the EWs along with the change in the overall metallicity [M/H] of 0.1 dex is less than 0.01 dex. The change in $\log g$ of 0.1 dex also does not affect the EWs by more than 0.05 dex.

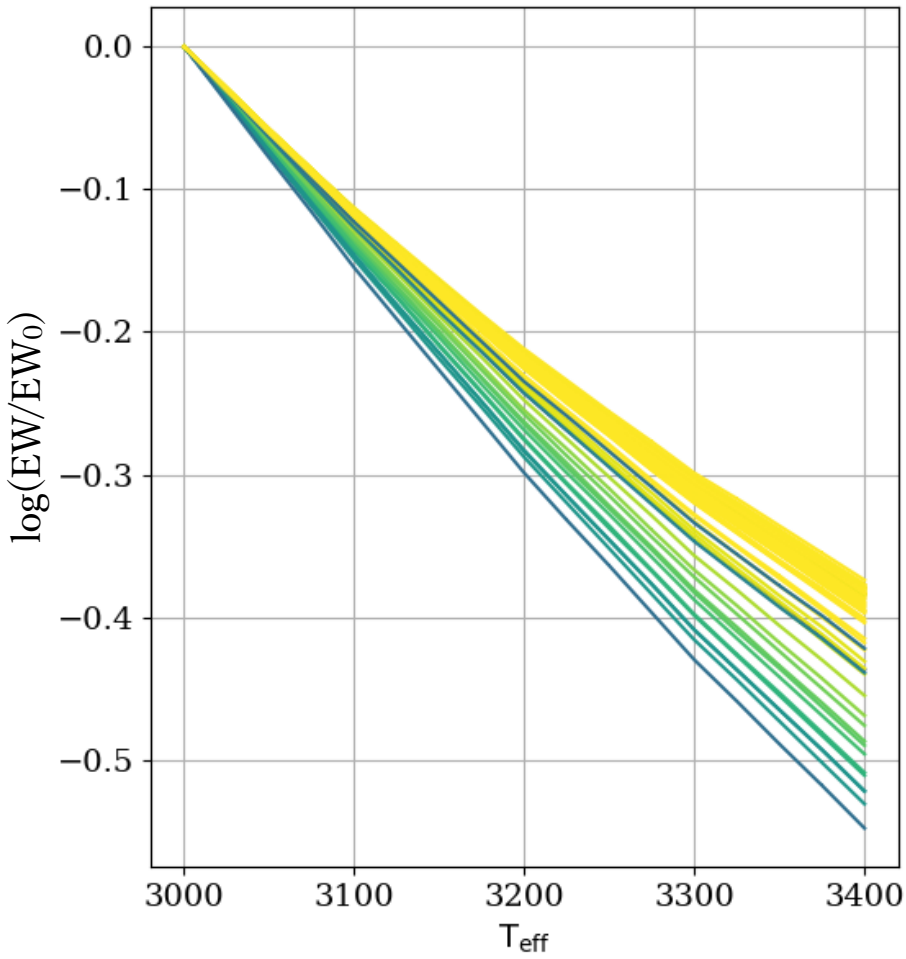

Figure 3.4: Sensitivity of EWs of the selected FeH lines in model spectra to the assumed $T_{\rm eff}$. The vertical axis shows the logarithmic EW normalized by the value at $T_{\rm eff}$ = 3000 K (EW_0).

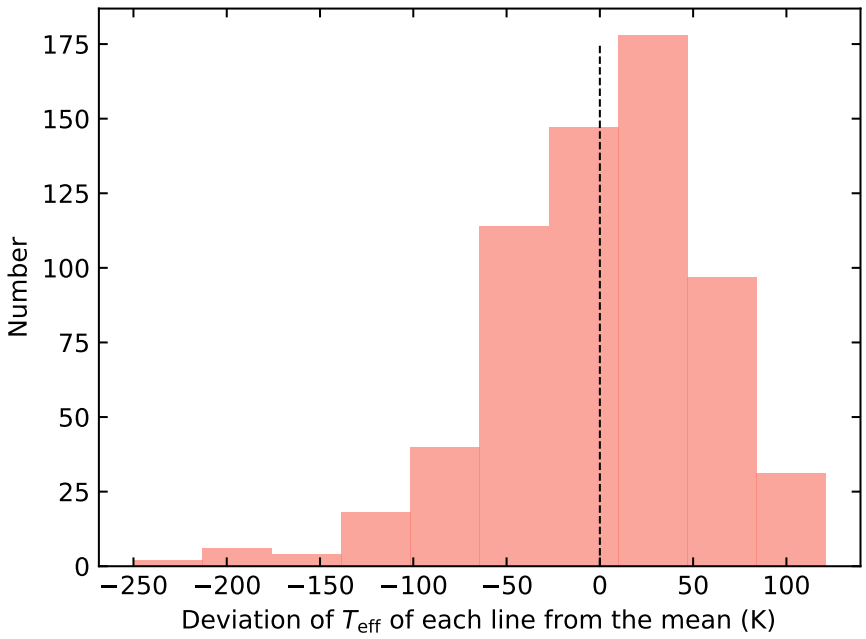

Figure 3.5: The histogram of the deviation of $T_{\rm eff}$ derived from each FeH line from the mean of $T_{\rm eff}$ values from all the FeH lines of corresponding object. The data of the 11 objects with $2900 < T_{\rm eff} < 3200$ is stacked.

We measured the EWs of the FeH lines by fitting the Gaussian profiles to observational data. The Gaussian profiles can fit to the line profiles satisfactorily because the damping wings of the FeH lines are not significant. We obtained $T_{\rm eff}$ from individual FeH lines as the observed EW is reproduced by calculation. The average of all the values is taken as the $T_{\rm eff\text{-}FeH}$ for a certain object. The $\log g = 5.0$, $\xi = 0.5$ km s^{-1}, and [M/H] = 0.0 are assumed throughout the above $T_{\rm eff\text{-}FeH}$ estimation. Figure 3.5 shows the histogram of the result from individual FeH lines. The low-temperature side has a gently extended tail, while the right side shows a steeper drop. The Shapiro-Wilk test results in a p-value far less than 0.05, which means that it is not a normal distribution. The histogram for each object shows a similar shape, suggesting that a particular set of absorption lines might be producing outliers regardless of the object. Other possible causes include contamination by unidentified weak absorption lines, incomplete line parameters, or misestimation of the continuum level in a particular wavelength range. A more stringent selection of absorption lines by examining the $T_{\rm eff}$ from each

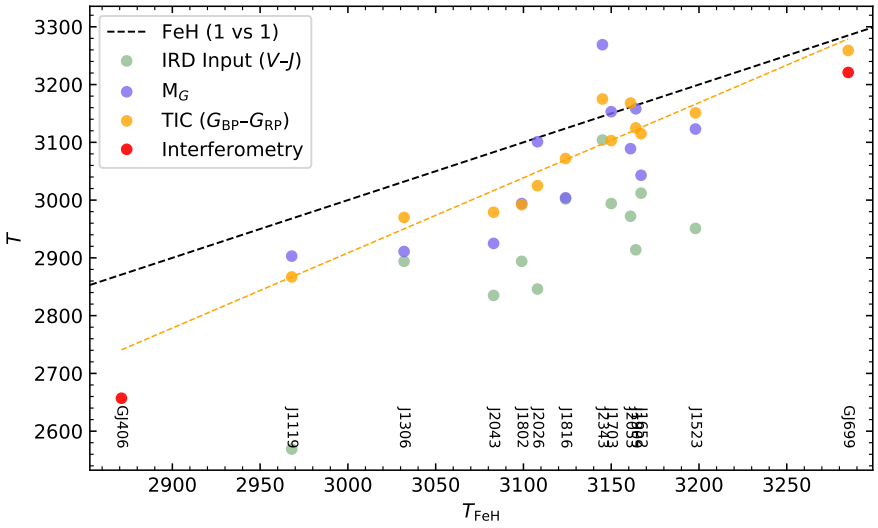

Figure 3.6: Comparison of different estimates of $T_{\rm eff}$. The horizontal axis shows the estimates from the FeH lines in the IRD spectra and the black dashed line shows the unity slope. The green, purple, orange, and red corresponds the $T_{\text{eff-}V-J}$, $T_{\text{eff-}G}$, $T_{\text{eff-TIC}}$, and $T_{\text{eff-interf}}$ in the text, respectively. The orange dashed line shows a linear fit on $T_{\text{eff-TIC}}$.

absorption line and its reasons will improve the accuracy of temperature estimation by the FeH lines.

We compare the $T_{\text{eff-FeH}}$ with different estimates of $T_{\rm eff}$, including $T_{\text{eff-TIC}}$ that we adopted for the abundance analysis, in Figure 3.6. The $T_{\text{eff-TIC}}$ are represented by the orange circles. The green circles are the $T_{\rm eff}$ values in the IRD input catalog, estimated by the empirical relationship between $V-J$ color and $T_{\rm eff}$ provided by Man15 ($T_{\text{eff-}V-J}$). In order to apply the estimation to all the IRD target candidates, the V magnitudes were estimated from the B and R magnitudes of USNO-B Catalog (Monet et al., 2003) and the J magnitudes were drawn from the Two Micron All Sky Survey (2MASS; Skrutskie et al., 2006) for all the objects. The purple circles are the estimates by the empirical relation between the absolute G-band magnitude and $T_{\rm eff}$ calibrated by Rabus et al. (2019). The absolute G-band magnitude is calculated from G-band photometry and parallaxes measured by Gaia.

The $T_{\text{eff-FeH}}$, represented by the black dashed unity line in the figure, lies higher

than most of the other estimates based on the color. Notably, the relative temperatures between the individual objects are shared by $T_{\text{eff-FeH}}$ and $T_{\text{eff-TIC}}$. This implies that these two independent estimates accurately reproduce the relative temperatures between the objects, probably thanks to the high T_{eff} dependence of the FeH lines and $G_{\text{BP}} - G_{\text{RP}}$ color, the substantial number of FeH lines, and the high photometric accuracy of Gaia. However, the difference between $T_{\text{eff-FeH}}$ and $T_{\text{eff-TIC}}$ tends to be larger at lower temperatures, as shown by the linear fit (orange dashed line in the figure). This can be because the $T_{\text{eff-FeH}}$ are indeed precise but not accurate in absolute terms due to the imperfections in the modeling of FeH lines at such low temperatures, such as the treatment of pressure broadening. The deviation of the best-fit synthetic spectra from the observed one is not noticeable for the objects analyzed in this thesis. For cooler objects such as TRAPPIST-1 ($T_{\text{eff}} \sim 2400$–2600 K), nonetheless, we confirmed that the FeH lines in our synthetic spectra have wider wings than observed ones. Thus the $T_{\text{eff-FeH}}$ might be greatly overestimated at such low temperatures.

However, there is also an uncertainty in the empirical T_{eff} estimation based on colors at the lower temperatures. The empirical relation based on the $G_{\text{BP}} - G_{\text{RP}}$ color which was used for deriving $T_{\text{eff-TIC}}$ is calibrated by the objects in Man15, for which Man15 estimated the T_{eff} based on the BT-Settl-model fitting on the medium-resolution spectra. Further, this fitting method in Man15 was originally calibrated by Mann et al. (2013b) (hereafter Man13), but their calibration sample does not include objects cooler than 3238 K. For the lower temperatures, it is undeniable that there still be uncalibrated systematic errors.

The calibration of Man13 is based on T_{eff} calculated by the Stefan-Boltzmann law from the radii directly measured by interferometers and bolometric luminosity. T_{eff} estimation from interferometric measurements ($T_{\text{eff-interf}}$) is reliable because it is model-independent, but the faintness and small angular diameters of late-M dwarfs limit its application with sufficient accuracy to only a few objects very close to the Sun. The coolest example is GJ 406 ($T_{\text{eff-interf}} = 2657 \pm 20$ K) reported by Rabus et al. (2019). The high-resolution near-infrared spectra of this object is available in the CARMENES GTO Data Archive, so we calculated $T_{\text{eff-FeH}}$ and compared it to the $T_{\text{eff-interf}}$ (the left red circle in Figure 3.6). Adopting the linear relation between $T_{\text{eff-FeH}}$ and $T_{\text{eff-TIC}}$ (the orange dashed line), the provisional $T_{\text{eff-TIC}}$ estimated from our $T_{\text{eff-FeH}}$ is 2741 K. Its difference from the $T_{\text{eff-interf}}$ is well within the typical scatter. This suggests that the T_{eff}

estimation based on the EW of the FeH lines may retain to be useful even for such cool objects. The extension of the reach of interferometric measurements to cooler M dwarfs is expected to drive the further understanding of the accurate $T_{\rm eff}$ in this regime.

It should be noted that GJ 406 is magnetically active. Reiners et al. (2018) reported the significant emission of Hα ($\mathrm{EW}_{\mathrm{H}\alpha} \sim -9.25$ Å). We confirmed that the magnetically sensitive FeH lines are wider than magnetically insensitive lines due to the Zeeman effect. The FeH lines being clearly affected by the Zeeman effect are excluded from the $T_{\rm eff\text{-}FeH}$ estimation of the object. The IRD-SSP sample does not include magnetically active M dwarfs, but if we want to go beyond that and analyze the magnetically active ones, we need to select the lines taking the Landé g-factors into consideration.

On the other hand, looking at the higher side of $T_{\rm eff}$, $T_{\rm eff\text{-}FeH}$, $T_{\rm eff\text{-}TiC}$, and $T_{\rm eff\text{-}interf}$ are in good agreement. The rightmost objects in Figure 3.6 show the convergence of the estimates for GJ 699 at around 3250 K. Although it is not shown in the figure, the corresponding estimates for GJ 436 also well agree with each other within 40 K (3440 K, 3456 K, 3416 K, respectively). These two examples support the view that the $T_{\rm eff}$ discrepancy between the methods is due to problems specific to low temperatures.

3.3.3 Equivalent width measurement

We determined the abundances of individual elements based on the comparison between the EWs in observed spectra and those of synthetic ones.

The spectral lines were selected based on the same line set as Section 2.3.3. We investigated the behavior of the absorption lines using synthetic spectra and confirmed that the sensitivity of most lines to the metallicity and stellar parameters is comparable even at the lower temperature range ($2900 < T_{\rm eff} < 3200$ K) with that at ~3200 K. However, all the three K I lines becomes much more sensitive to $T_{\rm eff}$ rather than [K/H] at the low temperature, so we removed K from the analysis of all the targets except for the hottest target GJ 436. On the other hand, we added some lines which were unavailable in the CARMENES spectra due to the detector gaps, thanks to the high continuity of the wavelength coverage of IRD. One of the notable lines is the Sr II line at 1091.79 nm. We analyzed it for all the objects to determine [Sr/H]. Another notable line is the Si I line at 1198.75 nm, which is the only one detectable Si I line in the wavelength range of IRD for late-M dwarfs, but we found it is not [Si/H]-sensitive

enough at the lower $T_{\rm eff}$. We used the line only for GJ 436 together with two other Si I lines which are not detectable for the other objects. We also added a V I line at 1225.28 nm only for GJ 436 due to the relatively high abundance-sensitivity at higher $T_{\rm eff}$.

Table 3.3: Atomic line list

Species	λ (nm)*	$E_{\rm low}$ (eV)†	$\log gf$‡	vdW §
Na I	1074.9393	3.191	-1.294	N/A
Na I	1083.7814	3.617	-0.503	N/A
Na I	1268.2639	3.617	-0.043	-6.653
Mg I	1183.1409	4.346	-0.333	-7.192
Si I	1078.9804	4.930	-0.303	-7.272
Si I	1083.0054	4.954	0.302	-7.266
Si I	1198.7478	4.930	0.239	-7.298
K I	1177.2861	1.617	-0.450	-7.326
K I	1243.5675	1.610	-0.439	-7.022
Ca I	1083.6349	4.877	-0.244	-7.590
Ca I	1195.9227	4.131	-0.849	-7.300
Ca I	1195.9228	4.131	-0.849	-7.300
Ca I	1281.9551	3.910	-0.765	-7.520
Ca I	1282.7375	3.910	-0.997	-7.520
Ca I	1283.0568	3.910	-1.478	-7.520
Ca I	1291.2601	4.430	-0.224	-7.710
Ca I	1303.7119	4.441	-0.064	-7.710
Ca I	1306.1457	4.441	-1.092	-7.710
Ca I	1313.8534	4.451	0.085	-7.710
Ti I	967.8197	0.836	-0.804	-7.800
Ti I	972.1625	1.503	-1.181	-7.780
Ti I	972.1626	1.503	-1.181	-7.780
Ti I	973.1075	0.818	-1.206	-7.800
Ti I	974.6277	0.813	-1.306	-7.800
Ti I	974.6278	0.813	-1.306	-7.800
Ti I	977.2980	0.848	-1.581	-7.800

Table 3.3 (Continued)

Species	λ (nm)*	E_{low} (eV)†	$\log gf$‡	vdW §
Ti I	979.0371	0.826	-1.444	-7.800
Ti I	979.0372	0.826	-1.444	-7.800
Ti I	983.4836	1.887	-1.130	-7.634
Ti I	1000.5831	2.160	-1.210	-7.780
Ti I	1005.1583	1.443	-1.930	-7.780
Ti I	1039.9651	0.848	-1.539	-7.810
Ti I	1058.7533	0.826	-1.775	-7.810
Ti I	1061.0624	0.848	-2.697	-7.810
Ti I	1066.4544	0.818	-1.915	-7.810
Ti I	1073.5804	0.826	-2.515	-7.810
Ti I	1077.7818	0.818	-2.666	-7.810
Ti I	1083.0863	0.836	-3.910	-7.810
Ti I	1085.0605	0.826	-3.922	-7.810
Ti I	1180.0415	1.430	-2.280	-7.790
Ti I	1180.0416	1.430	-2.280	-7.790
Ti I	1189.6132	1.430	-1.730	-7.790
Ti I	1281.4983	2.160	-1.390	-7.750
Ti I	1282.5179	1.460	-1.190	-7.790
Ti I	1282.5180	1.460	-1.190	-7.790
Ti I	1292.3433	2.154	-1.560	-7.750
Ti I	1292.3433	2.153	-1.560	-7.750
V I	1225.2755	2.359	-0.999	-7.780
Cr I	1065.0557	3.011	-1.582	-7.770
Cr I	1080.4319	3.011	-1.562	-7.780
Cr I	1081.9873	3.013	-1.894	-7.780
Cr I	1082.4625	3.013	-1.520	-7.780
Cr I	1090.8697	3.438	-0.561	-7.530
Cr I	1093.2864	3.010	-1.858	-7.780
Cr I	1139.3869	3.322	-0.423	-7.640
Cr I	1161.3739	3.321	0.055	-7.640

Table 3.3 (Continued)

Species	λ (nm)*	$E_{\rm low}$ (eV)†	$\log gf$‡	vdW §
Cr I	1291.3622	2.708	-1.779	-7.800
Cr I	1294.0559	2.710	-1.896	-7.800
Mn I	1290.3289	2.114	-1.070	N/A
Mn I	1297.9459	2.888	-1.090	N/A
Fe I	1038.1843	2.223	-4.148	-7.800
Fe I	1039.8643	2.176	-3.393	-7.800
Fe I	1042.5884	2.692	-3.616	-7.810
Fe I	1061.9630	3.267	-3.127	-7.780
Fe I	1078.6004	3.111	-2.567	-7.790
Fe I	1082.1238	3.960	-1.948	-7.820
Fe I	1088.4739	2.845	-3.604	-7.810
Fe I	1088.7244	3.929	-1.925	-7.820
Fe I	1089.9284	3.071	-2.694	-7.790
Fe I	1288.3289	2.279	-3.458	-7.820
Sr I	1091.7877	1.805	-0.526	-7.641

* Wavelength in vacuum † Lower excitation potential

‡ Oscillator strength § Van der Waals damping parameter

We measure the EWs of all the atomic lines of interest by fitting the synthesized spectra, in contrast to Chapter 2 where we measure them, except for Na I and Mn I lines, by fitting the Gaussian or Voigt profiles. Synthetic spectra can reproduce the line profile more accurately than the Gaussian and Voigt profiles, especially of relatively broad lines. We initially fixed for all objects the selected line list and each wavelength range to fit for each line. The wavelength range was selected to cover the line profile from the wings to the core, while avoiding wavelengths where contamination is suspected. This allows us to measure EW automatically and consistently for all objects. If there are other absorption lines in close proximity for which reliable data are available, we fitted the synthetic spectra including not only the lines of interest but also those contaminations. The EW of the lines of interest alone was then calculated by employing the best-fit abundance of the corresponding element.

Subsequently, we visually check the agreement between the best-fit synthesized spectrum and the observed one for each line because the automatic fitting does not necessarily return the best solutions. Absorption lines with unreasonable fittings, for example of an apparent discrepancy of the profile, a too weak detection almost hidden in the noise level, or a doubtful continuum level, were removed. The number of absorption lines excluded here is only a few at most for each object. The flux discrepancy tends to be found at the line cores of some deep lines, which suggests the imperfection of the upper layer of model atmospheres. This might be due to the effect of non-LTE as pointed out by Olander et al. (2021).

3.3.4 Kinematics

For the purpose of kinematic classification of the Galactic populations, we calculated the Galactocentric space velocities of each M dwarf.

We firstly measured the radial velocity ($v_{\rm rad}$) using the IRD spectra in a relatively telluric-free part, i.e. 1030–1330 nm. In this wavelengths, we took the cross-correlation between the observed spectra and synthetic spectra calculated from the VALD line list and the MARCS model atmosphere with $T_{\rm eff}$ = 3000 K, $\log g$ = 5.0, and [Fe/H] = 0.0 to obtain the relative velocity. The barycentric correction is made for the obtained relative velocity. We shifted these velocities by -0.1 km s^{-1} for all our M dwarfs such that the velocity of GJ 699 measured by the same procedure matches the value from Reiners et al. (2018).

Secondly, the space velocities UVW were calculated by combining the $v_{\rm rad}$ with the astrometric measurements (i.e. coordinates, proper motions, and parallaxes) in Gaia DR2 (Gaia Collaboration et al., 2018). The U, V, and W are, respectively, the radial, azimuthal, and vertical components of Galactocentric space velocities with respect to the local standard of rest (LSR). They are calculated adopting the Sun-Galactic center distance of 8.2 kpc (McMillan, 2017), the height of the Sun above the Galactic midplane of 0.025 kpc (Jurić et al., 2008), and the solar motion relative to the LSR of ($U_\odot$, $V_\odot$, $W_\odot$) = (11.10, 12.24, 7.25) km s^{-1} (Schönrich et al., 2010). The coordinate transformation to the Galactocentric Cartesian system was conducted with the astropy.coordinates package.

Table 3.4 lists the radial velocities $v_{\rm rad}$ and the space velocities UVW of our M

Table 3.4: Kinematics of the target M dwarfs

Object	$v_{\rm rad}$ (km s^{-1})	U (km s^{-1})	V (km s^{-1})	W (km s^{-1})
GJ 436	9.5	61.3	-6.3	26.2
GJ 699	-110.6	-130.2	17.0	26.0
LSPM J1306+3050	9.8	39.4	-6.0	18.3
LSPM J1523+1727	42.2	68.4	-37.7	37.5
LSPM J1652+6304	-21.1	3.3	2.9	-15.7
LSPM J1703+5124	37.3	-9.9	51.2	24.5
LSPM J1802+3731	4.1	72.5	-0.5	-16.1
LSPM J1909+1740	-13.8	27.0	-20.0	24.5
LSPM J2026+5834	-59.4	-12.1	-48.2	-1.0
LSPM J1816+0452	-53.2	-47.0	-1.5	20.3
LSPM J2043+0445	-48.1	-31.1	-27.1	-5.5
LSPM J2053+1037	-20.2	36.3	-21.9	22.9
LSPM J2343+3632	-2.9	-18.4	-7.1	-6.5
HD 233153	2.0	-3.2	-10.3	-6.7
HD154363B	34.7	58.2	-49.1	28.2
BX Cet	70.4	-94.5	21.4	7.1
G102-4	17.3	-0.4	-12.2	0.8
rho Cnc B	73.3	-60.4	-17.0	27.7
BD-02 2198	-17.1	35.9	8.3	-0.4

dwarfs. It also includes the kinematics of the six M dwarfs in Chapter 2 for which we adopt the $v_{\rm rad}$ from Reiners et al. (2018).

3.4 Results

3.4.1 Elemental abundance

The results and corresponding errors of elemental abundance determination from the IRD-SSP data are tabulated in Table 3.5 and plotted in Figure 3.7.

Table 3.5: Abundance results with individual error sources

Object	Element	[X/H]	$N_{\rm line}$	$\sigma_{\rm SEM}$	$\sigma_{T_{\rm eff}}$	$\sigma_{\log g}$	σ_{ξ}	$\sigma_{\rm OE}$	$\sigma_{\rm cont}$	$\sigma_{\rm Total}$
GJ 436	Na	0.02	2	0.12	0.11	0.00	0.01	0.07	0.04	0.19
	Mg	0.03	2	0.12	0.07	0.01	0.00	0.15	0.03	0.21

Table 3.5 (Continued)

Object	Element	[X/H]	N_{line}	σ_{SEM}	$\sigma_{T_{\mathrm{eff}}}$	$\sigma_{\log g}$	σ_{ξ}	σ_{OE}	σ_{cont}	σ_{Total}
	Si	-0.03	3	0.10	0.35	0.01	0.01	0.18	0.05	0.41
	K	-0.08	2	0.12	0.21	0.00	0.02	0.10	0.03	0.27
	Ca	0.04	9	0.05	0.05	0.00	0.01	0.11	0.02	0.13
	Ti	0.20	22	0.02	0.03	0.01	0.03	0.21	0.02	0.22
	V	0.18	1	0.18	0.01	0.00	0.01	0.09	0.08	0.22
	Cr	0.08	10	0.04	0.02	0.00	0.02	0.12	0.03	0.13
	Mn	0.17	3	0.10	0.04	0.01	0.02	0.16	0.03	0.20
	Fe	0.04	10	0.06	0.03	0.00	0.02	0.11	0.03	0.13
	Sr	0.08	1	0.18	0.03	0.01	0.04	0.15	0.09	0.26
GJ 699	Na	-0.61	2	0.20	0.18	0.01	0.00	0.07	0.03	0.27
	Mg	-0.52	1	0.28	0.07	0.02	0.01	0.19	0.04	0.35
	Ca	-0.68	9	0.05	0.07	0.01	0.00	0.09	0.02	0.13
	Ti	-0.56	21	0.02	0.22	0.02	0.01	0.23	0.01	0.32
	Cr	-0.70	8	0.04	0.06	0.00	0.00	0.12	0.03	0.14
	Mn	-0.86	2	0.20	0.13	0.01	0.01	0.16	0.04	0.29
	Fe	-0.60	7	0.11	0.06	0.00	0.01	0.12	0.03	0.18
	Sr	-0.66	1	0.28	0.01	0.00	0.01	0.16	0.08	0.33
LSPM J1306+3050	Na	-0.24	3	0.18	0.17	0.01	0.00	0.10	0.02	0.27
	Mg	-0.26	1	0.32	0.14	0.03	0.00	0.19	0.04	0.40
	Ca	-0.18	3	0.18	0.06	0.01	0.00	0.12	0.03	0.23
	Ti	-0.09	20	0.03	0.30	0.04	0.01	0.30	0.01	0.43
	Cr	-0.11	8	0.07	0.11	0.01	0.00	0.13	0.02	0.18
	Mn	-0.26	2	0.23	0.23	0.02	0.00	0.17	0.03	0.37
	Fe	-0.09	6	0.13	0.13	0.01	0.00	0.13	0.03	0.23
	Sr	-0.17	1	0.32	0.06	0.00	0.00	0.17	0.08	0.37
LSPM J1523+1727	Na	-0.33	3	0.13	0.20	0.01	0.00	0.08	0.02	0.25
	Mg	-0.21	1	0.22	0.12	0.02	0.00	0.19	0.04	0.32
	Ca	-0.29	3	0.13	0.10	0.01	0.00	0.12	0.03	0.20
	Ti	-0.14	20	0.03	0.28	0.03	0.01	0.27	0.01	0.39
	Cr	-0.22	8	0.04	0.11	0.01	0.00	0.13	0.03	0.17
	Mn	-0.40	2	0.16	0.20	0.02	0.01	0.17	0.03	0.31
	Fe	-0.20	6	0.09	0.12	0.01	0.01	0.13	0.03	0.20
	Sr	-0.24	1	0.22	0.02	0.01	0.01	0.18	0.08	0.30
LSPM J1652+6304	Na	-0.04	3	0.17	0.26	0.01	0.00	0.13	0.02	0.34
	Mg	0.07	1	0.29	0.17	0.01	0.00	0.18	0.04	0.39
	Ca	0.04	3	0.17	0.15	0.00	0.00	0.13	0.03	0.26
	Ti	0.30	20	0.03	0.36	0.02	0.02	0.32	0.01	0.48

Table 3.5 (Continued)

Object	Element	[X/H]	N_{line}	σ_{SEM}	$\sigma_{T_{\mathrm{eff}}}$	$\sigma_{\log g}$	σ_{ξ}	σ_{OE}	σ_{cont}	σ_{Total}
	Cr	0.09	8	0.04	0.16	0.00	0.01	0.14	0.03	0.22
	Mn	0.03	2	0.21	0.29	0.01	0.01	0.19	0.03	0.41
	Fe	0.08	6	0.12	0.17	0.00	0.01	0.14	0.03	0.25
	Sr	0.12	1	0.29	0.05	0.01	0.01	0.16	0.09	0.35
LSPM J1703+5124	Na	0.18	3	0.12	0.30	0.03	0.02	0.15	0.02	0.36
	Mg	0.18	1	0.21	0.20	0.03	0.02	0.18	0.04	0.34
	Ca	0.18	3	0.12	0.18	0.02	0.02	0.14	0.03	0.26
	Ti	0.54	20	0.03	0.42	0.05	0.05	0.33	0.01	0.54
	Cr	0.20	8	0.04	0.19	0.02	0.02	0.14	0.03	0.24
	Mn	0.20	2	0.15	0.34	0.03	0.03	0.20	0.04	0.42
	Fe	0.23	6	0.08	0.20	0.02	0.03	0.14	0.03	0.26
	Sr	0.23	1	0.21	0.05	0.01	0.03	0.15	0.09	0.28
LSPM J1802+3731	Na	-0.21	3	0.16	0.18	0.01	0.00	0.11	0.02	0.26
	Mg	-0.15	1	0.28	0.13	0.03	0.00	0.19	0.04	0.36
	Ca	-0.11	3	0.16	0.07	0.01	0.00	0.12	0.03	0.21
	Ti	-0.07	20	0.04	0.30	0.04	0.01	0.31	0.01	0.43
	Cr	-0.08	8	0.06	0.11	0.01	0.00	0.13	0.02	0.18
	Mn	-0.27	2	0.20	0.23	0.02	0.00	0.17	0.03	0.35
	Fe	-0.05	6	0.11	0.13	0.01	0.00	0.14	0.03	0.22
	Sr	-0.05	1	0.28	0.05	0.00	0.01	0.17	0.08	0.34
LSPM J1816+0452	Na	0.45	3	0.15	0.38	0.04	0.02	0.17	0.02	0.44
	Mg	0.33	1	0.25	0.27	0.04	0.02	0.18	0.04	0.42
	Ca	0.28	3	0.15	0.22	0.03	0.01	0.14	0.03	0.31
	Ti	0.88	20	0.02	0.54	0.07	0.05	0.34	0.01	0.65
	Cr	0.36	8	0.04	0.25	0.03	0.02	0.14	0.03	0.30
	Mn	0.47	2	0.18	0.43	0.05	0.03	0.21	0.04	0.51
	Fe	0.37	6	0.10	0.26	0.03	0.03	0.14	0.04	0.32
	Sr	0.41	1	0.25	0.11	0.02	0.03	0.15	0.10	0.33
LSPM J1909+1740	Na	0.12	3	0.13	0.28	0.03	0.01	0.14	0.02	0.35
	Mg	0.15	1	0.23	0.17	0.03	0.01	0.18	0.04	0.34
	Ca	0.11	3	0.13	0.16	0.02	0.01	0.14	0.03	0.25
	Ti	0.48	20	0.02	0.38	0.05	0.04	0.32	0.01	0.50
	Cr	0.16	8	0.04	0.17	0.02	0.02	0.14	0.03	0.23
	Mn	0.16	2	0.16	0.31	0.03	0.02	0.20	0.04	0.40
	Fe	0.18	6	0.09	0.18	0.02	0.02	0.14	0.03	0.25
	Sr	0.16	1	0.23	0.05	0.01	0.02	0.15	0.09	0.29
LSPM J2026+5834	Na	0.15	3	0.16	0.31	0.03	0.01	0.15	0.02	0.38

Table 3.5 (Continued)

Object	Element	[X/H]	$N_{\rm line}$	$\sigma_{\rm SEM}$	$\sigma_{T_{\rm eff}}$	$\sigma_{\log g}$	σ_{ξ}	$\sigma_{\rm OE}$	$\sigma_{\rm cont}$	$\sigma_{\rm Total}$
	Mg	0.05	1	0.27	0.23	0.04	0.01	0.19	0.04	0.41
	Ca	0.05	3	0.16	0.16	0.02	0.01	0.13	0.03	0.26
	Ti	0.36	20	0.03	0.47	0.06	0.02	0.34	0.01	0.58
	Cr	0.11	8	0.06	0.20	0.02	0.01	0.14	0.03	0.25
	Mn	0.12	2	0.19	0.37	0.04	0.01	0.20	0.03	0.47
	Fe	0.16	6	0.11	0.22	0.02	0.01	0.15	0.03	0.29
	Sr	0.17	1	0.27	0.05	0.01	0.01	0.15	0.09	0.33
LSPM J2043+0445	Na	0.41	3	0.19	0.42	0.05	0.01	0.17	0.02	0.49
	Mg	0.27	1	0.32	0.34	0.06	0.01	0.19	0.04	0.51
	Ca	0.29	3	0.19	0.26	0.04	0.01	0.14	0.03	0.35
	Ti	0.75	20	0.03	0.66	0.10	0.04	0.36	0.01	0.76
	Cr	0.33	8	0.06	0.29	0.04	0.01	0.15	0.03	0.34
	Mn	0.41	2	0.23	0.50	0.07	0.02	0.21	0.03	0.59
	Fe	0.39	6	0.13	0.32	0.04	0.02	0.15	0.03	0.38
	Sr	0.42	1	0.32	0.12	0.03	0.02	0.14	0.09	0.39
LSPM J2053+1037	Na	-0.13	3	0.11	0.22	0.01	0.00	0.11	0.02	0.26
	Mg	-0.08	1	0.19	0.12	0.02	0.01	0.19	0.04	0.29
	Ca	-0.12	3	0.11	0.11	0.01	0.01	0.13	0.03	0.20
	Ti	0.17	20	0.02	0.29	0.03	0.02	0.29	0.01	0.41
	Cr	-0.09	8	0.04	0.11	0.01	0.01	0.13	0.03	0.18
	Mn	-0.10	2	0.13	0.23	0.02	0.01	0.18	0.03	0.32
	Fe	-0.05	6	0.08	0.12	0.01	0.01	0.14	0.03	0.20
	Sr	0.01	1	0.19	0.03	0.01	0.02	0.17	0.09	0.27
LSPM J2343+3632	Na	-0.04	3	0.12	0.23	0.01	0.00	0.12	0.02	0.29
	Mg	0.04	1	0.21	0.12	0.02	0.01	0.18	0.04	0.31
	Ca	-0.06	3	0.12	0.12	0.01	0.01	0.13	0.03	0.22
	Ti	0.31	20	0.02	0.29	0.02	0.03	0.30	0.01	0.42
	Cr	-0.06	8	0.03	0.12	0.01	0.01	0.13	0.03	0.18
	Mn	0.05	2	0.15	0.24	0.01	0.02	0.19	0.04	0.34
	Fe	-0.00	6	0.09	0.13	0.01	0.02	0.14	0.03	0.21
	Sr	0.13	1	0.21	0.04	0.01	0.02	0.17	0.09	0.29

The symbol of each error source is the same as Table 2.4

The abundance ratios of individual elements are generally aligned with those of iron in all M dwarfs, with no stars showing a peculiar abundance pattern. We also calculated

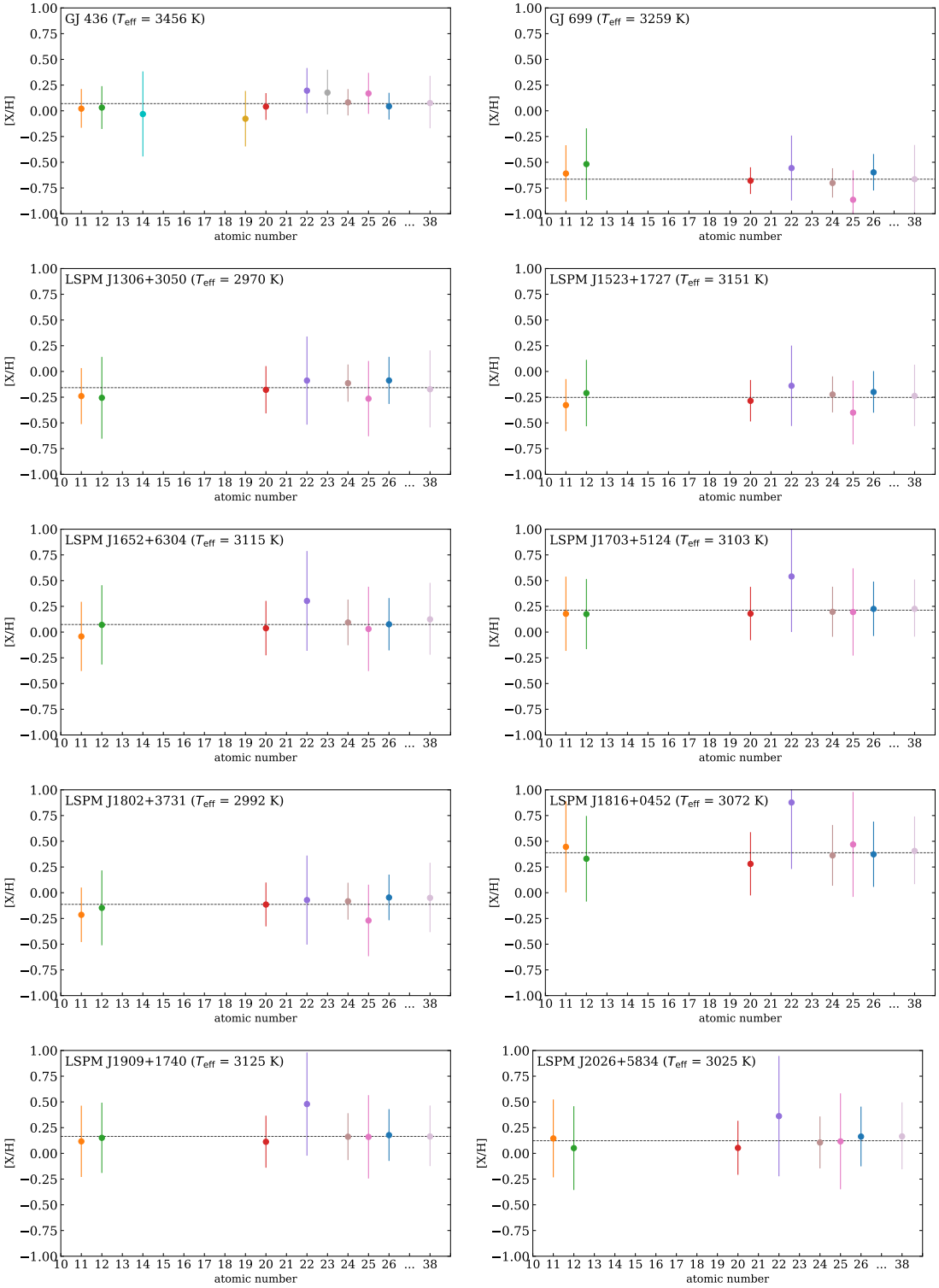

Figure 3.7: Abundance ratios [X/H] of individual elements for each M dwarfs as a function of atomic number. The error sizes are the $\sigma_{\rm Total}$ estimated in Section 3.3.3 as in Figure 2.4. The horizontal dashed line indicates the average of all the elements [$M_{\rm ave}$/H], weighted by the inverse of the square of the errors.

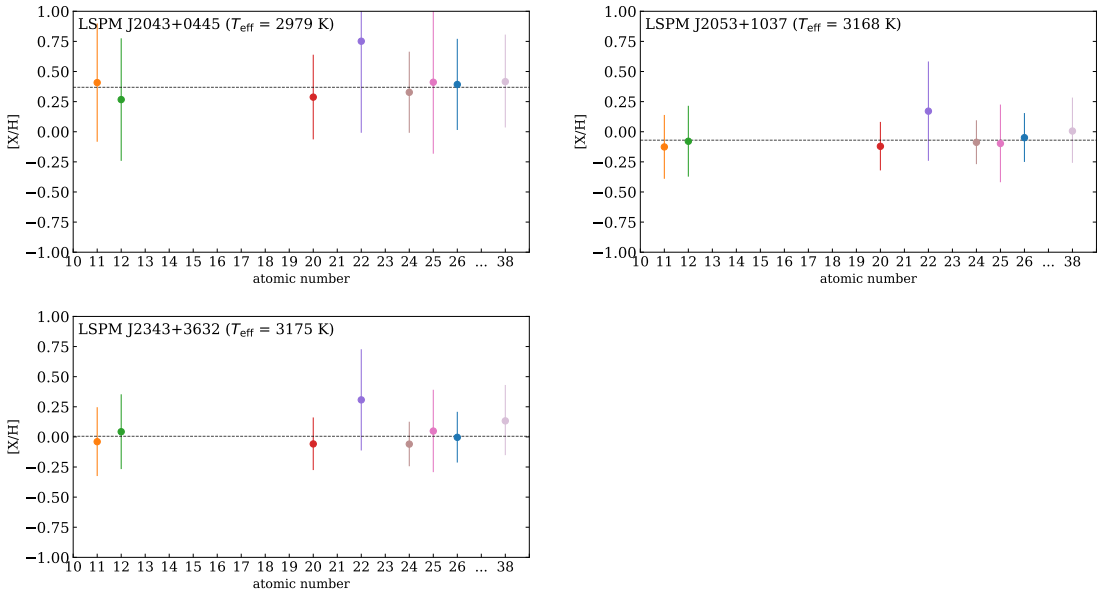

Figure 3.7: (Continued)

an error-weighted average of abundances of all the elements for each object ([M_{ave}/H]; the horizontal dashed lines in Figure 3.7) and confirmed that none of the elements deviate from it in all objects beyond the measurement errors.

Following the caveats discussed in Section 2.5.1, we determined the abundances of individual elements so that the assumed abundance of each element is consistent with the resulting abundance. The similarity of the abundance patterns to the Sun derived by the analysis for individual elements indicates that scaled-solar abundance ratios could be a good approximation for these M dwarfs.

The [M_{ave}/H] ranges from ~ -0.6 to $\sim +0.4$, centered around the solar value. These differences in metallicity can be visually confirmed by the difference in depth of a Na I line shown in Figure 3.8. We show the Na I line here because Na I lines are relatively insensitive to the abundances of other elements as investigated in the previous Chapter.

Sodium is one of the most important elements in terms of the contribution to the continuum opacity as discussed in the previous Chapter. We found that the precision of the [Na/H] determination is degraded with increasing [M_{ave}/H] values among the objects with similar temperatures. Figure 3.9 presents a comparison of the amount of

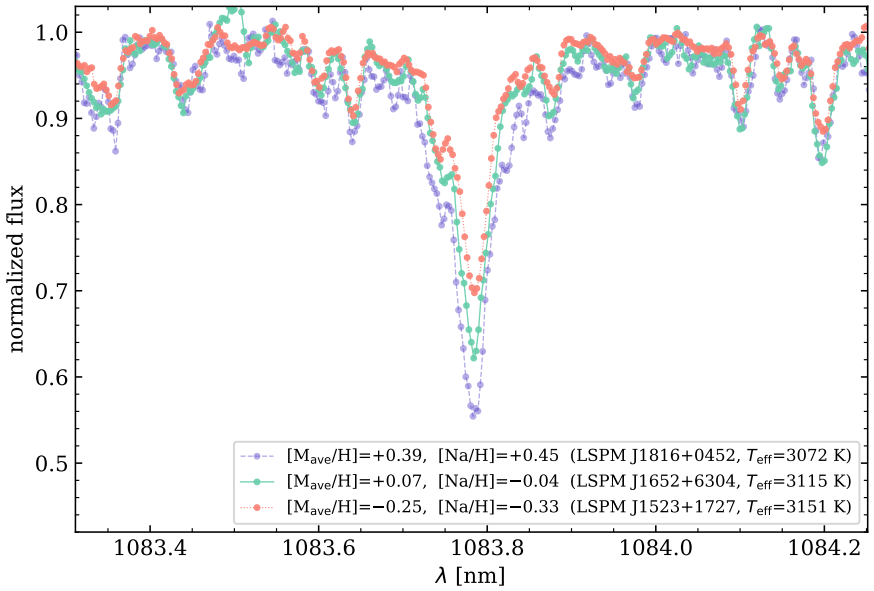

Figure 3.8: The IRD spectra around a Na I line (1083.78 nm) of M dwarfs at $T_{\rm eff} \sim 3100$ K with the low metallicity, high metallicity, and in-between.

errors in [Na/H] caused by individual error sources for 11 M dwarfs with temperatures of $2900 < T_{\rm eff} < 3200$ K. The error source $\sigma_{T_{\rm eff}}$ mainly contribute to the trend from lower left to upper right and $\sigma_{\rm OE}$ and $\sigma_{\log g}$ also show gradual upward trends. These trends are also observed in other elements, which may be attributed to the fact that the stronger the absorption lines, the more insensitive they become to the elemental abundance, due to effects such as the saturation of line core. Figure 3.9 also shows that the error source dominating total errors in most objects is the uncertainty of $T_{\rm eff}$, not the data quality or other parameters. If the $\sigma_{T_{\rm eff}}$ can be suppressed more by such as an increase of interferometric measurements, the total precision of abundance determination would be improved.

Although Mg is also an important element, the errors are relatively large because only one broad absorption line is available for the analysis. We have identified several Mg I lines in the H-band, but they are all heavily contaminated in unidentified absorption lines and cannot be measured reliably. In the future, when the data of molecular absorption lines in this band are advanced and the features around the Mg I

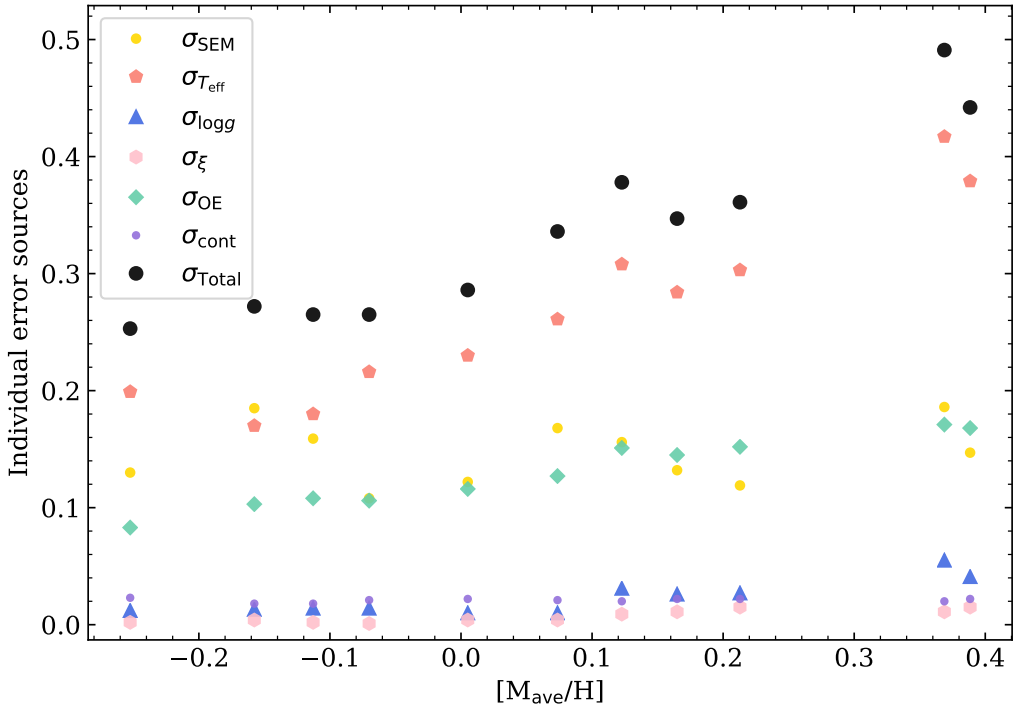

Figure 3.9: Size of errors associated with the resulting [Na/H] caused by individual error sources for the 11 targets with $T_{\rm eff} < 3200$ K as a function of [M$_{\rm ave}$/H] of the objects. The $\sigma_{\rm SEM}$ is a random error. The $\sigma_{T_{\rm eff}}$, $\sigma_{\log g}$, and σ_{ξ} are errors propagated from the corresponding stellar parameters. The $\sigma_{\rm OE}$ and $\sigma_{\rm cont}$ are the errors due to uncertainties of other elements and errors associated with the continuum level uncertainty, respectively. The $\sigma_{\rm Total}$ is the quadrature sum of all the above errors.

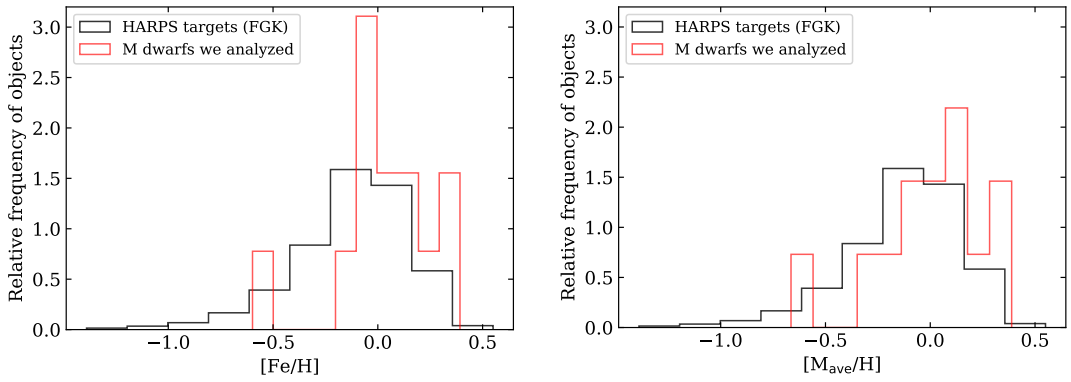

Figure 3.10: Distribution of 13 M dwarfs analyzed in this chapter in the iron abundance (red histogram in the right panel) and in the error-weighted average of abundances of all the elements (red histogram in the left panel). The black histograms in both panels are the distribution of [Fe/H] values of 1111 FGK dwarfs reported in Adibekyan et al. (2012a), where the [Fe/H] is treated as a proxy of overall metallicity.

lines can be reproduced with synthetic spectra, those lines could be used to further constrain [Mg/H].

Figure 3.10 shows the distribution of our M dwarfs for iron abundance [Fe/H] (left panel) and averaged metallicity [M_{ave}/H] (right panel). The [Fe/H] of 1111 FGK stars observed within the HARPS GTO planet search program (Mayor et al., 2003), which are chemically characterized by Adibekyan et al. (2012a) (hereafter Adi12), are also shown as a reference. We note that [Fe/H] in the literature is treated as an indicator of overall metallicity and then [M/H] is not given separately. The selection of the FGK stars was also for the purpose of an RV survey and therefore share similar criteria with the IRD-SSP targets, such as mild rotation and low level of chromospheric activity. The distributions of our M dwarfs are centered around the solar value but seem to slightly shift toward the metal-rich side against the distribution of the FGK stars.

To compare between the [Fe/H] or [M_{ave}/H] of the M dwarfs and the [Fe/H] of the FGK stars, we used the Mann-Whitney U-test because the number of the samples was different and the Shapiro-Wilk test suggests that a normal distribution cannot be assumed. The resulting p-value is 0.021 and 0.055 in the case of [Fe/H] and [M_{ave}/H], respectively. We thus can reject the null hypothesis of equality of distribution in the case of using [Fe/H] at the significance level of 5 %. Systematics due to analytical

problems, such as the collection of the used lines or the adopted stellar parameters including the possible systematic error in the adopted $T_{\rm eff\text{-}TIC}$, may have led to an overestimation of the [Fe/H]. The possible systematic error in the adopted $T_{\rm eff\text{-}TIC}$ and its effect on the abundance results are discussed in more detail in Section 3.5.2. Note that the Mann-Whitney U-test between the distribution of [Fe/H] and [$M_{\rm ave}$/H] (p = 0.76) does not reject their equality and the difference between the averages for 13 objects of [Fe/H] (~ +0.04 dex) and [$M_{\rm ave}$/H] (~ +0.01 dex) is much less than the typical error. We need a larger sample to confirm or refute the possible overestimation of iron abundances.

Given the long life of the M dwarfs and the selection bias of the IRD-SSP targets toward magnetically inactive ones, it is more natural to think that they are biased toward lower metallicities if detectable. On the other hand, if the initial mass function has a dependence on metallicity, it could make difference in metallicity distribution.

Besides, the distribution of our M dwarfs seems to lack the extended tail of low-metallicity objects that is clearly shown by the FGK stars, although the sample is too small to be conclusive. The extension of the analysis to the other IRD-SSP targets will corroborate these discussions.

3.4.2 Comparison with literatures for the 11 objects with 2900 $< T_{\rm eff} <$ 3200

We compare the resulting iron abundances of eleven M dwarfs with $T_{\rm eff} < 3200$ K with the overall metallicity estimated by previous studies. One of the previous estimates is obtained from an empirical relation of metallicity against the location in the $(J-K)$–$(V-K)$ color–color diagram calibrated by Johnson et al. (2012). Other estimates are those from Newton et al. (2014) (hereafter New14), who derived the [Fe/H] empirically from the EW of Na doublet at 2.2 μm (K-band). These metallicity estimates agree with our [Fe/H] values with a scatter of ~0.1 dex, which is below the expected uncertainty, as shown in the top panel of Figure 3.11. The other small panels demonstrate that the differences do not have significant systematic trend with $T_{\rm eff}$ or [Fe/H].

However, Newton et al. (2015) points out that the method of New14 overestimates the metallicities of late-M dwarfs (M5V and later) compared with the more accurate

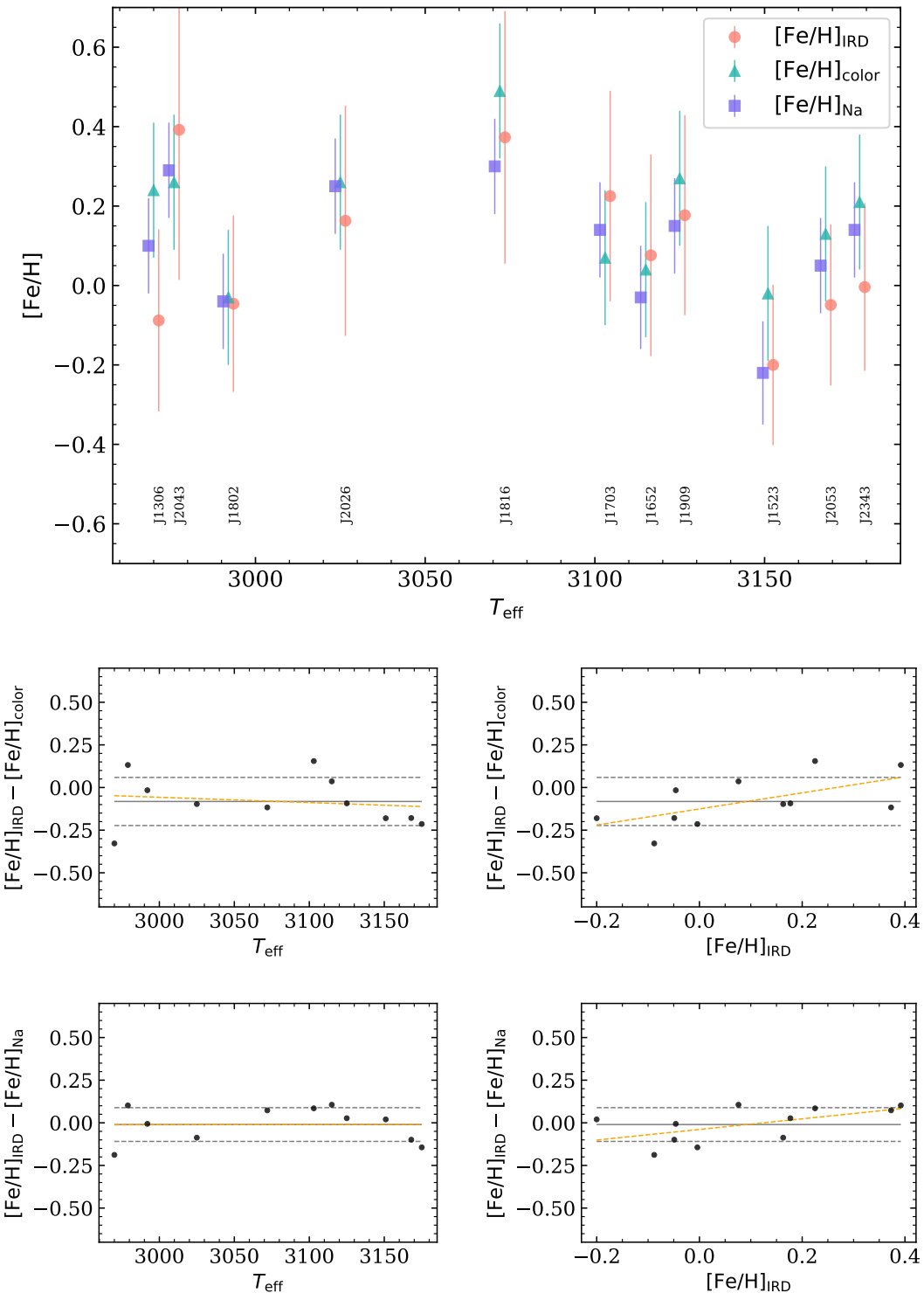

Figure 3.11: Comparison between our resulting [Fe/H] values and the previous estimates of the overall metallicity. The red circles are our results. The green triangles are the estimates from the location in the $(J-K)$–$(V-K)$ color–color diagram. The purple squares are the estimates from the EW of Na doublet at 2.2 μm. The lower four small panels show that the differences between our results and the previous estimates as a function of $T_{\rm eff}$ or [Fe/H], where the gray solid lines, gray dashed lines, and orange dashed lines represent the mean, 1σ scatter, and the fitted linear trend, respectively.

estimation by Mann et al. (2014) by up to ~0.2 dex. Possible reasons are that their estimation does not take the impact of $T_{\rm eff}$ into account and their calibration sample is heavily biased toward mid-M dwarfs. If the overestimation of our resulting [Fe/H] suggested in Section 3.4.1 is true, it would be consistent with the indication of Newton et al. (2015).

3.4.3 Comparison with literatures for Barnard's star

One of the other targets with $T_{\rm eff} > 3200$ K is GJ 699 (Barnard's star). It is a well-studied bright and high proper-motion M dwarf and the closest single star to the Solar System. It is also famous for the RV detection of a super-Earth candidate orbiting near its snow line by Ribas et al. (2018). Its metallicity has been estimated in literature with a variety of methods, including Man15 and New14.

We compared our [Fe/H] with estimates from the previous studies in Figure 3.12. The literature values range from −0.59 to +0.10 dex, whereas our [Fe/H] is -0.60 ± 0.18 dex. Our result is consistent with several literature values within the error margin, but is relatively lower than those of any previous study.

The closest estimate to our result is that of Neves et al. (2014). However, their method is a model-independent empirical one and uses optical wavelengths, so we do not find any important similarities with our method. They empirically determined [Fe/H] from the pseudo-EW of 4104 absorption lines in high-resolution optical spectra by the procedure calibrated by reference [Fe/H] values. The reference values were based on an empirical relation between M_{K_s}, $V-K_s$, and [Fe/H] calibrated by Neves et al. (2012) with 23 FGK+M binaries.

The results of five literatures using medium-resolution K-band spectra, namely Terrien et al. (2015), Man15, Gaidos et al. (2014), New14, and Rojas-Ayala et al. (2012), consistently cluster around −0.4. Terrien et al. (2015) compared the results from a limited number of these features in each spectral band of J, H, and K_s and found that the K_s-band estimates achieve the best precision, so the plot in Figure 3.12 is the result from K_s-band. Man15 and Gaidos et al. (2014) determine [Fe/H] from the 22 metallicity-sensitive features on medium-resolution visible/near-infrared spectra that were statistically identified by Mann et al. (2013a) using 112 FGK+M binary systems. Rojas-Ayala et al. (2012) determined [Fe/H] from EWs of metallicity-sensitive Na I and

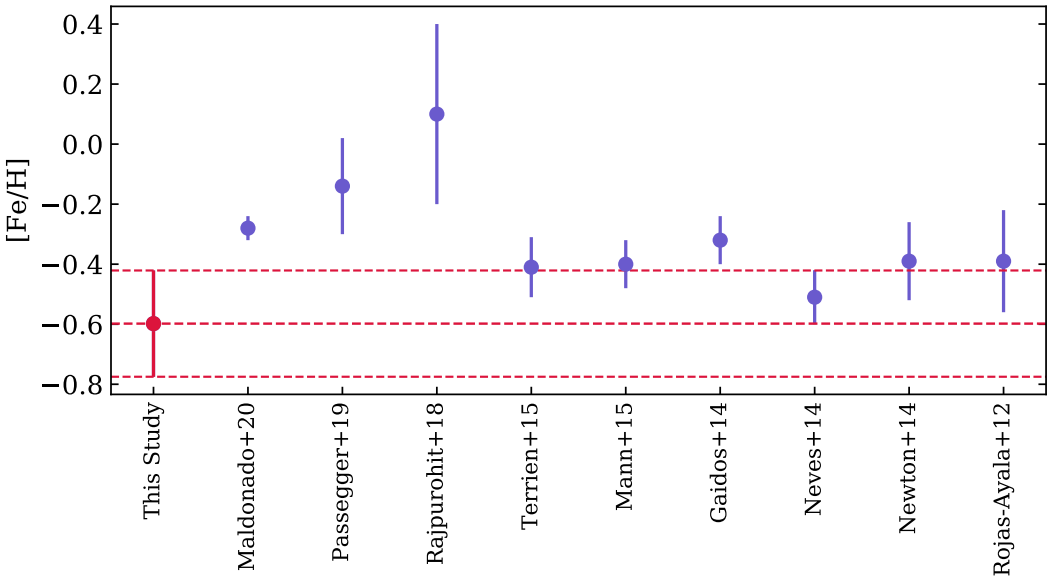

Figure 3.12: Comparison of the [Fe/H] of GJ 699 from our analysis with those from previous studies. The values in the literature are not the iron abundances determined directly from Fe lines. They refer to overall metallicities, except for that of Maldonado et al. (2020) who empirically determined abundances of iron using principal component analysis and sparse Bayesian method. The three horizontal dashed lines indicate the result of this study and its $1\sigma_{\mathrm{Total}}$ range.

Ca I lines and $T_{\rm eff}$-sensitive H_2O features in the medium-resolution K-band spectra. The aforementioned overestimation of New14 is not seen because the $T_{\rm eff}$ of GJ 699 is higher than those of the objects in Section 3.4.2 and among the $T_{\rm eff}$ range where their method is well calibrated.

Recent estimates by synthetic spectral fitting on high-resolution spectra show even higher results. Passegger et al. (2019) and Rajpurohit et al. (2018a) determined the metallicity and stellar parameters simultaneously by fitting the synthetic spectral grids of PHOENIX-SESAM and PHOENIX-BT-Settl, respectively, to the high-resolution optical and near-infrared spectra of CARMENES. They used the respectively selected spectral features of various elements all together to determine the overall metallicity. The features include a significant number of Ti I lines, that can potentially degrade the abundance determination as investigated in Section 2.5.2. In addition, the $T_{\rm eff}$ simultaneously estimated by the fitting in Rajpurohit et al. (2018a) (3400 K) is higher than that in other literature, including the $T_{\rm eff\text{-}TIC}$ (3259 K), and the χ^2 (= 2.43) of their fitting is significantly larger than those of most objects. It is thus possible that their fitting is not working well at least for this object for some reason such as its low metallicity.

Besides us, only Maldonado et al. (2020) considered the abundance of individual elements. They employed the principal component analysis and sparse Bayesian methods, using a sample of M dwarfs in binary systems with FGK primaries as a training dataset, to empirically determine the iron abundance from high-resolution optical spectra. However, their [Fe/H] are also significantly higher than ours. This suggests that the origin of the difference between our result and literature values is not the consideration of individual elemental abundances but instead due to differences in the wavelength ranges or the atmospheric models.

3.5 Discussion

3.5.1 Abundance distribution

Figures 3.13 and 3.14 show the distribution of the abundance ratios, relative to iron, of our M dwarfs compared with the FGK stars belonging to the individual kinematically separated stellar populations of the Galaxy. In these figures, the error bars of [X/Fe] are

calculated as the quadrature sum of $\sigma_{\rm SEM}$ values of [X/H] and [Fe/H]. The abundance ratios of FGK stars are adopted from Adi12 for Figure 3.13 and from Mishenina et al. (2019) for Figure 3.14.

Our M dwarfs generally have a distribution similar to that of the FGK stars, most of which belong to the thin disk population. We suppose that most of the program stars belong to the Galactic thin disk with two exceptions, GJ 699 and HD 154363B, both of which have similarities rather to the thick-disk FGK samples, especially in the low [Fe/H].

Several previous studies have suggested that GJ 699 (Barnard's star) belongs to the older populations with an age of ~7–12 Gyr based on observational properties such as a high space velocity, low metallicity, slow rotation ($P_{\rm rot} \sim 130.4$ d; Benedict et al. 1998), non-detection of lithium (Zuckerman & Song, 2004), low chromospheric activity (Rauscher & Marcy, 2006), and low X-ray luminosity ($\log L_{\rm X} = 26$; Hünsch et al. (1999)). Many literatures have indicated its belonging to the thick disk population and some (e.g., Choi et al., 2013) suggested that it is even a halo star. For such old stars, high [α/Fe] is expected. However, [Mg/Fe] and [Ca/Fe] of GJ 699 are lower than the typical value of the thick-disk FGK samples. There are, however, a fraction of thick disk stars that have [α/Fe] values as low as those of thin disk stars. Hence, the [Mg/Fe] and [Ca/Fe] do not exclude GJ 699 from the thick disk population. On the other hand, the abundance pattern of HD 154363B is more consistent with the thick-disk FGK samples in most elements.

For the [X/Fe] of the other 17 M dwarfs (5 form Chapter 2 and 12 from Chapter 3), the distribution is indeed similar to the thin-disk stars, but the absolute values are systematically lower than those of FGK stars. Although this discrepancy is within the error range for each object, the p-value of the Mann-Whitney U-test between the 17 M dwarfs and the thin-disk FGK stars is much smaller than 0.05, except for [Mn/Fe] and [Sr/Fe], which suggests the statistical significance of the differences. This difference appears to be existing only in the M dwarfs in this chapter rather than in Chapter 2, so they may be due to some systematic errors inherent in the stellar parameters in TIC or the low $T_{\rm eff}$.

In the following, we report what we can find about the distribution of individual elements. First, [Na/Fe] is generally constant, but shows an overall downward shift mentioned above. On the super-solar [Fe/H] side, it may reproduce the trend shown by

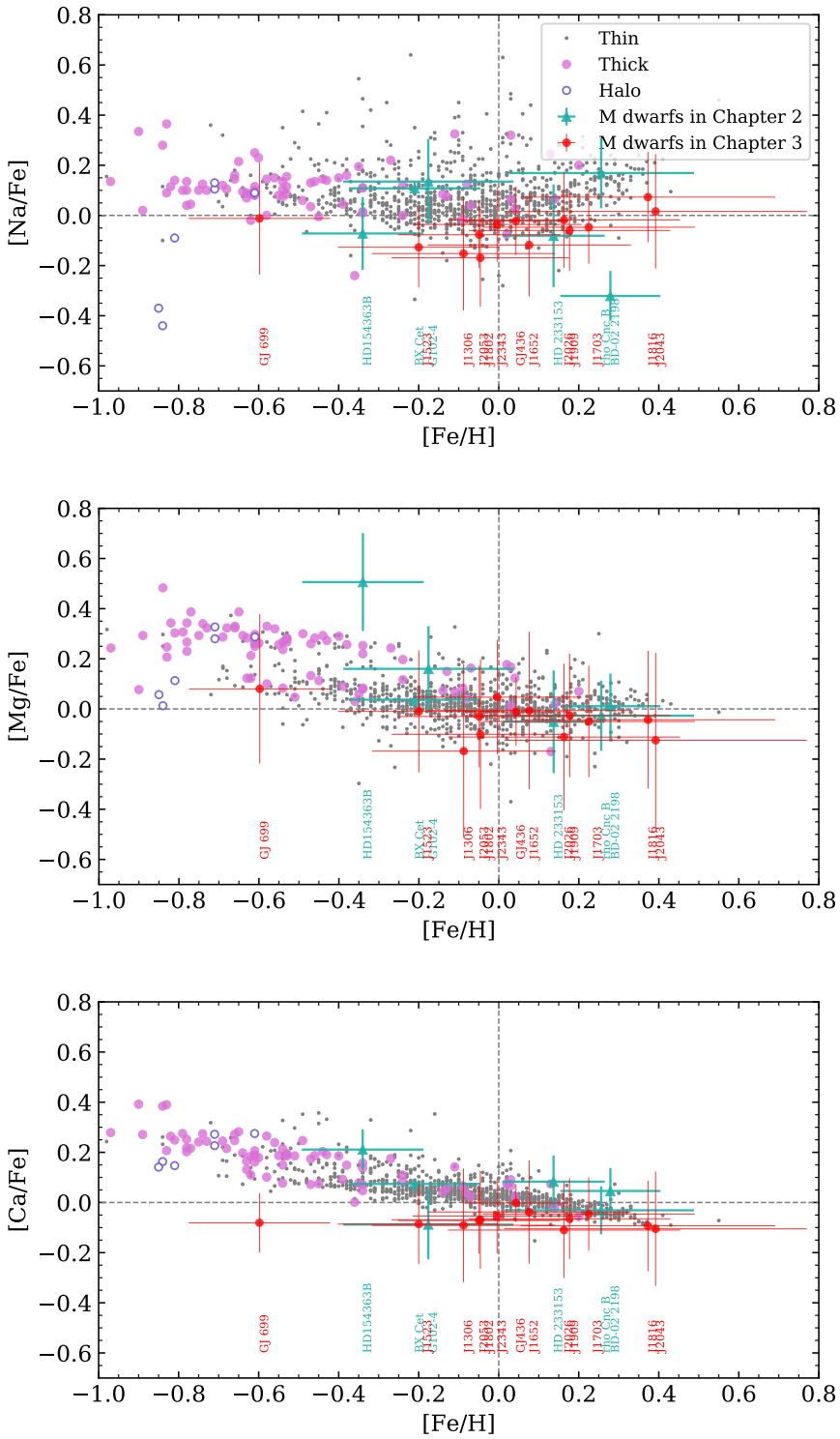

Figure 3.13: Iron-normalized abundances of six individual elements in the respective panels as a function of iron abundances. The red circles and green triangle are the M dwarfs we analyzed in Chapters 3 and 2, respectively. FGK stars analyzed by Adi12 are displayed as references showing the abundance trends of individual Galactic subpopulations. Among them, the gray dots, pink circles, and purple open circles are the thin disk stars, thick disk stars, and halo stars, respectively.

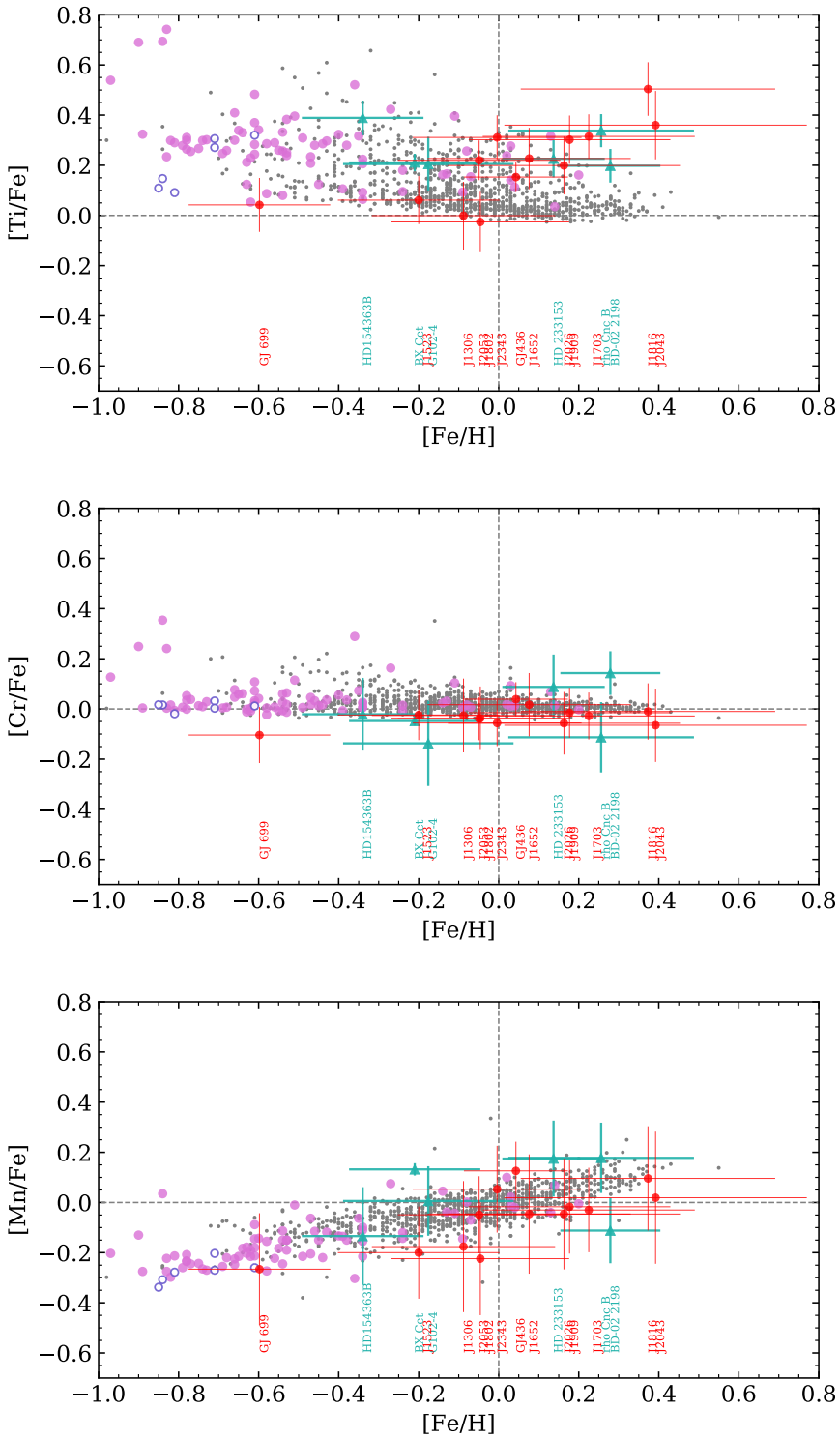

Figure 3.13: (Continued)

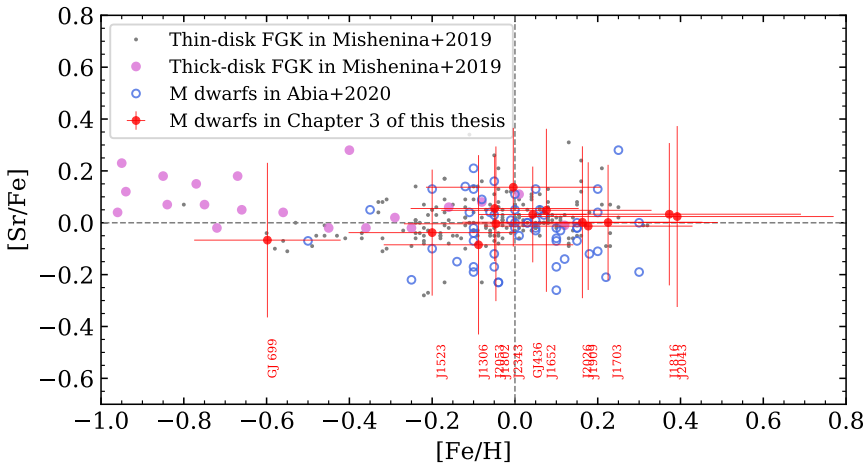

Figure 3.14: Iron-normalized abundances of Sr as a function of iron abundances. The red circles are the M dwarfs we analyzed in this Chapter. FGK stars from Mishenina et al. (2019) are displayed as references showing the abundance trends of the thin-disk stars (gray dots) and the thick-disk stars (pink circles). The blue open circles represent the nearby early M dwarfs in Abia et al. (2020).

the FGK samples where [Na/Fe] is higher as [Fe/H] is higher, but it is not significant. Similarly, [Mg/Fe] appears to exhibit a similar trend to the FGK samples, but is systematically lower. In [Ca/Fe], in addition to the overall downward shift similar to [Na/Fe], the M dwarfs in this chapter do not seem to reproduce the trend seen of FGK stars, where [Ca/Fe] rises gently with lower [Fe/H]. The [Ti/Fe] shows a large scatter and does not follow the trend of FGK stars. We suppose that it is due to analytical problems. However, the error bars on the vertical axis are small due to the large number of Ti I lines, since we adopted the quadrature sum of both σ_{SEM} values of [Fe/H] and [Ti/H]. The [Cr/Fe] is tightly aligned around the solar value as in the FGK samples. This is probably because both elements are iron peak elements, so the nature of the absorption lines is similar. The [Mn/Fe] is well within the increasing trend toward higher metallicities seen in the FGK samples. This trend is explained by the Type Ia supernovae enrichment (e.g., Nomoto et al., 2013). It is caused by the delayed enrichment by Type Ia supernovae because the Mn yield relative to Fe is higher for Type Ia supernovae than for Type II supernovae/hypernovae.

As the reference for the [Sr/Fe], we used FGK stars in Mishenina et al. (2019), as a

recent representative study, because Adi12 do not have Sr abundance values. We also plot the [Sr/Fe] results of Abia et al. (2020) for 57 nearby (within a few tens of parsecs) early-M dwarfs ($T_{\rm eff}$ > 3400 K) selected from the CARMENES-GTO targets. Figure 3.14 shows that the [Sr/Fe] ratios derived in our M dwarfs (red circles) agree well with those derived in the thin-disk FGK dwarfs (grey dots) and the early-M dwarfs (blue open circles). GJ 699 again shows a value that could be either of a thin- or a thick-disk star.

The general trends found in these abundance ratios could be not analytical artifacts but real trends in nearby M dwarfs, but we need to increase the precision or sample size to draw any conclusions. It is beyond the scope of this thesis to further discuss the trends in the precision finer than the estimated errors verified in Chapter 2.

3.5.2 Effect of $T_{\rm eff}$ shift

As mentioned in Section 3.3.2, there may still be systematic errors in the $T_{\rm eff\text{-}TIC}$ values below 3228K due to the scarcity of interferometric measurements. In the following, we will discuss this possibility and its impact on the abundance analysis.

As mentioned in Section 3.3.1, the HR diagram of our M dwarfs in Figure 3.3) suggests that either (1) the metallicities of all objects are lower than the solar value, or (2) $T_{\rm eff\ mathchar`-TIC}$ is overestimated, or both. The metallicity distribution of our results in Figure 3.10 does not support the possibility (1). If we consider (2) to be plausible, it is consistent with mitigating the possible difference between $T_{\rm eff\text{-}TIC}$ and $T_{\rm eff\text{-}interf}$ that might be implied in Figure 3.6.

To investigate the effect of overestimation of $T_{\rm eff\text{-}TIC}$ on the abundance analysis, we employed $T_{\rm eff}$ 100 K lower than $T_{\rm eff\text{-}TIC}$ to perform the same abundance analysis as in Section 3.3.3 as an experiment. The resulting metallicity distribution is shown in Figure 3.15. Both [Fe/H] and [$M_{\rm ave}$/H] dropped 0.11 dex on average, of which the distribution approached those of FGK stars to the extent that the Mann-Whitney U-test could not reject the null hypothesis of no difference.

The abundances of other elements [X/H] also decrease with a downward shift in $T_{\rm eff}$, as with Fe. The qualitative understanding is that if the $T_{\rm eff}$ adopted for the spectral synthesis decreases, the ionization degree of Na would decrease and make the EWs of Na I lines larger in the model, thus the result of [Na/H] reproducing the observed EW would result to be lower. In addition to the fact that the abundances of other elements

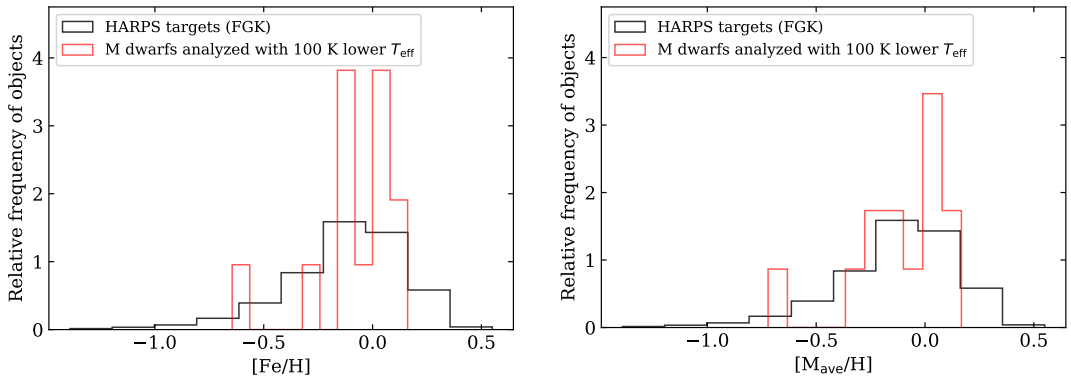

Figure 3.15: The same histograms as in Figure 3.10 but with 100K lower $T_{\rm eff}$ adopted in our analysis.

Table 3.6: Changes in abundance ratios when the temperature is lowered by 100 K

[Fe/H]	[Na/Fe]	[Mg/Fe]	[Ca/Fe]	[Ti/Fe]	[Cr/Fe]	[Mn/Fe]	[Sr/Fe]
−0.11	−0.05	−0.01	+0.03	−0.14	+0.01	−0.08	+0.09

These values are the average of the results for the 13 objects analyzed in this section.

also show similar behavior, the decrease in [Na/H] causes a general decrease in the abundances of all the other elements through the H^- opacity during the iterative process.

On the other hand, the abundance ratios [X/Fe] of individual elements relative to Fe show different changes depending on the ionization state of the elements and the characteristics of the used lines. Table 3.6 tabulates the variation of each abundance ratio with a 100 K decrease in $T_{\rm eff}$. If [X/H] changes as much as [Fe/H], [X/Fe] remains the same and 0.0 is reported in this table, but if [X/H] does not change as much as [Fe/H], it is positive in the table, and if it changes more than [Fe/H], it is negative. We find that these ratios do not necessarily move in the direction to match the distribution of nearby FGK stars. For example, the distribution of [Na/Fe], which has been generally lower than those of FGK as pointed out in Section 3.5.1, becomes even lower.

Thus, the overestimation of [Fe/H], which was implied in Sections 3.4.1 and 3.4.2, may be explained by the overestimation of $T_{\rm eff\text{-}TIC}$, but the difference in the abundance patterns of individual elements seen in Figure 3.13 from FGK stars is not. The shift of 100 K employed here is only for reference, and $T_{\rm eff}$ estimation by external methods

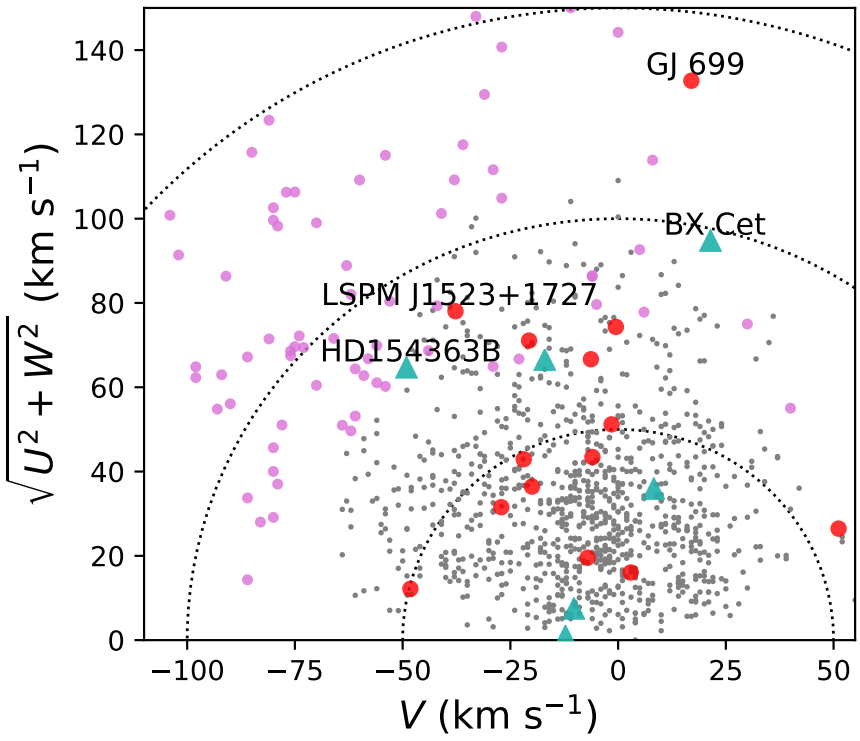

Figure 3.16: Toomre diagram of our M dwarfs and the FGK stars in Adi12. The types of marker are the same as in Figure 3.13. The Galactocentric space velocities U, V, and W are with respect to the LSR. Dotted lines represent constant values of the total space velocity $v_{\rm tot} = (U^2 + V^2 + W^2)^{1/2}$ in steps of 50 km s^{-1}.

such as interferometry is essential to understand the actual statistical error. It is highly desirable to clarify the systematic error of the $T_{\rm eff\text{-}TIC}$ in order to further improve the accuracy of the abundance analysis.

3.5.3 Kinematics

In Figure 3.16, we plot the Galactocentric space velocities of our M dwarfs calculated in Section 3.3.4 with those of FGK stars in Adi12 for comparison. Compared with Figure 3.13, we find that objects with lower [Fe/H] tend to have higher space velocities, which is consistent with the trend found for FGK stars.

We calculated the probabilities for each object belonging to either the thin disk

(D), thick disk (TD), or the halo (H) based on the kinematical criteria of Bensby et al. (2014) using the UVW. The criteria are based on the assumption that the individual populations have Gaussian velocity distributions, different rotation velocities around the Galactic center, and occupy certain fractions of the stars in the solar neighborhood. Then we selected thin disk stars as those with $TD/D < 0.5$ and thick disk stars as those with $TD/D > 2$. As a result, GJ 699 is likely to belong to the thick disk, HD 154363B and LSPM J1523+1727 are classified as "in-between stars" with equivalent chances of being the thin and thick disk, and the rest 16 objects belong to the thin disk. There were no halo stars with $H/TD > 1$. These are reasonable results considering the fact that ~90 % of the FGK stars in the solar vicinity are thin-disk stars and halo stars account for less than 1 % (e.g., Fuhrmann et al., 2017; de Jong et al., 2010).

3.5.4 Indication to chemical composition of planet-hosts

The sample of this study shows metallicity distribution in the range of about 1 dex. The differences over the range could have an impact on planet formation as suggested by many previous studies (e.g., Adibekyan, 2019).

The abundance ratios are similar to solar values in most of our target M dwarfs. Scaled solar abundances would be a useful approximation for them. However, there could be thick disk stars with high α/Fe ratios even in the solar neighborhood, which needs to be taken into account in the interpretation of the planets which will be found by the IRD-SSP.

This study also demonstrated that for M dwarfs, elemental abundances and kinetics can be used complementarily to distinguish stellar populations in the Galactic context. Future extension of these analyses to larger samples will reveal the distribution of stellar populations in nearby M dwarfs. Since it is difficult to determine the age of M dwarfs due to the slow changes of their properties (e.g., $T_{\rm eff}$ and luminosity) after reaching the main sequence, the chemical and kinematical information are the few valuable clues to understanding the formation age and environment of M dwarfs. This information of the formation history of M dwarfs directly connects to the formation and evolution of orbiting planets.

Combining the chemical composition of M dwarfs with the results of ongoing and future planet searches around M dwarfs will enable us to statistically explore

trends such as the planet–metallicity correlation, which provides the constraints on planet formation scenarios around M dwarfs. The difference in the occurrence rate of low-mass planets in different stellar populations indicated by Bashi et al. (2020) can also be assessed.

3.6 Summary

We determined the abundances of individual elements for the 13 nearby M dwarfs with $2900 < T_{\rm eff} < 3500$ K by the line-by-line EW analysis using the high-resolution (~70,000) near-infrared (970–1750 nm) spectra obtained in the IRD-SSP project. This is a pilot sample to understand the homogeneous chemical composition of nearby M dwarfs where the number of planet detection has been increasing. The IRD-SSP is a five-year project using the IRD spectrometer mounted on the Subaru Telescope to monitor the RV of 60 nearby mid-M to late-M dwarfs with a precision of 2 m s^{-1} to detect small and possibly habitable planets. We used the high-S/N IP-deconvolved telluric-removed spectra produced for the RV measurements in the project.

We determined the abundances of eight elements (Na, Mg, Ca, Ti, Cr, Mn, Fe, and Sr) for all 13 M dwarfs and those of three additional elements (Si, K, and V) for the hottest object GJ 436. The resulting metallicities, represented by [Fe/H] values, agree with the previous metallicity estimates by medium-resolution K-band spectra within the error margin. The error-weighted average metallicity $[M_{\rm ave}/H]$ of the M dwarfs range from ~ -0.6 to $\sim +0.4$ centered at around 0.0. For all the objects, the abundance ratios of individual elements with respect to Fe are generally aligned with the solar values within the measurement errors. An exception is a well-studied object GJ 699 (Barnard's star), which shows a small departure from the solar abundance ratios. Besides, our [Fe/H] of the object is lower than most of the previous estimates.

The abundance patterns of individual elements, namely the distribution of [X/Fe]s as a function of [Fe/H], are comparable to those of FGK stars in the solar neighborhood, most of which belong to the Galactic thin disk population. The wide distribution of metallicity, however, suggests a few of them could be thick disk stars.

We also measured the RVs from the high-resolution spectra of all the program stars, including those analyzed in Chapter 2. They are combined with the astrometric measurements from Gaia DR2 to calculate the space velocities UVW with respect to

the LSR. The Kinematics based on the UVW also suggests that a few of the M dwarfs studied in this thesis show similar features to FGK stars classified into the thick disk.

The wide distribution of metallicity could have an impact on planet formation around M dwarfs. Whereas scaled solar abundances were found for the 13 objects studied in this chapter, different abundance ratios could be found in a larger sample, given that the existence of thick disk stars is suggested by our results even in the solar vicinity. Abundance measurements of individual elements are required to determine the accurate metallicity of M dwarfs and to characterize their planets found by the IRD-SSP and other planet searches.

The quality of the abundance determination is limited by the uncertainty of $T_{\rm eff}$. We also tried to determine $T_{\rm eff}$ using the line strength of FeH molecules. The $T_{\rm eff\text{-}FeH}$ results in systematically higher values than the other empirical estimates based on photometry, especially at lower temperatures. Meanwhile, the $T_{\rm eff\text{-}FeH}$ shows a good correlation with the $T_{\rm eff\text{-}TIC}$, which is empirically calculated from $G_{\rm BP} - G_{\rm RP}$ color. Further interferometric measurements of angular diameters of such low-temperature M dwarfs are desired to improve the understanding of accurate $T_{\rm eff}$ values.

This study provides the first reliable elemental abundances of nearby 13 M dwarfs including the objects with $T_{\rm eff}$ less than 3200 K that have not been previously investigated. Their abundance patterns are shown to be comparable to those of FGK stars. We also show the possibility of locating M dwarfs on the Galactic chemical evolution based on the elemental abundance ratios and kinematics. They will be useful to characterize the planet-hosting M dwarfs and their planets identified by the current and future planet search projects.

The future extension of the analysis to all the targets of the IRD-SSP will lead to a further understanding of the abundance distribution of M dwarfs. It will also help to examine the relation between the chemical composition of M dwarfs and properties of the orbiting planets and constrain planet formation theories.

4 Conclusions and Outlook

4.1 Conclusions

We verified the analysis methods to obtain reliable abundances of individual elements for M dwarfs and applied them to a coherent sample of nearby M dwarfs. Especially for the objects with $T_{\rm eff} < 3200$ K, this is the first time that the elemental abundances have been directly determined from individual absorption lines. This study is a pioneering work to consistently determine the individual elemental abundances of M dwarfs.

M dwarfs are the most numerous constituents of the Galaxy and the major targets of recent planet search projects. The comprehensive and statistical measurements of their chemical composition will lead to the understanding of the relation between the planet formation and the nature of host stars, including their populations in the Galactic context.

Our main conclusions are as follows:

1. We found as a caveat specific to the low-temperature atmosphere that elements

with low ionization potentials, such as Na and Ca, have a significant effect on the abundance analysis of all the individual elements via the H^- continuous opacity. We also found that the strength of Ti I lines of M dwarfs with $T_{\rm eff} < 3400$ K are inversely correlated with the overall metallicity due to the TiO formation. These findings indicate the importance to analyze the individual elements not only those of interest in a consistent manner.

2. We verified the validity and precision of the abundance analysis of M dwarfs by confirming that the resulting elemental abundances of M dwarfs ($T_{\rm eff} \sim$ 3200–3800 K), which form binary systems with FGK primaries, agree with those of the primaries. The method is a line-by-line EW analysis based on high-resolution ($R \sim 80{,}000$) near-infrared (960–1710 nm) spectra and the typical uncertainty of resulting [X/H] is ∼0.2 dex.

3. We applied the analysis technique to determine the abundance ratios of eight elements (Na, Mg, Ca, Ti, Cr, Mn, Fe, and Sr) for 13 nearby M dwarfs (2900 $< T_{\rm eff} <$ 3500 K) among the IRD-SSP targets. The abundances of three additional elements (Si, K, and V) were also determined for the hottest one. The resulting metallicities range from approximately −0.6 to +0.4 and center at around 0.0. The [Fe/H] of individual objects agree with previous metallicity estimates from medium-resolution K-band spectra within the error margin.

4. The patterns of [X/Fe] for individual elements as functions of [Fe/H] are comparable to those of nearby FGK stars, most of which belong to the thin disk population. The wide distribution of metallicity, however, suggests a couple of them (e.g., GJ 699) could be thick disk stars and it is also supported by the Galactocentric space velocities UVW, which are calculated from our radial velocities and the astrometric measurements of Gaia. The existence of thick disk stars, which are expected to have a different abundance pattern than thin disk stars, makes the analysis of individual elemental abundances even more vital.

5. FeH molecular lines in Y-band are useful for estimating $T_{\rm eff}$ consistently from high-resolution spectra but they overestimate compared to the empirically calibrated $T_{\rm eff}$ based on colors. An increase in interferometric radius measurements is needed for the accurate calibration of the estimation.

4.2 Future prospects

This study has opened up the possibility of using high-resolution near-infrared spectra to homogeneously and consistently investigate the elemental abundances and stellar populations of nearby M dwarfs. In the near future, many planet search projects, including IRD-SSP, will increase the planet detection around M dwarfs. Since the metallicities of M dwarfs even in the solar neighborhood are distributed over almost 1 dex as shown in this study, combining them with the results of planet search projects will enable us to study the dependence of the occurrence rate or properties of the planets on the stellar metallicities and populations. The future extension to all the targets of IRD-SSP and other planet searches around M dwarfs will provide the detailed chemistry of the planet host candidates and lead to a further understanding of the abundance distribution of M dwarfs.

To do so, however, we still need to extend the validity of our abundance analysis method to lower temperatures. While we only dealt with M dwarfs hotter than 2900 K in this study, there are cooler objects even among the already known planet-hosts (e.g. $T_{\rm eff}$ of TRAPPIST-1 is estimated to be < 2600 K). At the lower temperature, the dust formation may begin to affect the spectra. Careful comparison and selection of atmospheric models and line data will be crucial. In the CARMENES GTO Data Archive, there are spectra of three late-M dwarfs ($T_{\rm eff}$ < 3200 K) which form binary systems with hotter M dwarfs. Besides, I obtained IRD spectra of such an object in my PI observations. I can use at least the four binary pairs for the verification of the abundance analysis of the cooler M dwarfs. The extension will allow us to discuss the stellar chemical composition in a wider $T_{\rm eff}$ range than ever before and its influence on planet formation.

Bibliography

Abia, C., Tabernero, H. M., Korotin, S. A., et al. 2020, A&A, 642, A227

Adibekyan, V. 2019, Geosciences, 9, 105

Adibekyan, V. Z., Sousa, S. G., Santos, N. C., et al. 2012a, A&A, 545, A32

Adibekyan, V. Z., Santos, N. C., Sousa, S. G., et al. 2012b, A&A, 543, A89

Allard, F., & Hauschildt, P. H. 1995, ApJ, 445, 433

Allard, F., Homeier, D., & Freytag, B. 2012, Philosophical Transactions of the Royal Society of London Series A, 370, 2765

—. 2013, Mem. Soc. Astron. Italiana, 84, 1053

Artigau, É., Kouach, D., Donati, J.-F., et al. 2014, in Proc. SPIE, Vol. 9147, Ground-based and Airborne Instrumentation for Astronomy V, 914715

Asplund, M., Grevesse, N., Sauval, A. J., & Scott, P. 2009, ARA&A, 47, 481

Barber, R. J., Tennyson, J., Harris, G. J., & Tolchenov, R. N. 2006, MNRAS, 368, 1087

Barclay, T., Pepper, J., & Quintana, E. V. 2018, ApJS, 239, 2

Barklem, P. S., Piskunov, N., & O'Mara, B. J. 2000, A&AS, 142, 467

Bashi, D., Zucker, S., Adibekyan, V., et al. 2020, A&A, 643, A106

Bean, J. L., Sneden, C., Hauschildt, P. H., Johns-Krull, C. M., & Benedict, G. F. 2006, ApJ, 652, 1604

Benedict, G. F., McArthur, B., Nelan, E., et al. 1998, AJ, 116, 429

Bensby, T., Feltzing, S., & Oey, M. S. 2014, A&A, 562, A71

Birky, J., Hogg, D. W., Mann, A. W., & Burgasser, A. 2020, ApJ, 892, 31

Bitsch, B., & Battistini, C. 2020, A&A, 633, A10

Blackwell-Whitehead, R., Pavlenko, Y. V., Nave, G., et al. 2011, A&A, 525, A44

Bochanski, J. J., Hawley, S. L., Covey, K. R., et al. 2010, AJ, 139, 2679

Bonfils, X., Delfosse, X., Udry, S., et al. 2005, A&A, 442, 635

Bressan, A., Marigo, P., Girardi, L., et al. 2012, MNRAS, 427, 127

Brugamyer, E., Dodson-Robinson, S. E., Cochran, W. D., & Sneden, C. 2011, ApJ, 738, 97

Caballero, J. A., Guàrdia, J., López del Fresno, M., et al. 2016, in Proc. SPIE, Vol. 9910, Observatory Operations: Strategies, Processes, and Systems VI, 99100E

Chen, Y., Girardi, L., Bressan, A., et al. 2014, MNRAS, 444, 2525

Choi, J., McCarthy, C., Marcy, G. W., et al. 2013, ApJ, 764, 131

Clough, S. A., Iacono, M. J., & Moncet, J.-L. 1992, J. Geophys. Res., 97, 15,761

Clough, S. A., Shephard, M. W., Mlawer, E. J., et al. 2005, J. Quant. Spec. Radiat. Transf., 91, 233

de Jong, J. T. A., Yanny, B., Rix, H.-W., et al. 2010, ApJ, 714, 663

Delfosse, X., Forveille, T., Ségransan, D., et al. 2000, A&A, 364, 217

Delrez, L., Gillon, M., Queloz, D., et al. 2018, in Society of Photo-Optical Instrumentation Engineers (SPIE) Conference Series, Vol. 10700, Proc. SPIE, 107001I

Desidera, S., Gratton, R. G., Lucatello, S., & Claudi, R. U. 2006, A&A, 454, 581

Desidera, S., Gratton, R. G., Scuderi, S., et al. 2004, A&A, 420, 683

Dorn, C., Venturini, J., Khan, A., et al. 2017, A&A, 597, A37

Fischer, D. A., & Valenti, J. 2005, ApJ, 622, 1102

Fortney, J. J., Mordasini, C., Nettelmann, N., et al. 2013, ApJ, 775, 80

Fuhrmann, K., Chini, R., Kaderhandt, L., & Chen, Z. 2017, MNRAS, 464, 2610

Gaia Collaboration, Brown, A. G. A., Vallenari, A., et al. 2018, A&A, 616, A1

Gaidos, E., Mann, A. W., Lépine, S., et al. 2014, MNRAS, 443, 2561

Gan, T., Shporer, A., Livingston, J. H., et al. 2020, AJ, 159, 160

Gardner, J. P., Mather, J. C., Clampin, M., et al. 2006, Space Sci. Rev., 123, 485

Gray, D. F. 2005, The Observation and Analysis of Stellar Photospheres

Gustafsson, B., Edvardsson, B., Eriksson, K., et al. 2008, A&A, 486, 951

Hauschildt, P. H., Allard, F., & Baron, E. 1999, ApJ, 512, 377

Hawkins, K., Lucey, M., Ting, Y.-S., et al. 2020, MNRAS, 492, 1164

Hejazi, N., Lépine, S., Homeier, D., Rich, R. M., & Shara, M. M. 2020, AJ, 159, 30

Henry, T. J., Kirkpatrick, J. D., & Simons, D. A. 1994, AJ, 108, 1437

Hirano, T., Kuzuhara, M., Kotani, T., et al. 2020, PASJ, 72, 93

Hobson, M. J., Jofré, E., García, L., Petrucci, R., & Gómez, M. 2018, Revista Mexicana de Astronomía y Astrofísica, 54, 65

Holtzman, J. A., Shetrone, M., Johnson, J. A., et al. 2015, AJ, 150, 148

Howell, S. B., Sobeck, C., Haas, M., et al. 2014, PASP, 126, 398

Hünsch, M., Schmitt, J. H. M. M., Sterzik, M. F., & Voges, W. 1999, A&AS, 135, 319

Husser, T. O., Wende-von Berg, S., Dreizler, S., et al. 2013, A&A, 553, A6

Irwin, J. M., Berta-Thompson, Z. K., Charbonneau, D., et al. 2015, in Cambridge Workshop on Cool Stars, Stellar Systems, and the Sun, Vol. 18, 18th Cambridge Workshop on Cool Stars, Stellar Systems, and the Sun, ed. G. T. van Belle & H. C. Harris, 767–772

Ishikawa, H. T., Aoki, W., Kotani, T., et al. 2020, PASJ, 72, 102

Jeffers, S. V., Schöfer, P., Lamert, A., et al. 2018, A&A, 614, A76

Jofré, P., Heiter, U., & Soubiran, C. 2019, ARA&A, 57, 571

Johnson, J. A., Gazak, J. Z., Apps, K., et al. 2012, AJ, 143, 111

Jurić, M., Ivezić, Ž., Brooks, A., et al. 2008, ApJ, 673, 864

Kaeufl, H.-U., Ballester, P., Biereichel, P., et al. 2004, in Proc. SPIE, Vol. 5492, Ground-based Instrumentation for Astronomy, ed. A. F. M. Moorwood & M. Iye, 1218–1227

Kotani, T., Tamura, M., Suto, H., et al. 2014, in Proc. SPIE, Vol. 9147, Ground-based and Airborne Instrumentation for Astronomy V, 914714

Kotani, T., Tamura, M., Nishikawa, J., et al. 2018, in Society of Photo-Optical Instrumentation Engineers (SPIE) Conference Series, Vol. 10702, Proc. SPIE, 1070211

Kupka, F., Piskunov, N., Ryabchikova, T. A., Stempels, H. C., & Weiss, W. W. 1999, A&AS, 138, 119

Lindgren, S., & Heiter, U. 2017, A&A, 604, A97

Lindgren, S., Heiter, U., & Seifahrt, A. 2016, A&A, 586, A100

Luck, R. E. 2017, AJ, 153, 21

Madhusudhan, N. 2019, ARA&A, 57, 617

Mahadevan, S., Ramsey, L., Bender, C., et al. 2012, in Proc. SPIE, Vol. 8446, Ground-based and Airborne Instrumentation for Astronomy IV, 84461S

Majewski, S. R., Schiavon, R. P., Frinchaboy, P. M., et al. 2017, AJ, 154, 94

Maldonado, J., Micela, G., Baratella, M., et al. 2020, A&A, 644, A68

Mann, A. W., Brewer, J. M., Gaidos, E., Lépine, S., & Hilton, E. J. 2013a, AJ, 145, 52

Mann, A. W., Deacon, N. R., Gaidos, E., et al. 2014, AJ, 147, 160

Mann, A. W., Feiden, G. A., Gaidos, E., Boyajian, T., & von Braun, K. 2015, ApJ, 804, 64

Mann, A. W., Gaidos, E., & Ansdell, M. 2013b, ApJ, 779, 188

Mann, A. W., Dupuy, T., Kraus, A. L., et al. 2019, ApJ, 871, 63

Mayor, M., Pepe, F., Queloz, D., et al. 2003, The Messenger, 114, 20

McKemmish, L. K., Masseron, T., Hoeijmakers, H. J., et al. 2019, MNRAS, 488, 2836

McMillan, P. J. 2017, MNRAS, 465, 76

Mishenina, T., Pignatari, M., Gorbaneva, T., et al. 2019, MNRAS, 484, 3846

Monet, D. G., Levine, S. E., Canzian, B., et al. 2003, AJ, 125, 984

Montes, D., González-Peinado, R., Tabernero, H. M., et al. 2018, MNRAS, 479, 1332

Mould, J. R. 1976, ApJ, 210, 402

Neves, V., Bonfils, X., Santos, N. C., et al. 2013, A&A, 551, A36

—. 2014, A&A, 568, A121

—. 2012, A&A, 538, A25

Newton, E. R., Charbonneau, D., Irwin, J., et al. 2014, AJ, 147, 20

Newton, E. R., Charbonneau, D., Irwin, J., & Mann, A. W. 2015, ApJ, 800, 85

Nissen, P. E., & Gustafsson, B. 2018, A&A Rev., 26, 6

Nomoto, K., Kobayashi, C., & Tominaga, N. 2013, ARA&A, 51, 457

Olander, T., Heiter, U., & Kochukhov, O. 2021, arXiv e-prints, arXiv:2102.08836

Önehag, A., Heiter, U., Gustafsson, B., et al. 2012, A&A, 542, A33

Passegger, V. M., Schweitzer, A., Shulyak, D., et al. 2019, A&A, 627, A161

Poveda, A., Allen, C., Costero, R., Echevarría, J., & Hernández-Alcántara, A. 2009, ApJ, 706, 343

Quirrenbach, A., Amado, P. J., Caballero, J. A., et al. 2014, in Society of Photo-Optical Instrumentation Engineers (SPIE) Conference Series, Vol. 9147, Ground-based and Airborne Instrumentation for Astronomy V, ed. S. K. Ramsay, I. S. McLean, & H. Takami, 91471F

Rabus, M., Lachaume, R., Jordán, A., et al. 2019, MNRAS, 484, 2674

Rajpurohit, A. S., Allard, F., Rajpurohit, S., et al. 2018a, A&A, 620, A180

Rajpurohit, A. S., Allard, F., Teixeira, G. D. C., et al. 2018b, A&A, 610, A19

Rauscher, E., & Marcy, G. W. 2006, PASP, 118, 617

Reddy, B. E., Lambert, D. L., & Allende Prieto, C. 2006, MNRAS, 367, 1329

Reiners, A., Zechmeister, M., Caballero, J. A., et al. 2018, A&A, 612, A49

Ribas, I., Tuomi, M., Reiners, A., et al. 2018, Nature, 563, 365

Ricker, G. R., Winn, J. N., Vanderspek, R., et al. 2015, Journal of Astronomical Telescopes, Instruments, and Systems, 1, 014003

Rojas-Ayala, B., Covey, K. R., Muirhead, P. S., & Lloyd, J. P. 2012, ApJ, 748, 93

Ryabchikova, T., Piskunov, N., Kurucz, R. L., et al. 2015, Phys. Scr, 90, 054005

Ryan, S. G. 1998, A&A, 331, 1051

Santos, N. C., Israelian, G., & Mayor, M. 2004, A&A, 415, 1153

Sato, B., Ohashi, N., Akiyama, E., et al. 2018, Search for Planets like Earth around Late-M Dwarfs: Precise Radial Velocity Survey with IRD (Available at: https://www.naoj.org/Science/SACM/Senryaku/IRD_180520235849.pdf)

Schönrich, R., Binney, J., & Dehnen, W. 2010, MNRAS, 403, 1829

Schweitzer, A., Passegger, V. M., Cifuentes, C., et al. 2019, A&A, 625, A68

Shields, A. L., Ballard, S., & Johnson, J. A. 2016, Phys. Rep., 663, 1

Skrutskie, M. F., Cutri, R. M., Stiening, R., et al. 2006, AJ, 131, 1163

Souto, D., Cunha, K., García-Hernández, D. A., et al. 2017, ApJ, 835, 239

Souto, D., Unterborn, C. T., Smith, V. V., et al. 2018, ApJ, 860, L15

Souto, D., Cunha, K., Smith, V. V., et al. 2020, ApJ, 890, 133

Sozzetti, A., Bernagozzi, A., Bertolini, E., et al. 2013, in European Physical Journal Web of Conferences, Vol. 47, European Physical Journal Web of Conferences, 03006

Stassun, K. G., Oelkers, R. J., Paegert, M., et al. 2019, AJ, 158, 138

Terrien, R. C., Mahadevan, S., Deshpande, R., & Bender, C. F. 2015, ApJS, 220, 16

Thiabaud, A., Marboeuf, U., Alibert, Y., et al. 2014, A&A, 562, A27

Tsuji, T. 1973, A&A, 23, 411

—. 1978, A&A, 62, 29

—. 2016, PASJ, 68, 84

Tsuji, T., & Nakajima, T. 2014, PASJ, 66, 98

—. 2016, PASJ, 68, 13

Tsuji, T., Nakajima, T., & Takeda, Y. 2015, PASJ, 67, 26

Tsuji, T., Ohnaka, K., & Aoki, W. 1996, A&A, 305, L1

Unsöld, A. 1955, Physik der Sternatmospharen, MIT besonderer Berucksichtigung der Sonne. (Springer-Verlag, Berlin)

Unterborn, C. T., & Panero, W. R. 2017, ApJ, 845, 61

Valenti, J. A., Piskunov, N., & Johns-Krull, C. M. 1998, ApJ, 498, 851

Veyette, M. J., & Muirhead, P. S. 2018, ApJ, 863, 166

Veyette, M. J., Muirhead, P. S., Mann, A. W., & Allard, F. 2016, ApJ, 828, 95

Veyette, M. J., Muirhead, P. S., Mann, A. W., et al. 2017, ApJ, 851, 26

Weidemann, V. 1955, ZAp, 36, 101

Welbanks, L., Madhusudhan, N., Allard, N. F., et al. 2019, ApJ, 887, L20

Wende, S., Reiners, A., & Ludwig, H. G. 2009, A&A, 508, 1429

West, A. A., Morgan, D. P., Bochanski, J. J., et al. 2011, AJ, 141, 97

Wing, R. F., & Ford, W. Kent, J. 1969, PASP, 81, 527

Woolf, V. M., & Wallerstein, G. 2005, MNRAS, 356, 963

—. 2020, MNRAS, 494, 2718

Zboril, M., & Byrne, P. B. 1998, MNRAS, 299, 753

Zechmeister, M., Anglada-Escudé, G., & Reiners, A. 2014, A&A, 561, A59

Zuckerman, B., & Song, I. 2004, ARA&A, 42, 685

A

IRD spectral atlas

In Figures A.1–A.16, we plot the continuum-normalized IRD spectra of GJ 436 ($T_{\text{eff-TIC}}$ = 3456 K) by purple solid lines, GJ 699 ($T_{\text{eff-TIC}}$ = 3259 K) by green dot-dashed lines, and LSPM J1306+3050 ($T_{\text{eff-TIC}}$ = 2970 K) by red dashed lines. The horizontal axis is the vacuum wavelength in the stellar rest frame written in Å.

Prominent absorption lines are marked based on the VALD database and the line list by Plez. Since the Wing-Ford band at ~9900–10200 Å has a high density of FeH lines, only the 57 lines used for T_{eff} estimation are marked and highlighted for clarity. The atomic lines used for the abundance analysis in Chapter 3 are also highlighted in color.

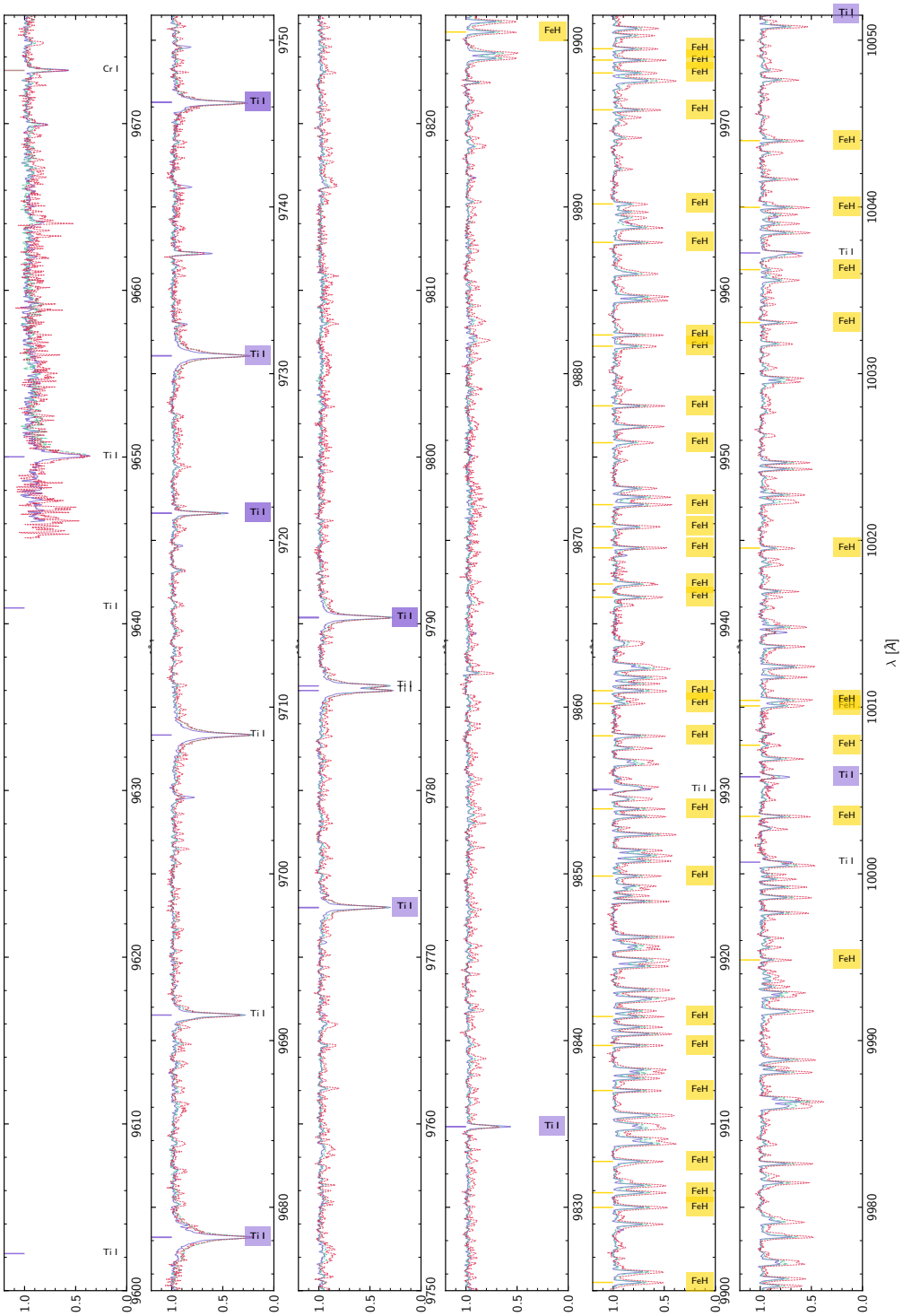

Figure A.1: IRD spectral atlas

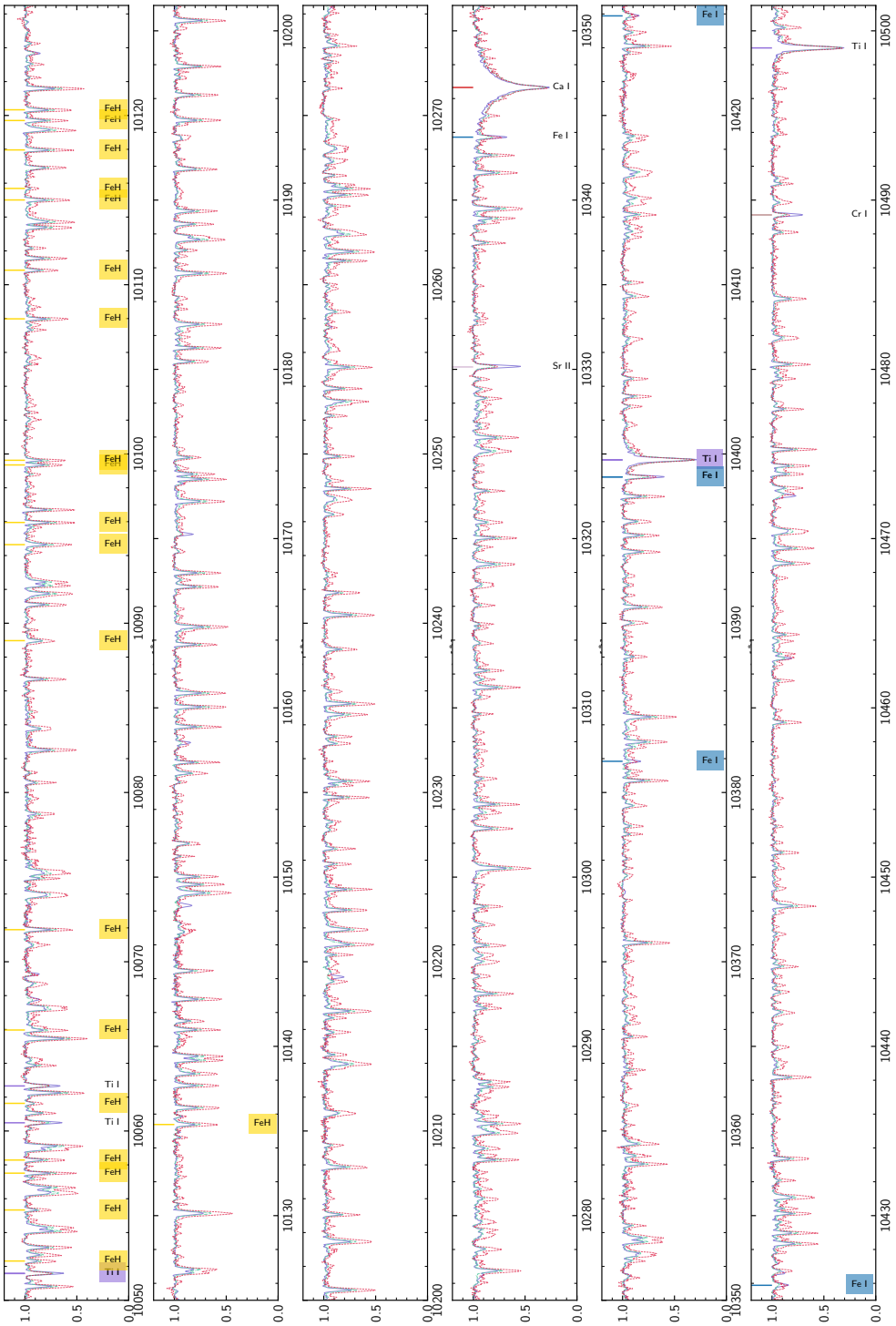

Figure A.2: IRD spectral atlas (Continued)

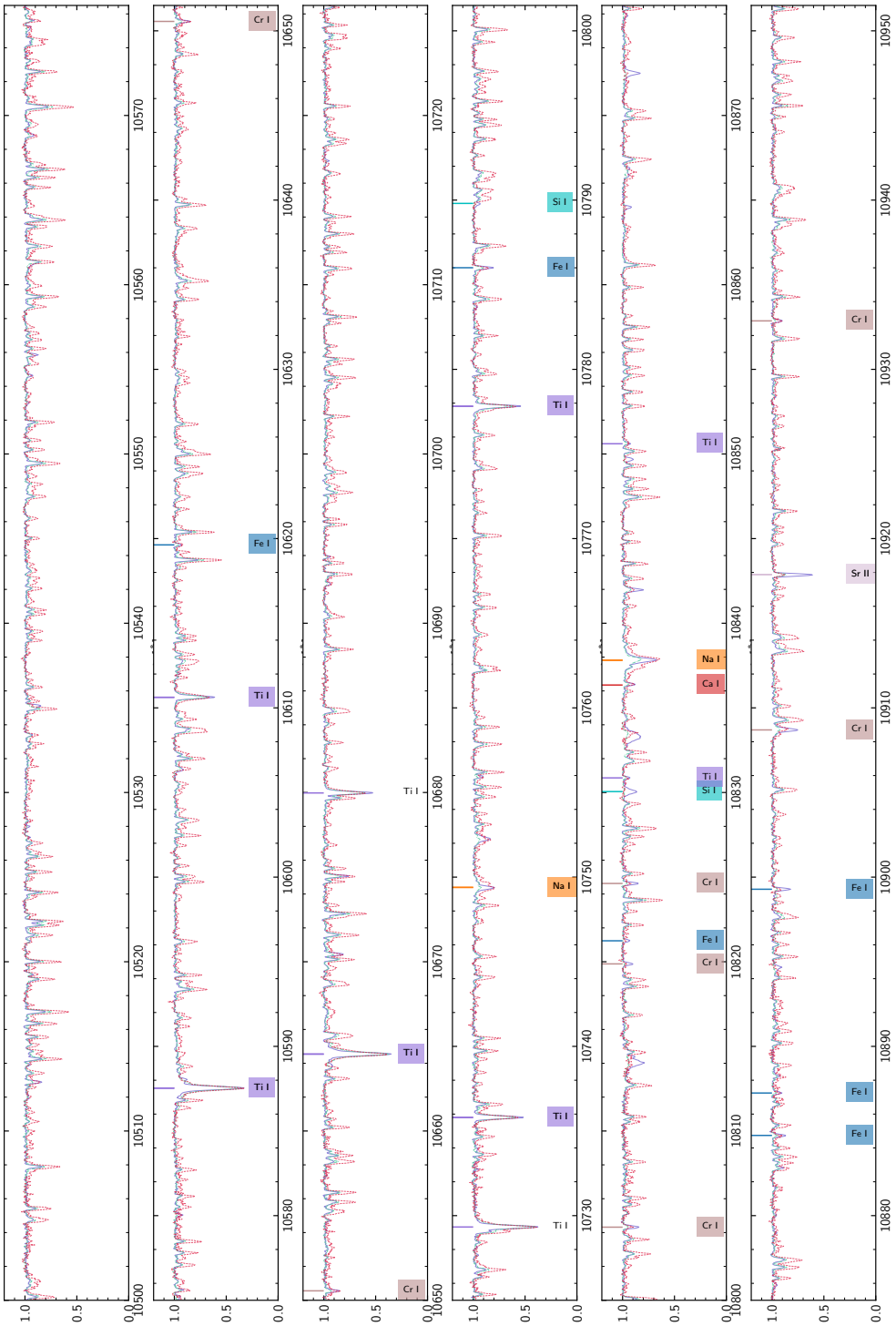

Figure A.3: IRD spectral atlas (Continued)

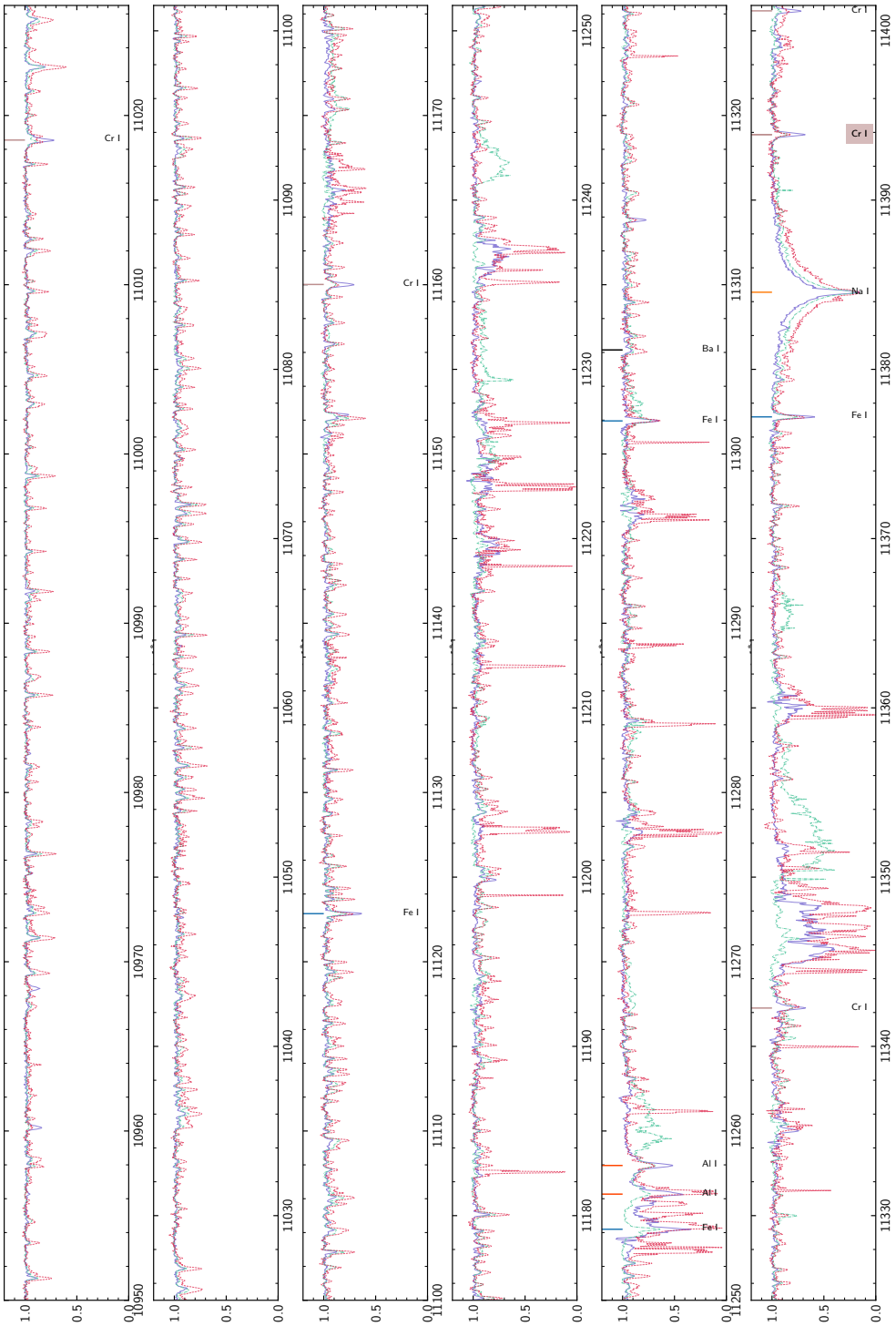

Figure A.4: IRD spectral atlas (Continued)

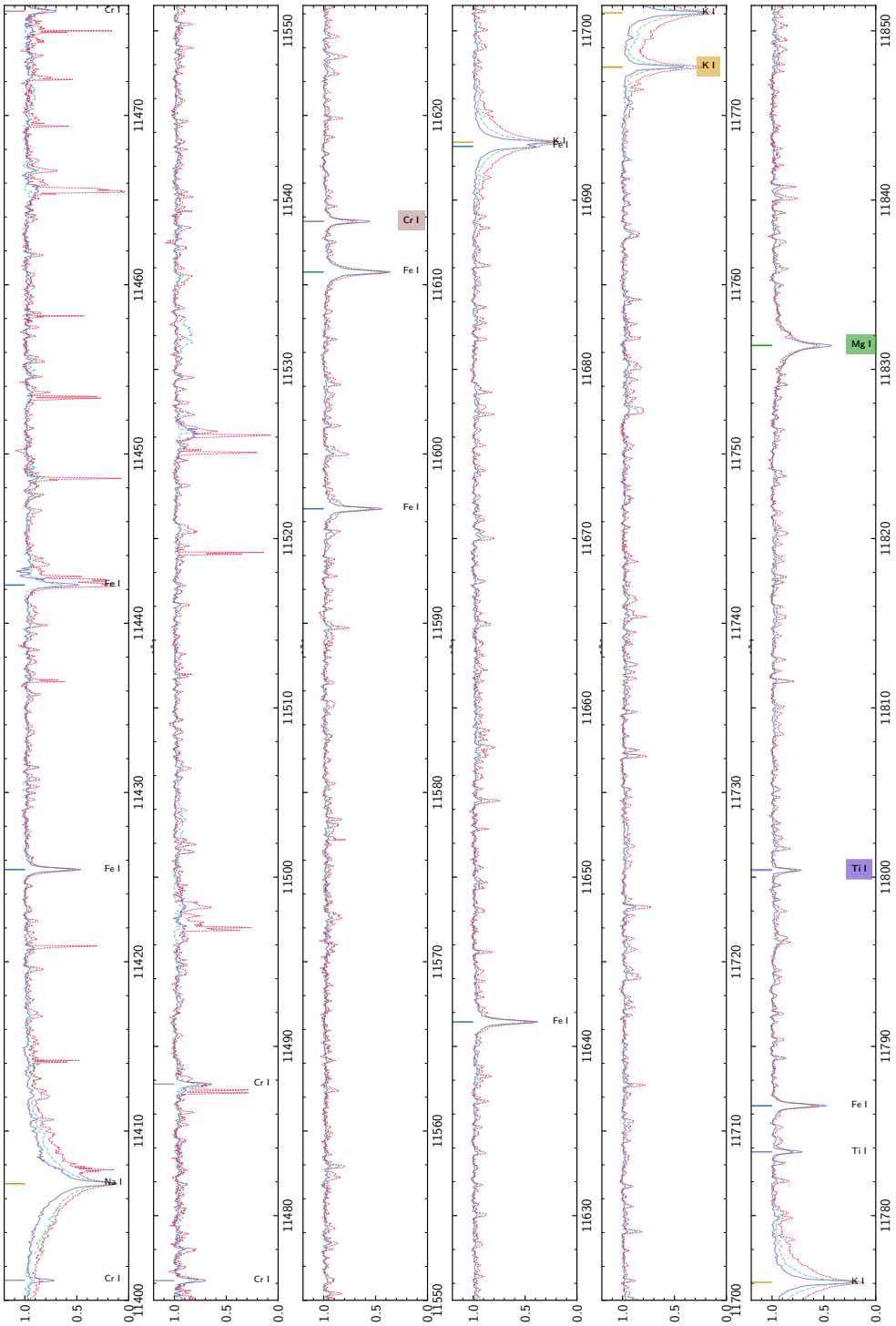

Figure A.5: IRD spectral atlas (Continued)

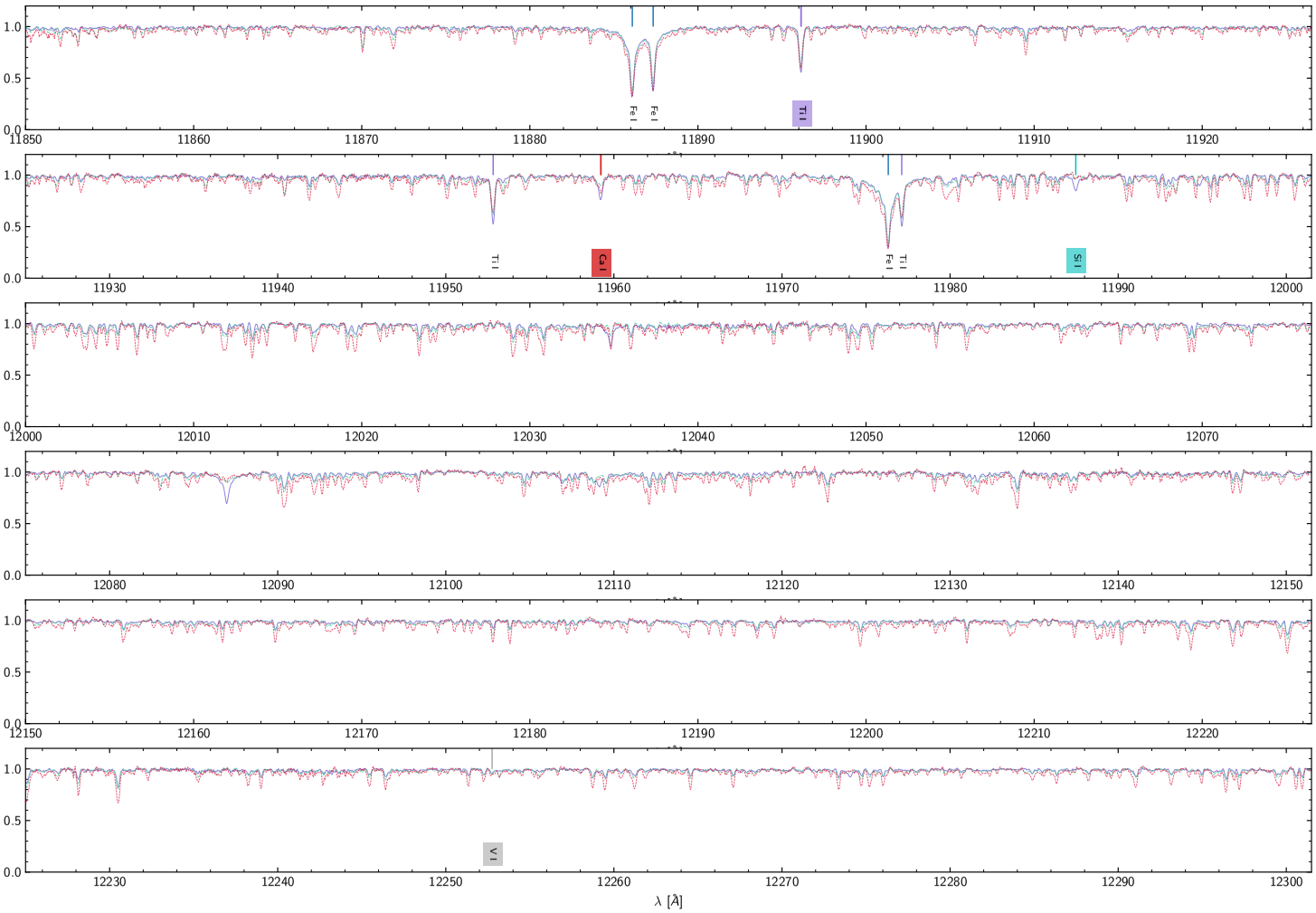

Figure A.6: IRD spectral atlas (Continued)

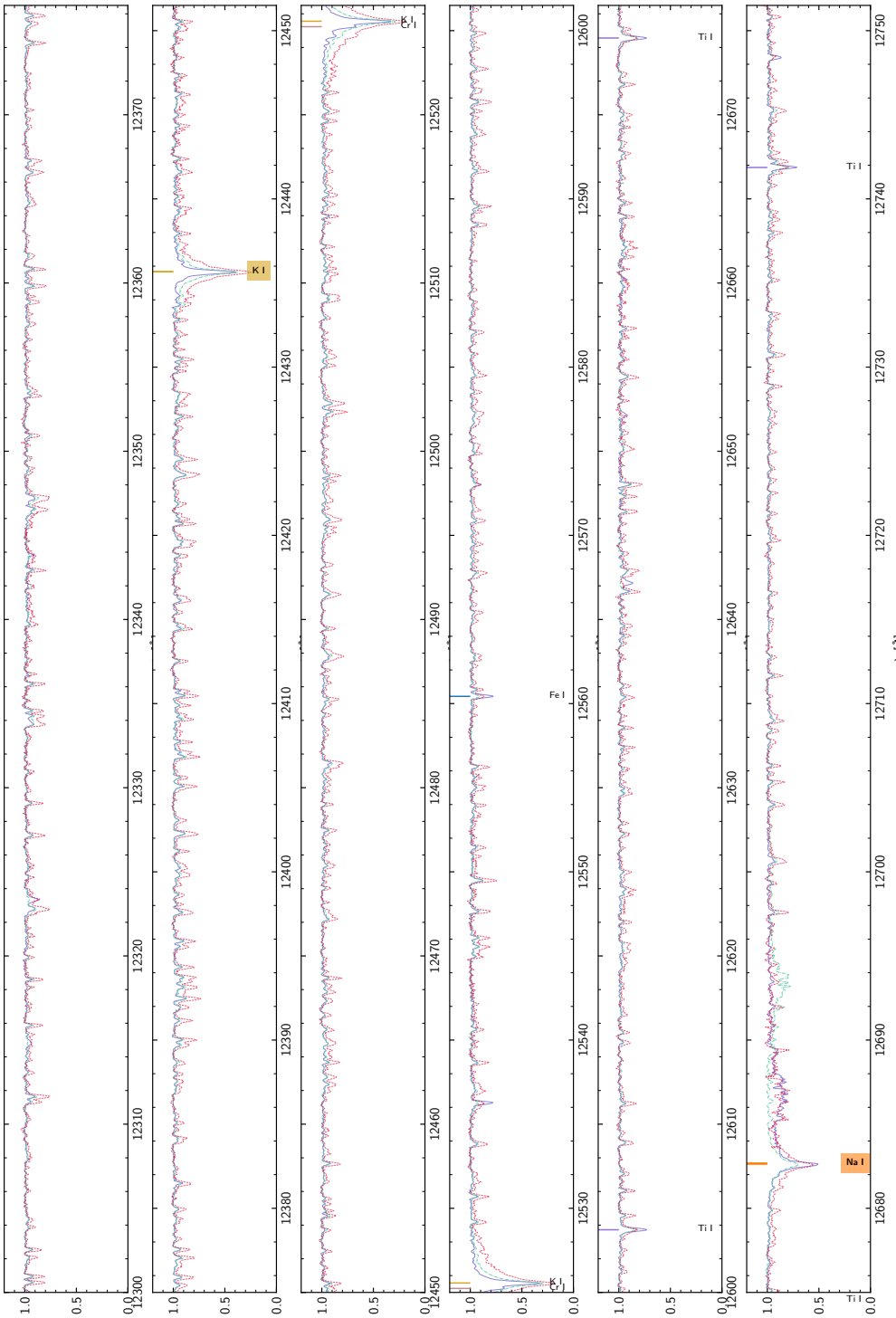

Figure A.7: IRD spectral atlas (Continued)

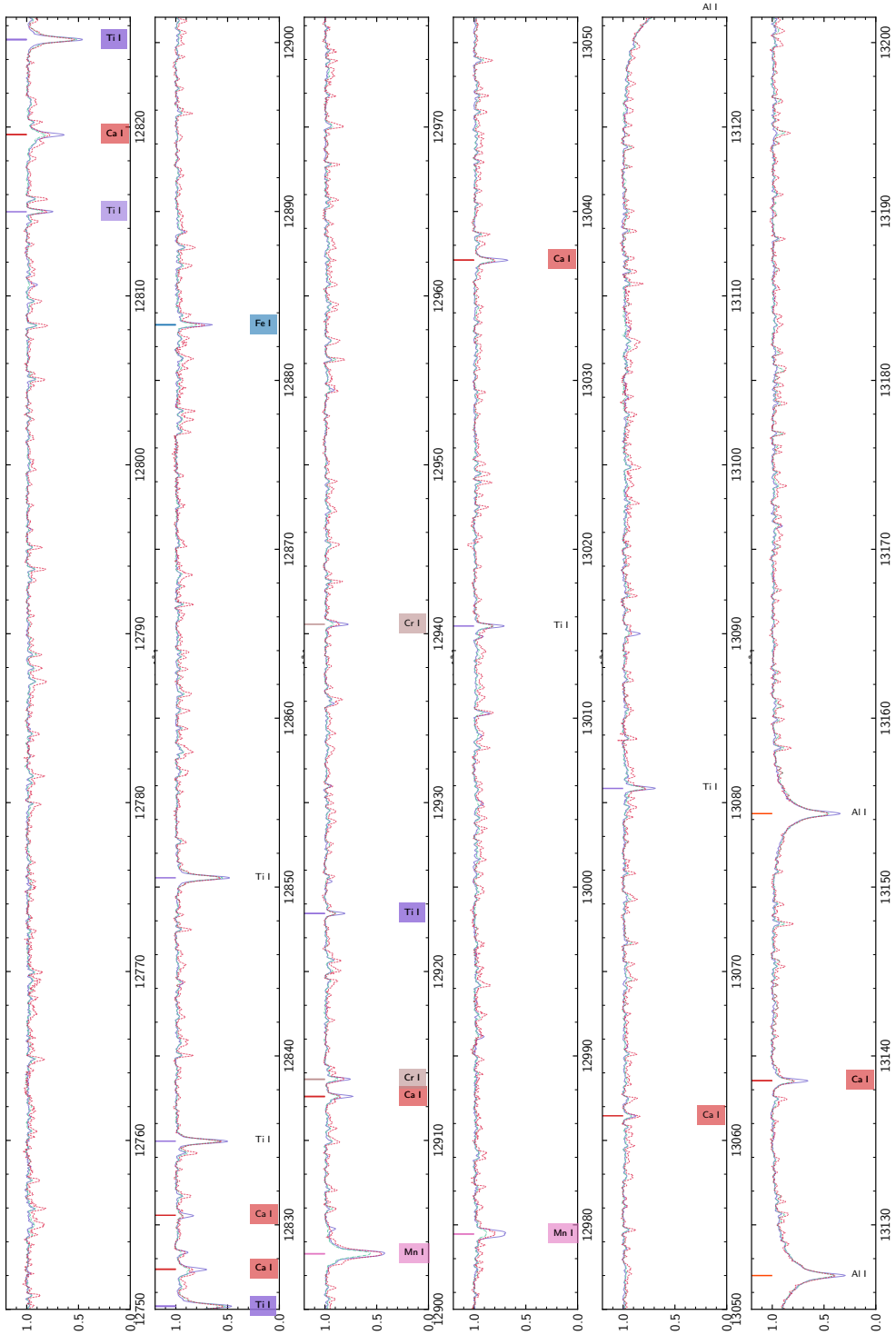

Figure A.8: IRD spectral atlas (Continued)

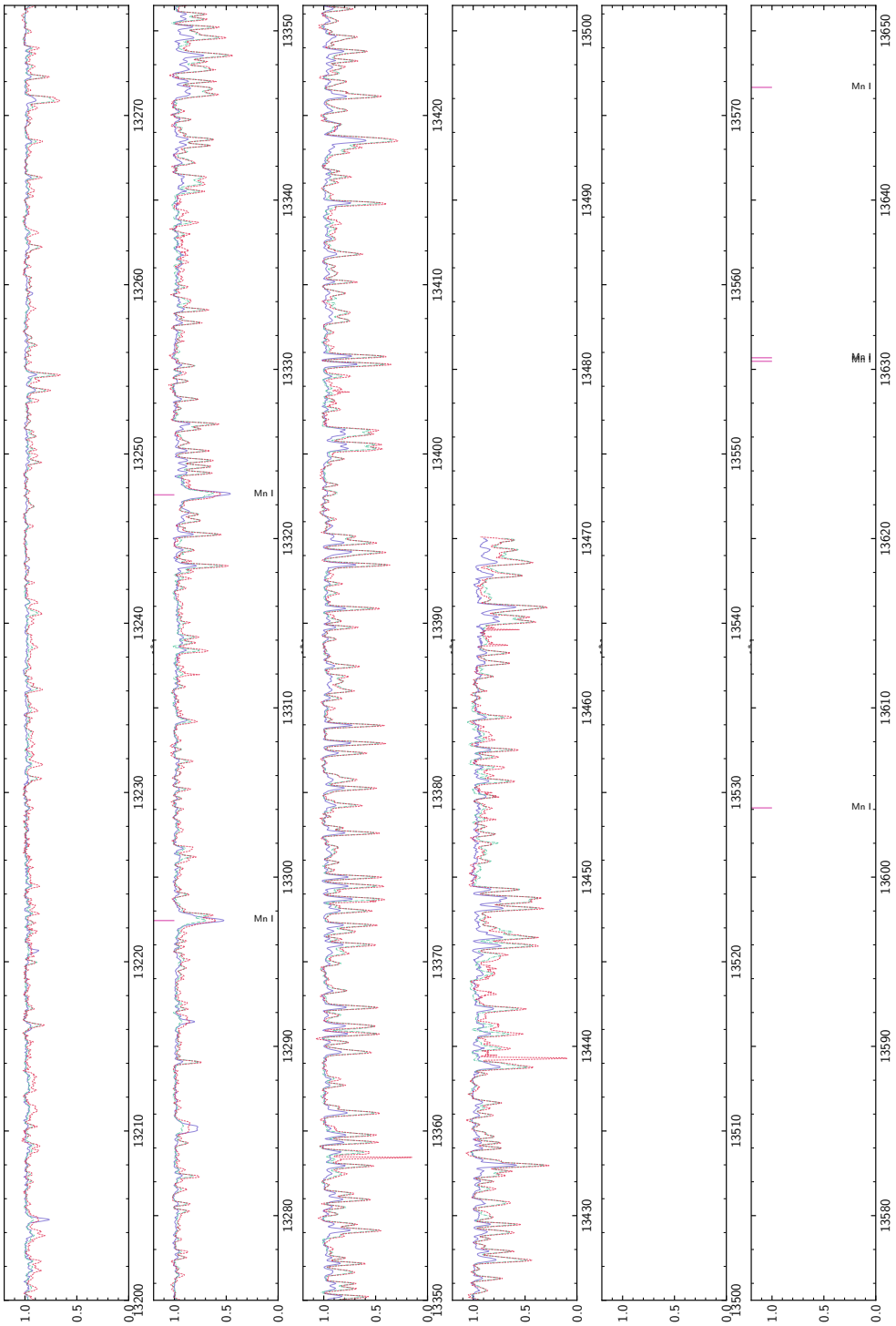

Figure A.9: IRD spectral atlas (Continued)

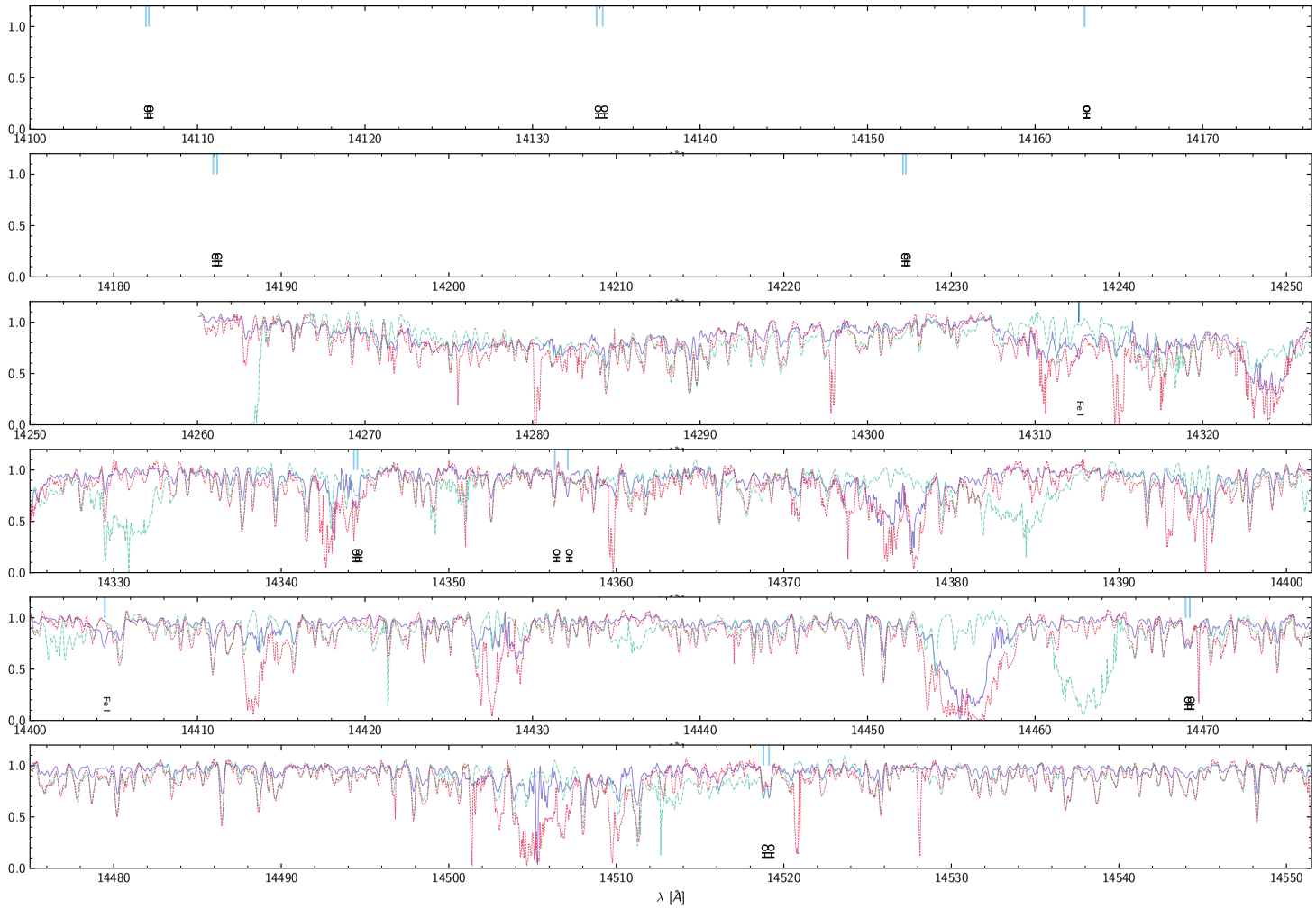

Figure A.10: IRD spectral atlas (Continued)

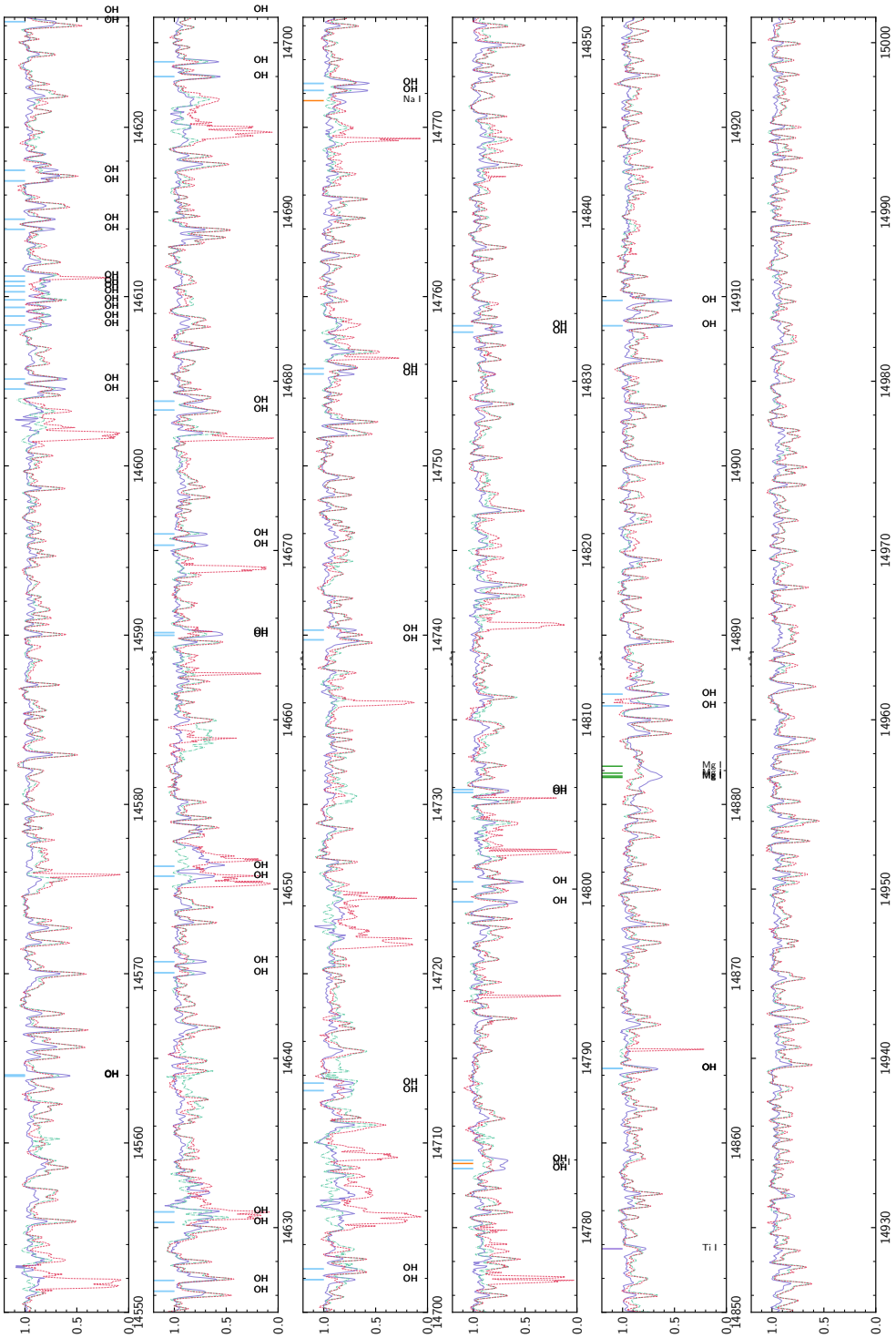

Figure A.11: IRD spectral atlas (Continued)

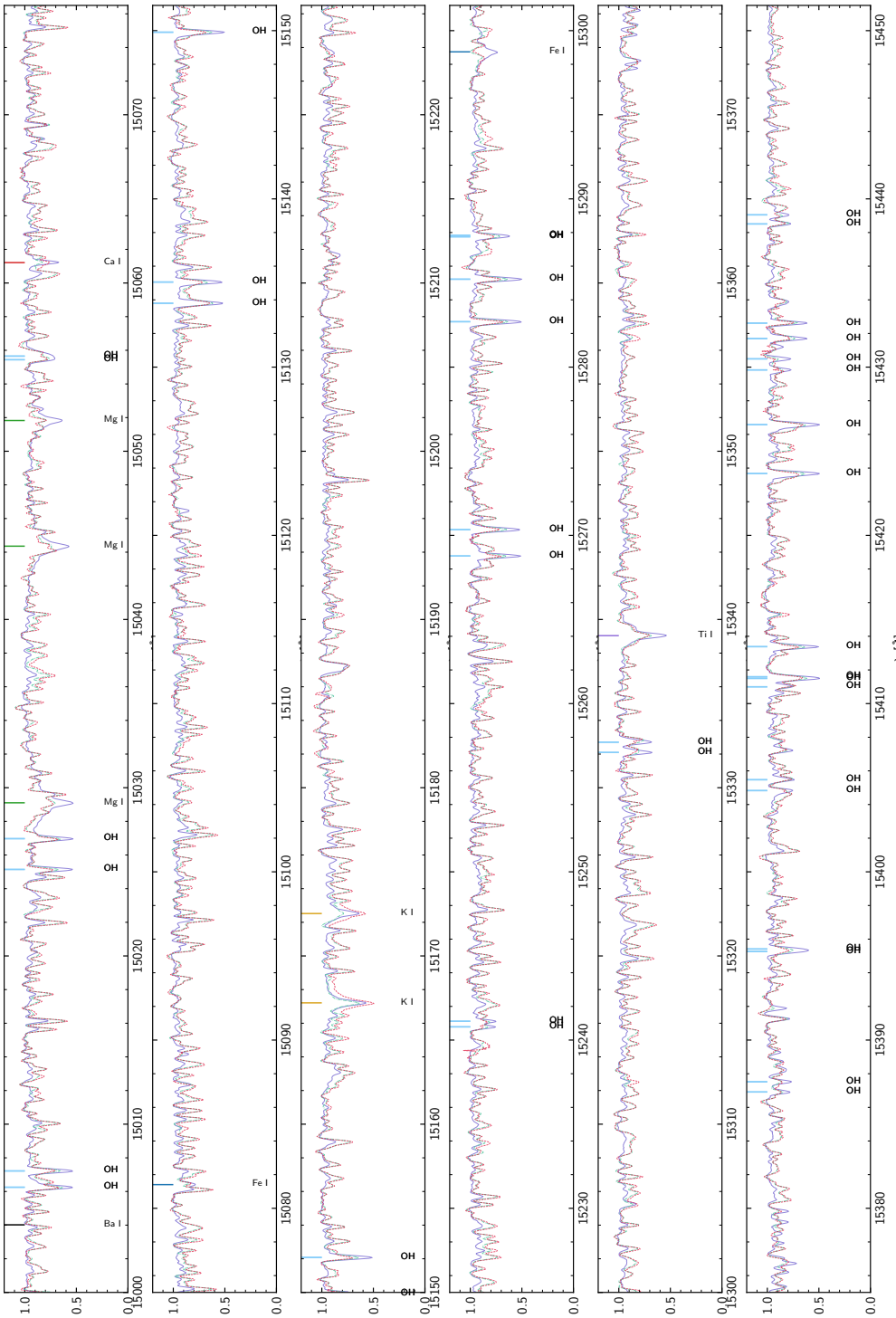

Figure A.12: IRD spectral atlas (Continued)

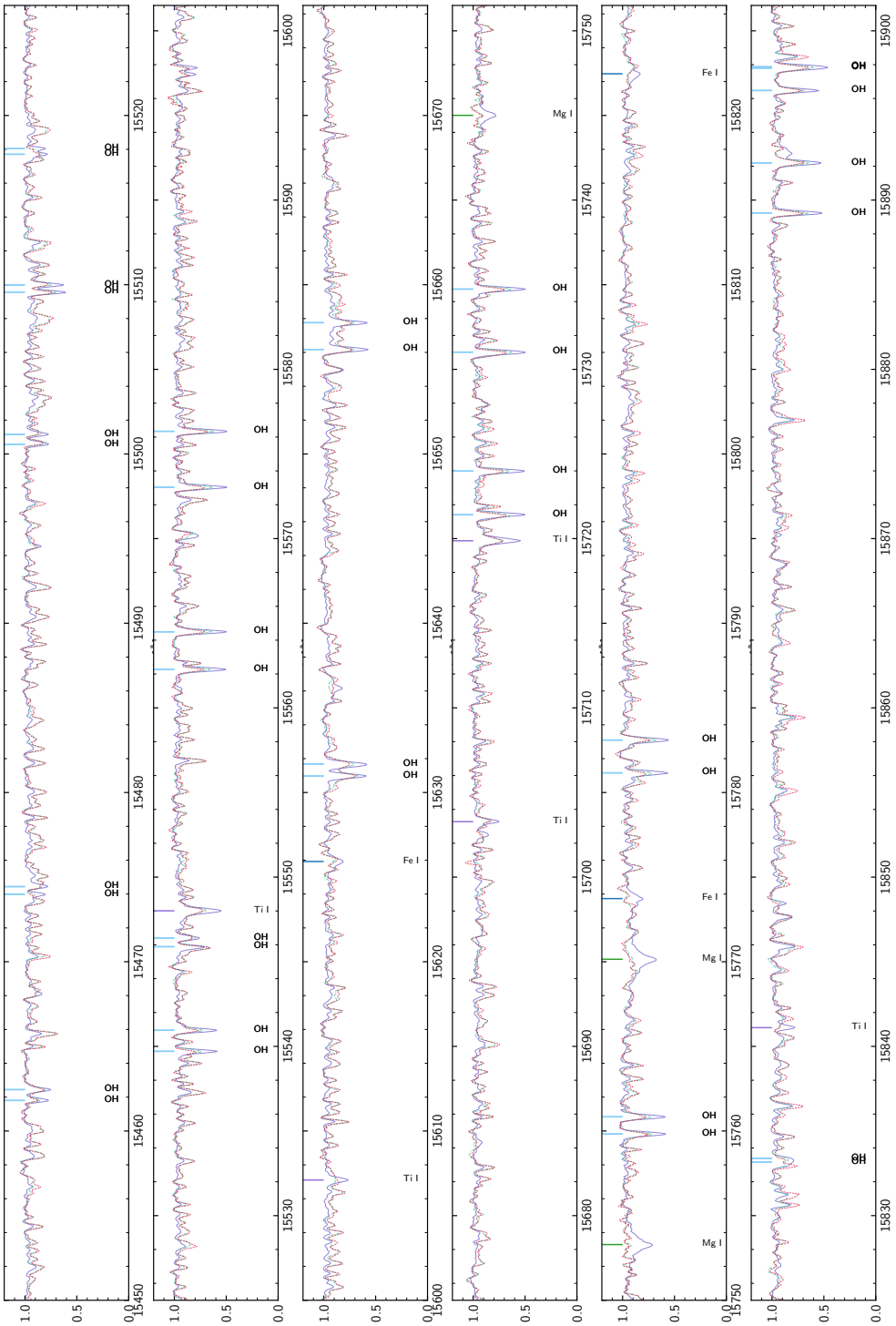

Figure A.13: IRD spectral atlas (Continued)

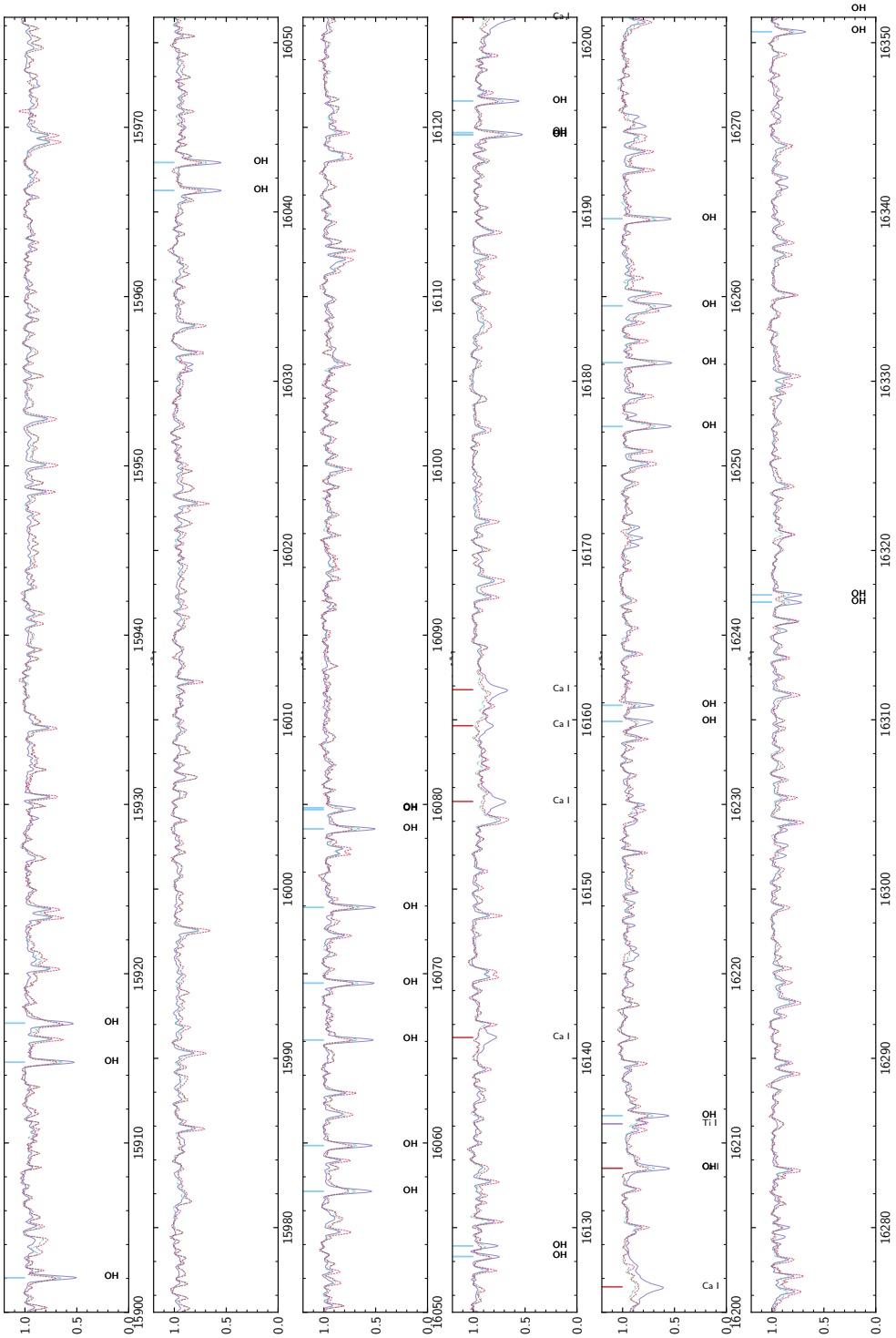

Figure A.14: IRD spectral atlas (Continued)

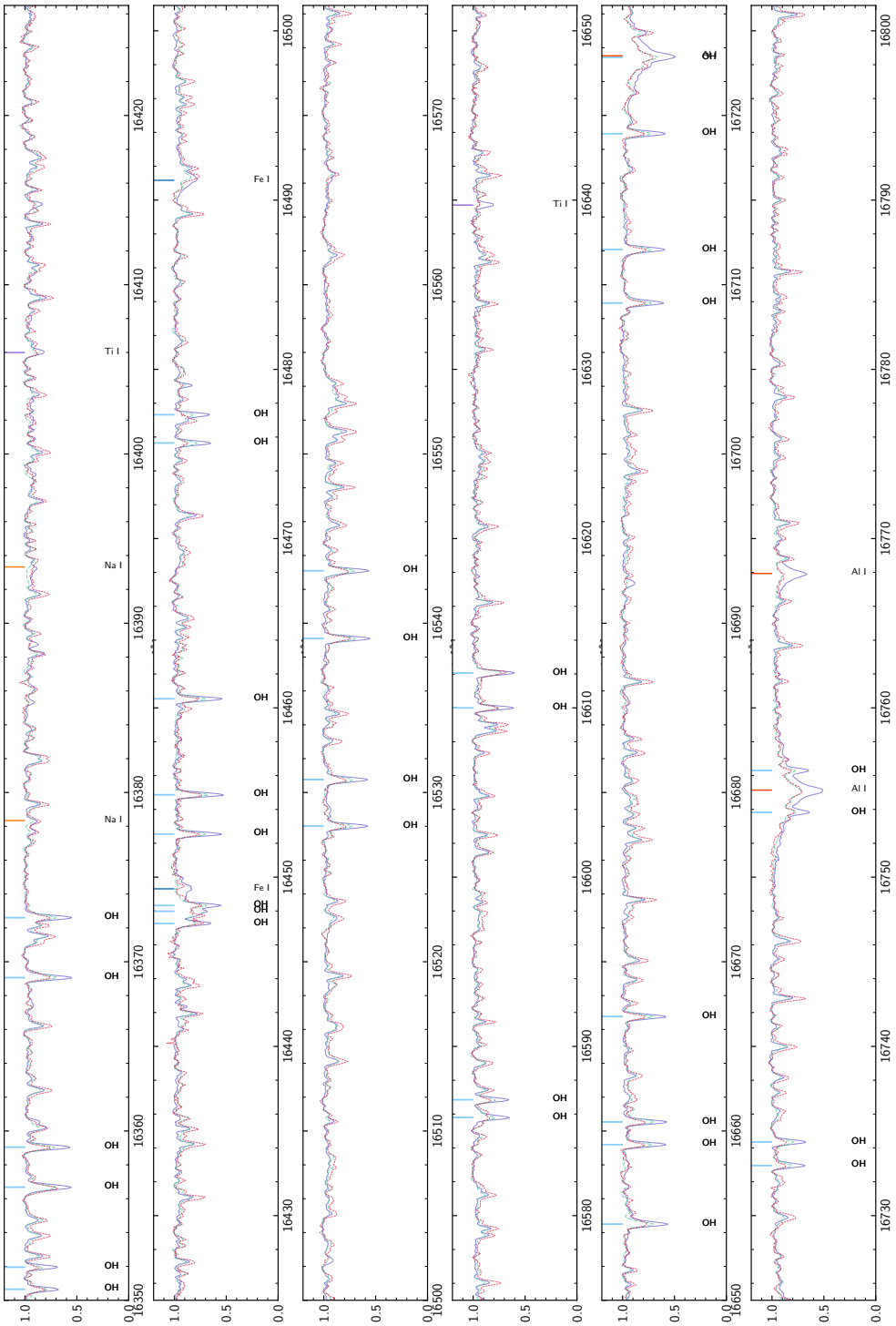

Figure A.15: IRD spectral atlas (Continued)

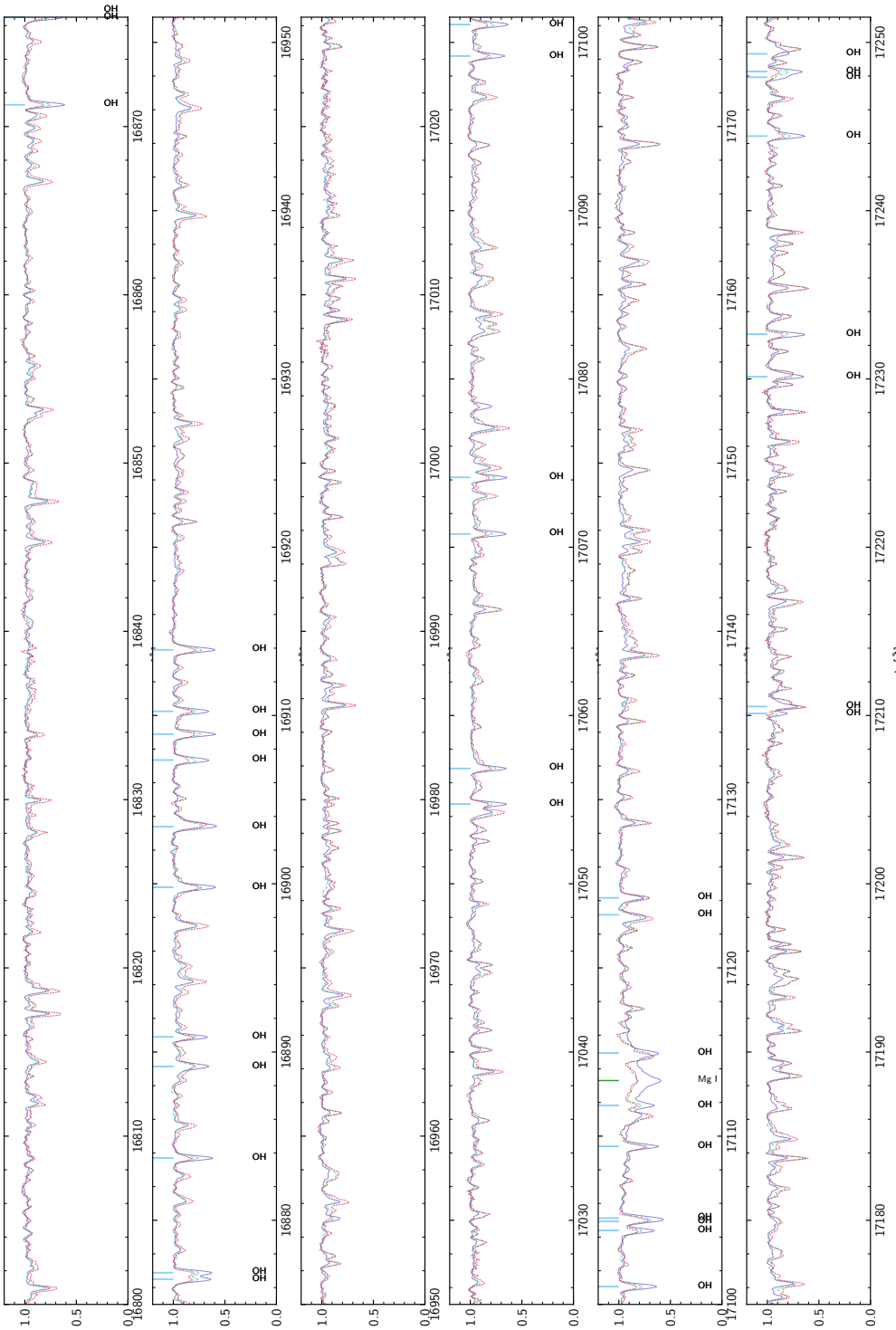

Figure A.16: IRD spectral atlas (Continued)